Nanodispersion Strengthened Metallic Composites with Enhanced Neutron Irradiation Tolerance

Award Number: DE-NE0008827

Award Dates: 10/2018 to 09/2021 – PIE until 02/2026

PI: Ju Li (MIT)

Team Members: Kang Pyo So, So Yeon Kim, Alexander O'Brien, Emre Tekoglu

Collaborators: Alina C. Zackrone, Sriswaroop Dasari, Cheng Sun, Mitch Meyer (INL)

Kory Linton, Annabelle Le Coq, Xiang Chen, Ben Garrison (ORNL)

Special thanks to our Oak Ridge National Lab collaborators

Kory Linton

Annabelle Le Coq

Xiang Chen

Ben Garrison

Idaho National Lab collaborators

Sriswaroop Dasari

Alina C. Zackrone

Cheng Sun

Mitch Meyer

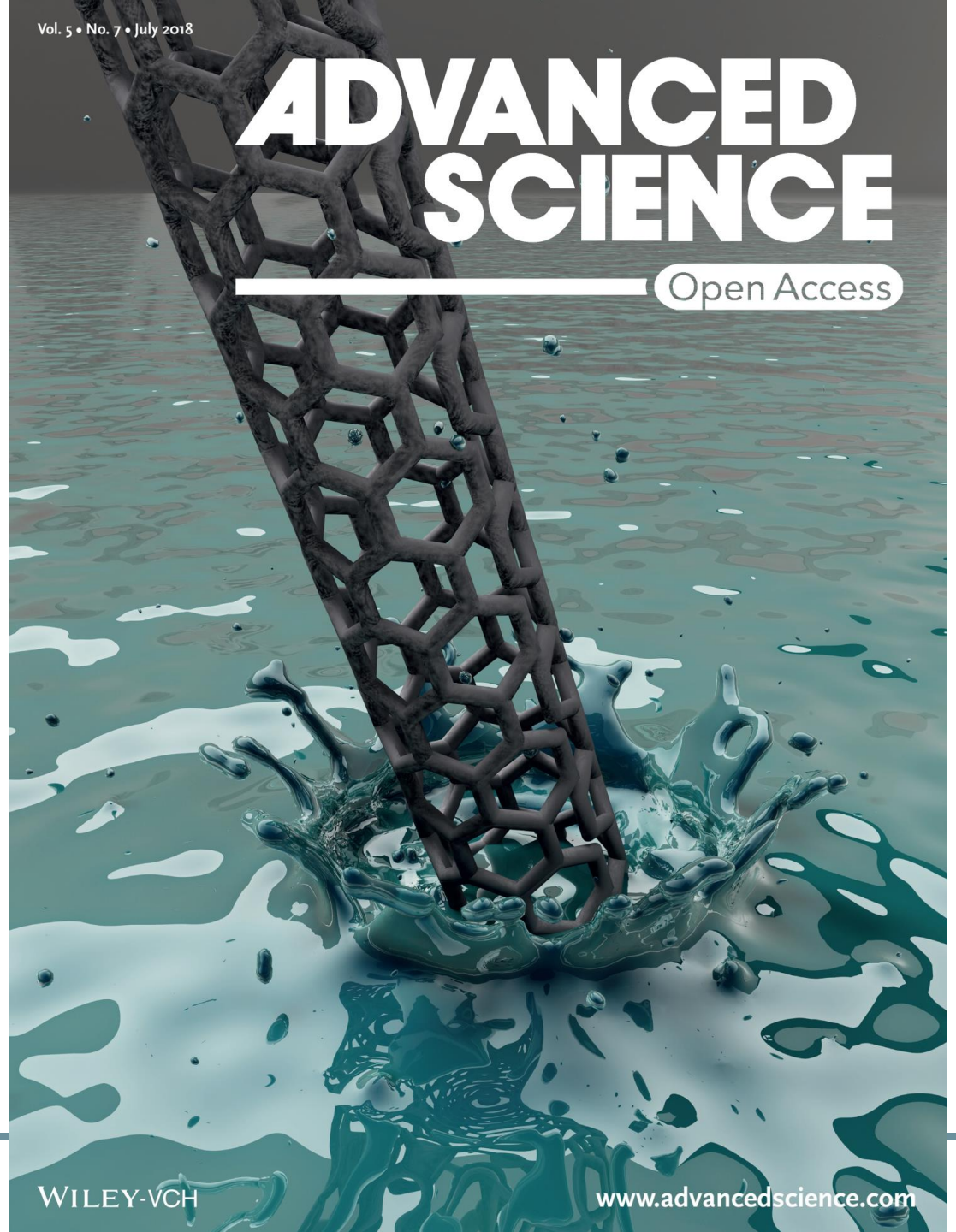

Intragranular Dispersion of Carbon Nanotubes Comprehensively Improves Aluminum Alloys, *Advanced Science* (2018) 1800115

Ton-scale metal-carbon nanotube composite: The mechanism of strengthening while retaining tensile ductility, *Extreme Mechanics Letters* **8** (2016) 245

Dispersion of carbon nanotubes in aluminum improves radiation resistance, Kang Pyo So, …, Ju Li, *Nano Energy* **22** (2016) 319

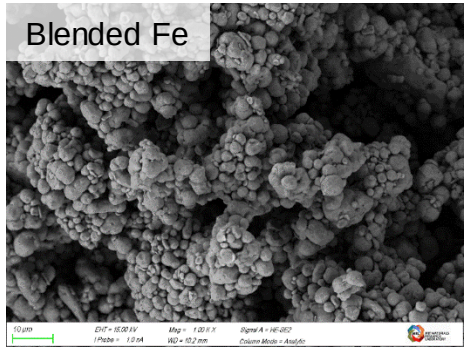

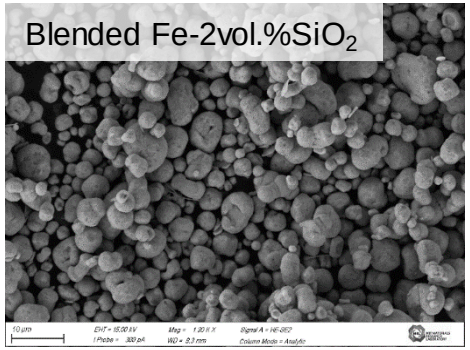

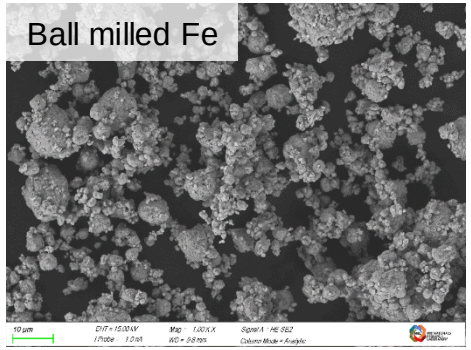

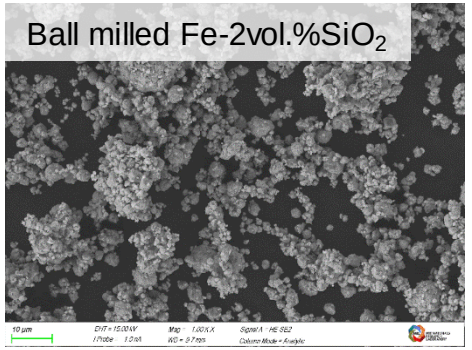

2 vol% dispersoid ×
10% uptake
= 0.2% He uptake
= 2000 appm He

Demonstration of Helide formation for fusion structural materials as natural lattice sinks for helium,
S.Y. Kim, … J. Li,
Acta Materialia **266** (2024) 119654

Elastic energy = $V^{\beta} \cdot 6\mu\delta^2 E(c/a)$

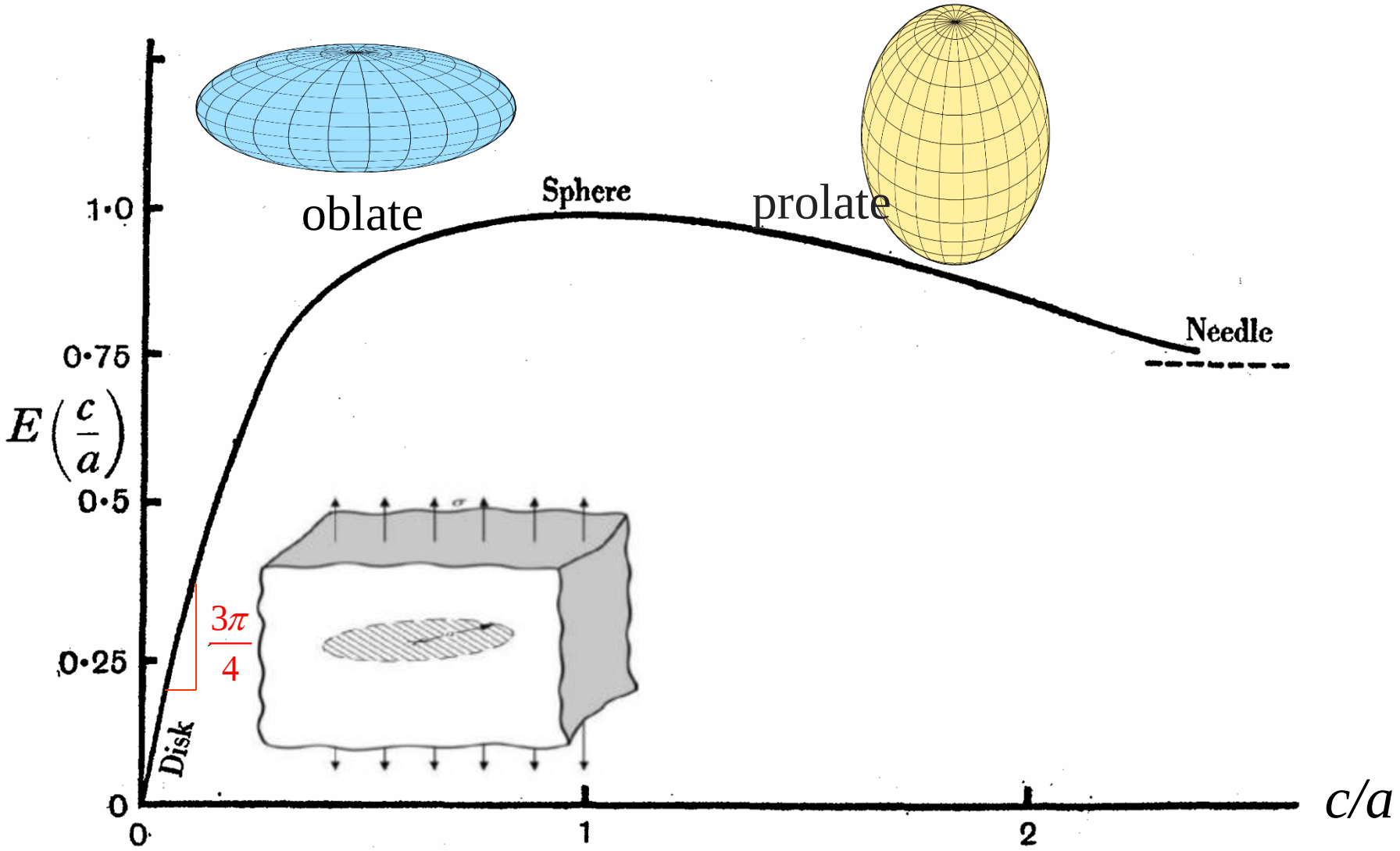

F. R. N. Nabarro, "The strains produced by precipitation in alloys," *Proc. R. Soc. Lond.* A **175** (1940) 519.

Nanofiller Declustering via Blending

Encapsulation & Consolidation via Ball Milling
3x at 600rpm for 10min

Casting Into Miniature Billets
800°C for 20min
Stirring at 1300rpm

We have developed melt-processing (casting & 3D printing), with nanodispersions

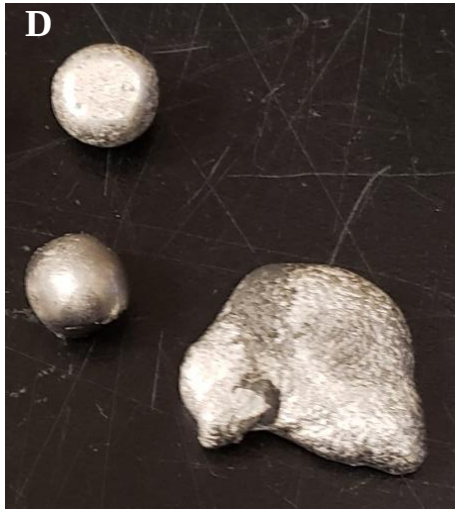

Casting process resulted in separation of the TiO_2 material, indicating wetting incompatibility

Extrusion Into Rods with 1mm Radius
400°C
10 tons of force

Cold Rolling Into Thin Foil
Thickness ~100µm

Stamping Into Dogbone Samples

Heat Treatment
400°C for 7 hours

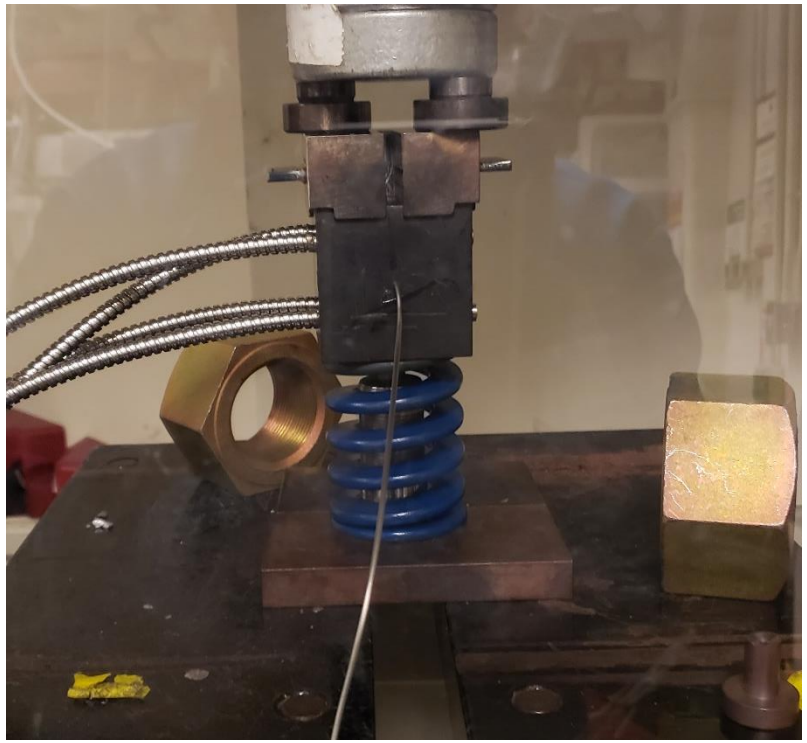

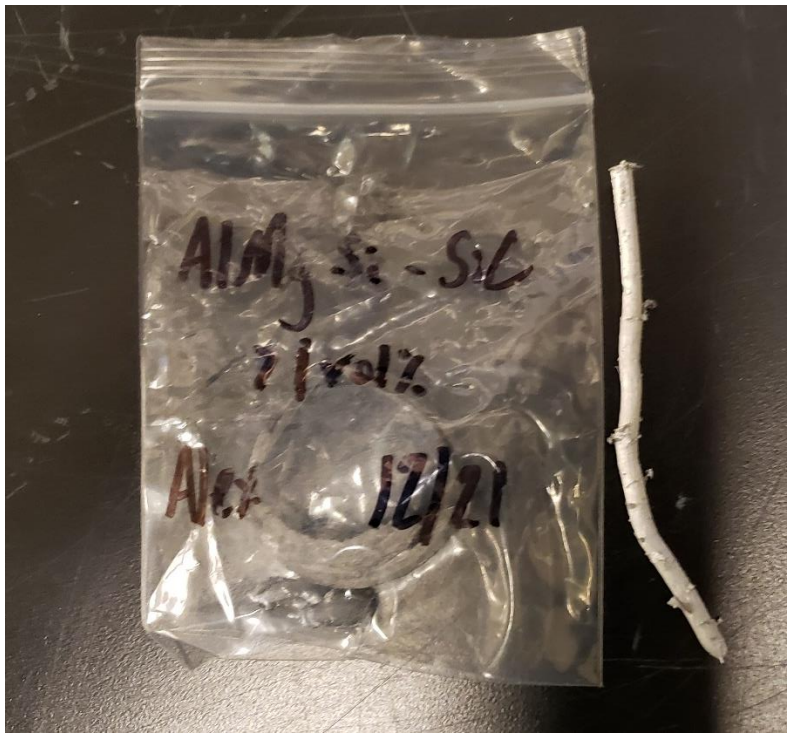

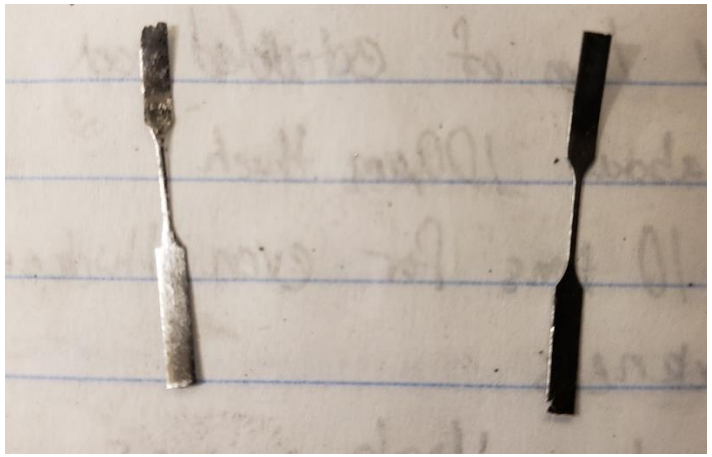

Dogbone samples compatible with eventual irradiation testing were prepared, allowing for tensile property comparison of materials.

Results of Al-Mg-Si tensile property comparisons indicate that the SiC composite achieves the highest increase in strength while maintaining good ductility

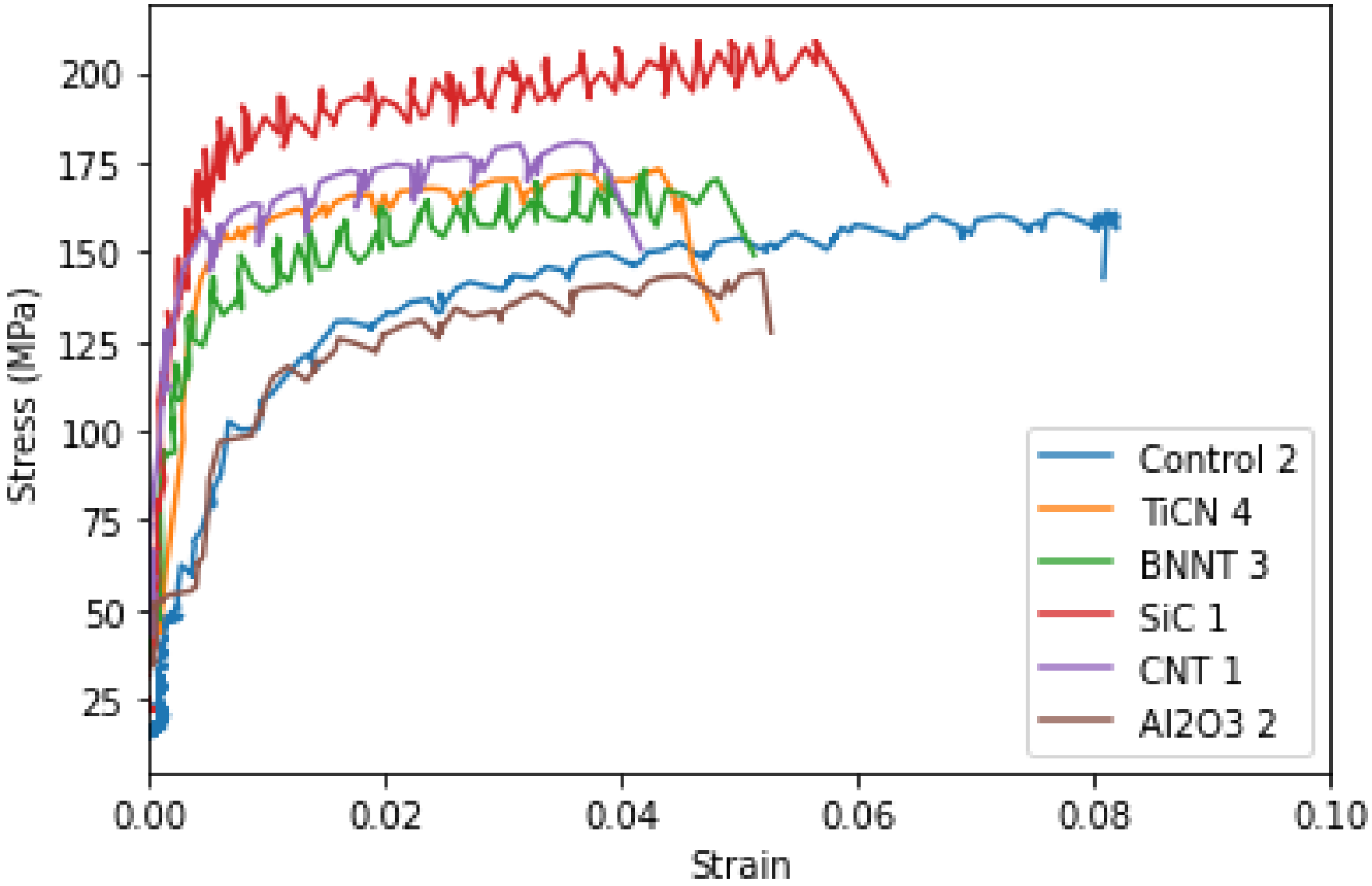

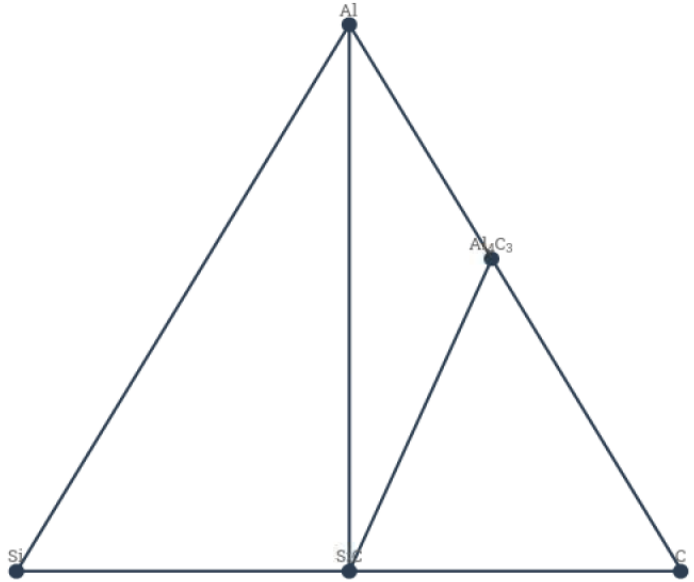

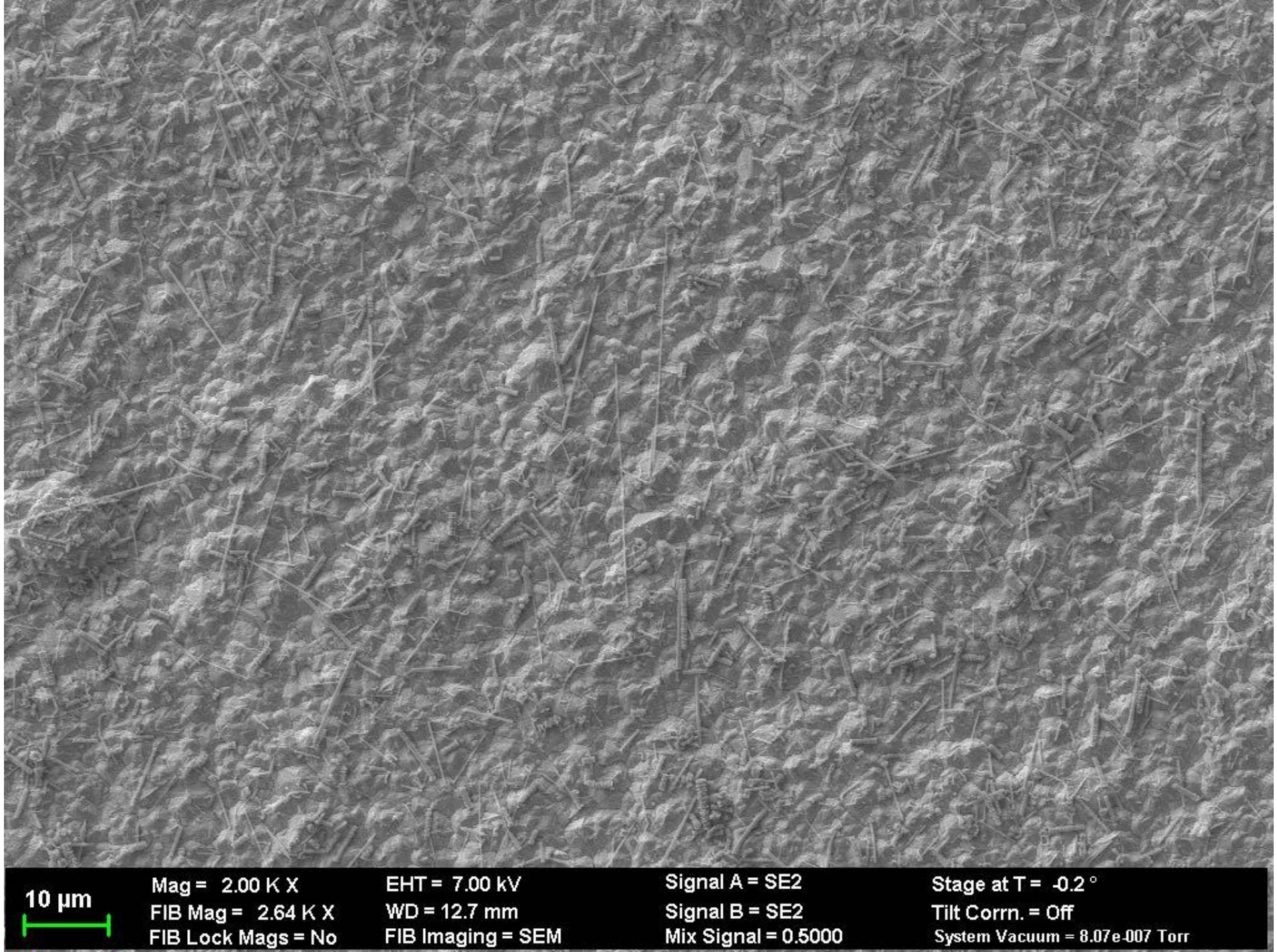
10 µm
Mag = 2.00 K X
FIB Mag = 2.64 K X
FIB Lock Mags = No
EHT = 7.00 kV
WD = 12.7 mm
FIB Imaging = SEM
Signal A = SE2
Signal B = SE2
Mix Signal = 0.5000
Stage at T = -0.2 °
Tilt Corrn. = Off
System Vacuum = 8.07e-007 Torr

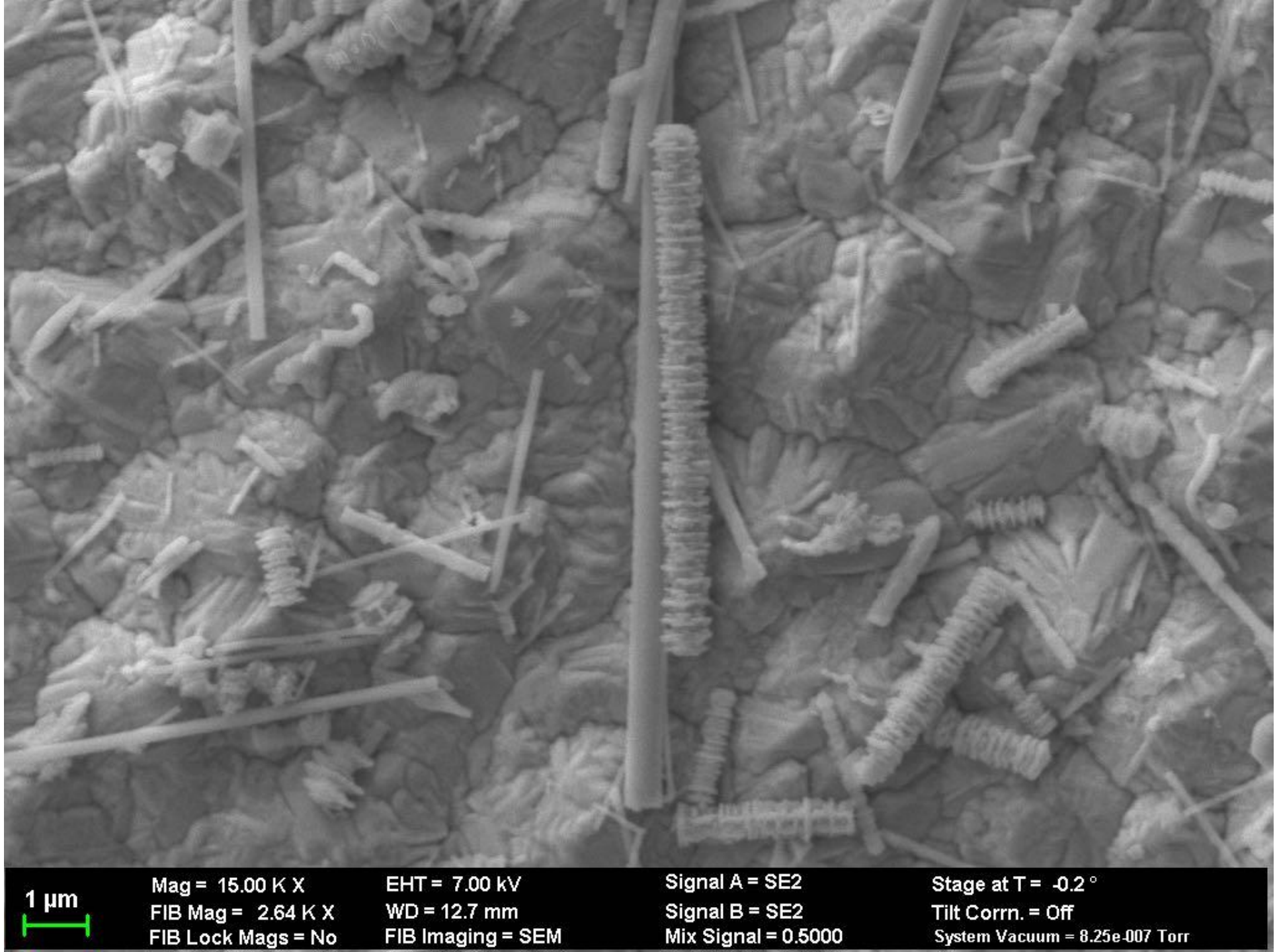
1 µm
Mag = 15.00 K X
FIB Mag = 2.64 K X
FIB Lock Mags = No
EHT = 7.00 kV
WD = 12.7 mm
FIB Imaging = SEM
Signal A = SE2
Signal B = SE2
Mix Signal = 0.5000
Stage at T = -0.2 °
Tilt Corrn. = Off
System Vacuum = 8.25e-007 Torr

Part layout for capsules

Neutron irradiation completed by Nov. 2021

#	Materials	DPA	Temperature	Number of dog-bone samples
1	Al	0.7, 1.4, 2.1	350°C	9
2	Al + 1 vol.% CNT	0.7, 1.4, 2.1	350°C	9
3	Cu	0.7, 1.4, 2.1	350°C	9
4	Cu + 1 vol.% graphene	0.7, 1.4, 2.1	350°C	9
5	Steel 1	0.7, 1.4, 2.1	350°C	9
6	Steel 1 + 2 wt.% $Y_2Ti_2O_7$	0.7, 1.4, 2.1	350°C	9
7	Steel 2	0.7, 1.4, 2.1	350°C	9
8	Steel 2 + 2 wt.% $Y_2Ti_2O_7$	0.7, 1.4, 2.1	350°C	9
9	Ni	0.7, 1.4, 2.1	350°C	9
10	Ni + 1 vol.% CNT	0.7, 1.4, 2.1	350°C	9
11	Single crystal Ni	0.7, 1.4, 2.1	350°C	9
12	Fe-16Cr-2Si	0.7, 1.4, 2.1	350°C	9
13	Fe-20Cr-2Si	0.7, 1.4, 2.1	350°C	9
Total number of dog-bone samples				117

Matrix compositions

- Steel 1: Martensitic stainless steel Fe-9Cr-1W
- Steel 2: Austenitic stainless steel Fe-15Cr-7Ni

1. Design and Assembly of Rabbit Capsules for Irradiation of Prototype Metal and Nanocomposite Specimens in the High Flux Isotope Reactor (ORNL)

- A HFIR cycle provides between 1.4 - 1.7 dpa per cycle depending on the material and position
- 2 rabbits per dose at 300°C (+/- 20°C)
  - ~.7 dpa - Hydraulic Tube for 13 days (.5 cycle)
  - ~1.4 dpa - Standard position for 1 cycle
  - ~2.1 or 2.8 dpa - either 1 full cycle plus 13 days in Hydraulic Tube position / or 2 full cycle

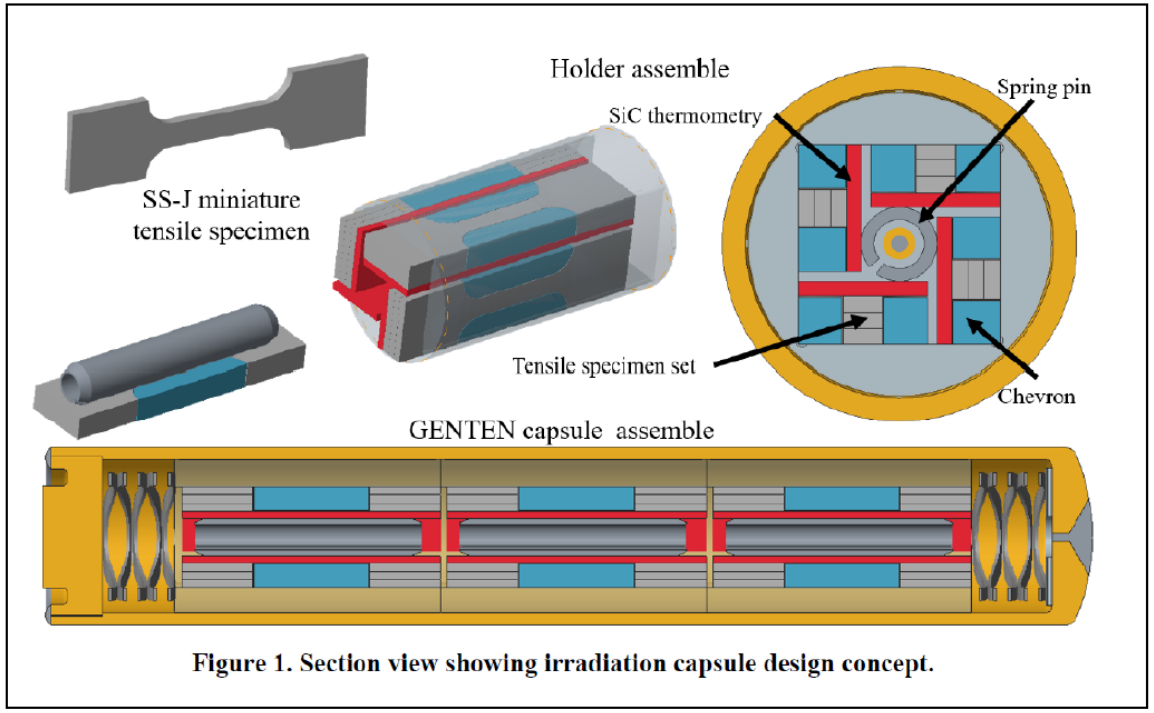

Figure 1. Section view showing irradiation capsule design concept.

Proposed Test Matrix

DPA	Rabbit ID	Sub Assembly	SS-J2 Tensile 16x4x.5	MPC1 Coupon (16x4x.25)
.7 dpa	JULI01	Top	6	6
		Mid	6	6
		Bottom	6	6
.7 dpa	JULI02	Top	6	6
		Mid	9	6
		Bottom	6	9
Total 0.7 dpa			39	39
1.4 dpa	JULI03	Top	6	6
		Mid	6	6
		Bottom	6	6
1.4 dpa	JULI04	Top	6	6
		Mid	9	6
		Bottom	6	9
Total 1.4 dpa			39	39
2.1 dpa	JULI05	Top	6	6
		Mid	6	6
		Bottom	6	6
2.1 dpa	JULI06	Top	6	6
		Mid	9	6
		Bottom	6	9
Total 2.1 dpa			39	39
Total			117	117

This email documents the completion of APT analysis of 6 of the samples from the 1st ORNL shipment of broken SSJ specimens to support CINR Project "MIT JL 18-1783 PIE (NSUF-1.2 HFEF)(PICS work package UA-22IN060502)". The 6 samples that have been analyzed for APT are listed below. This effort fulfilled the requirements of the Level III milestone "MIT JL 18-14783 PIE: Complete APT testing on 1st set of ORNL provided specimens (6 specimens) (Zackrone)".

IMCL ID#	Project ID#	Material	DPA
IMCL-0286	M9S 13	Steel2	1.4 dpa
IMCL-0290	M10S 01	Steel1+OC	0.7 dpa
IMCL-0295	M8S 08	Steel1	0 dpa
IMCL-0288	M11S05	Steel2(Fe-15Cr-7Ni) + 0D oxide/carbide	2.1 dpa
IMCL-0289	M11S13		1.4 dpa
IMCL-0294	M11S03		0 dpa

0D dispersoid

Next shipment of broken SSJ specimens from ORNL is shown below. The irradiated specimens will ship first, followed by the unirradiated samples at a later date. We anticipate having approval to ship the irradiated samples by the end of this week.

Material	Unirradiated	0.7 dpa	1.4 dpa	2.1 dpa
Al+CNT	M2A04	M2A07	M2A12	M2A01
Fe-16Cr-2Si	M3S16	M3S01	M3S06	M3S11
Fe-20Cr-2Si	M4S16	M4S06	M4S11	M4S01
Cu	M5C13	M5C01	M5C05	M5C09
Cu+Graphene	M6C06	M6C04	M6C03	M6C10

1D dispersoid

No dispersoid

2D dispersoid

No Dispersoid

Commercial Coarse-Grained Materials

Fe-16Cr-2Si

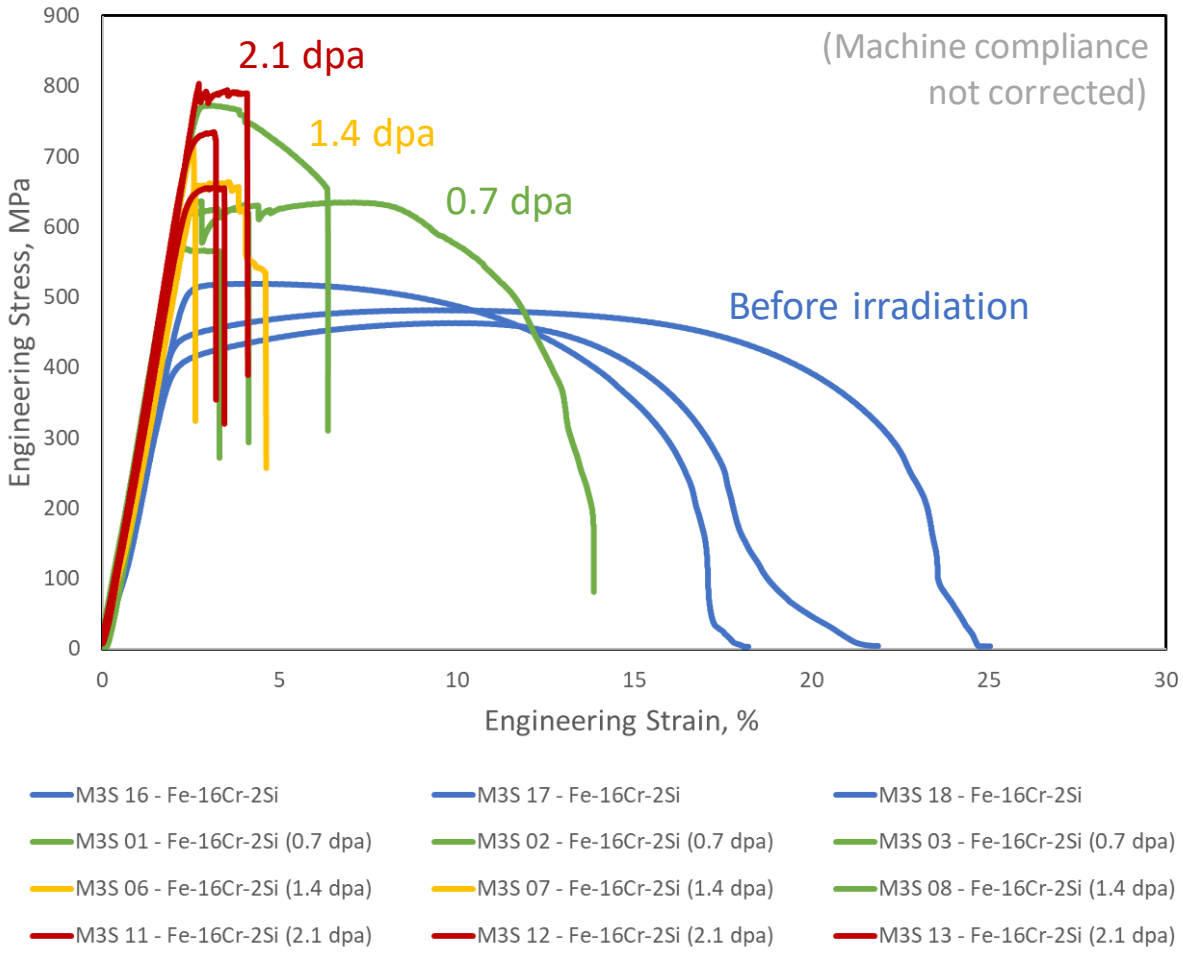

Fe-20Cr-2Si

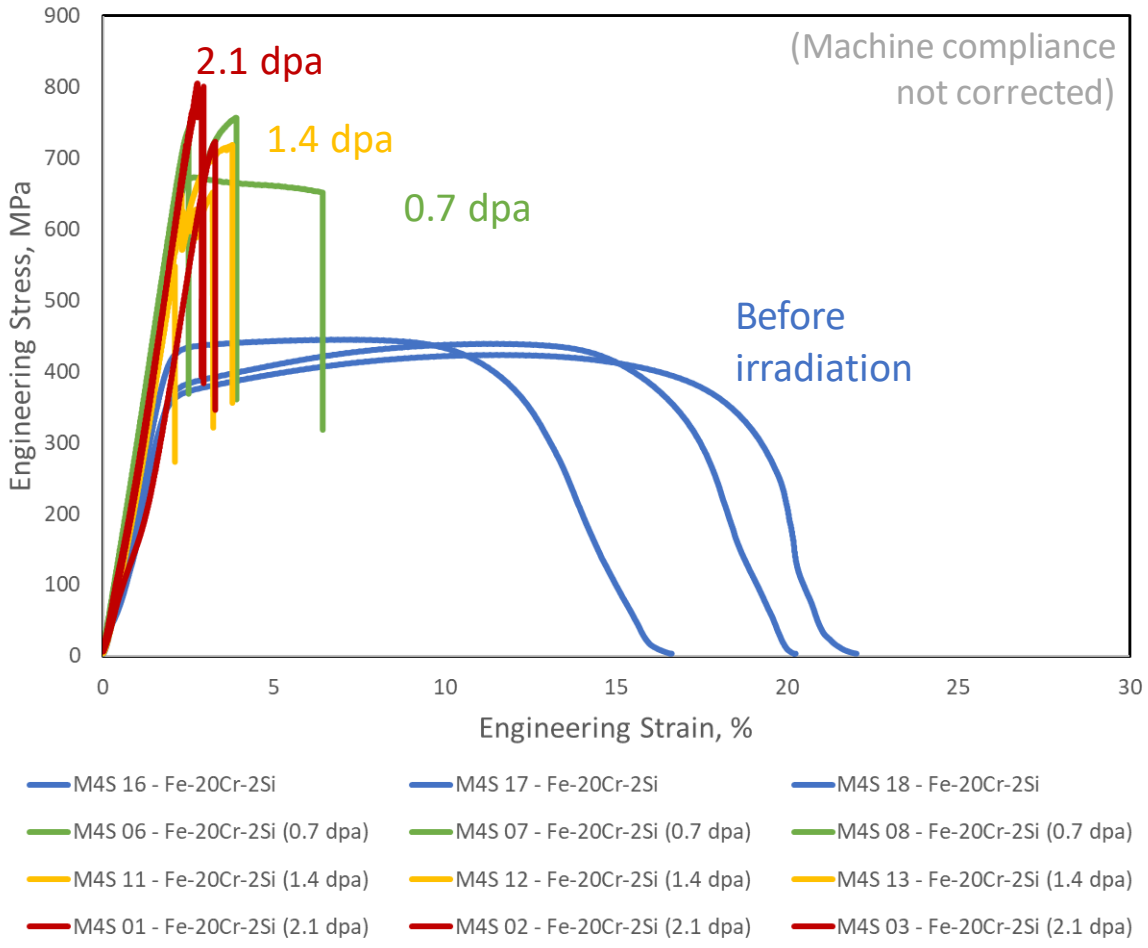

Significant radiation embrittlement even at <1 dpa

No Dispersoid

Single Crystal Ni

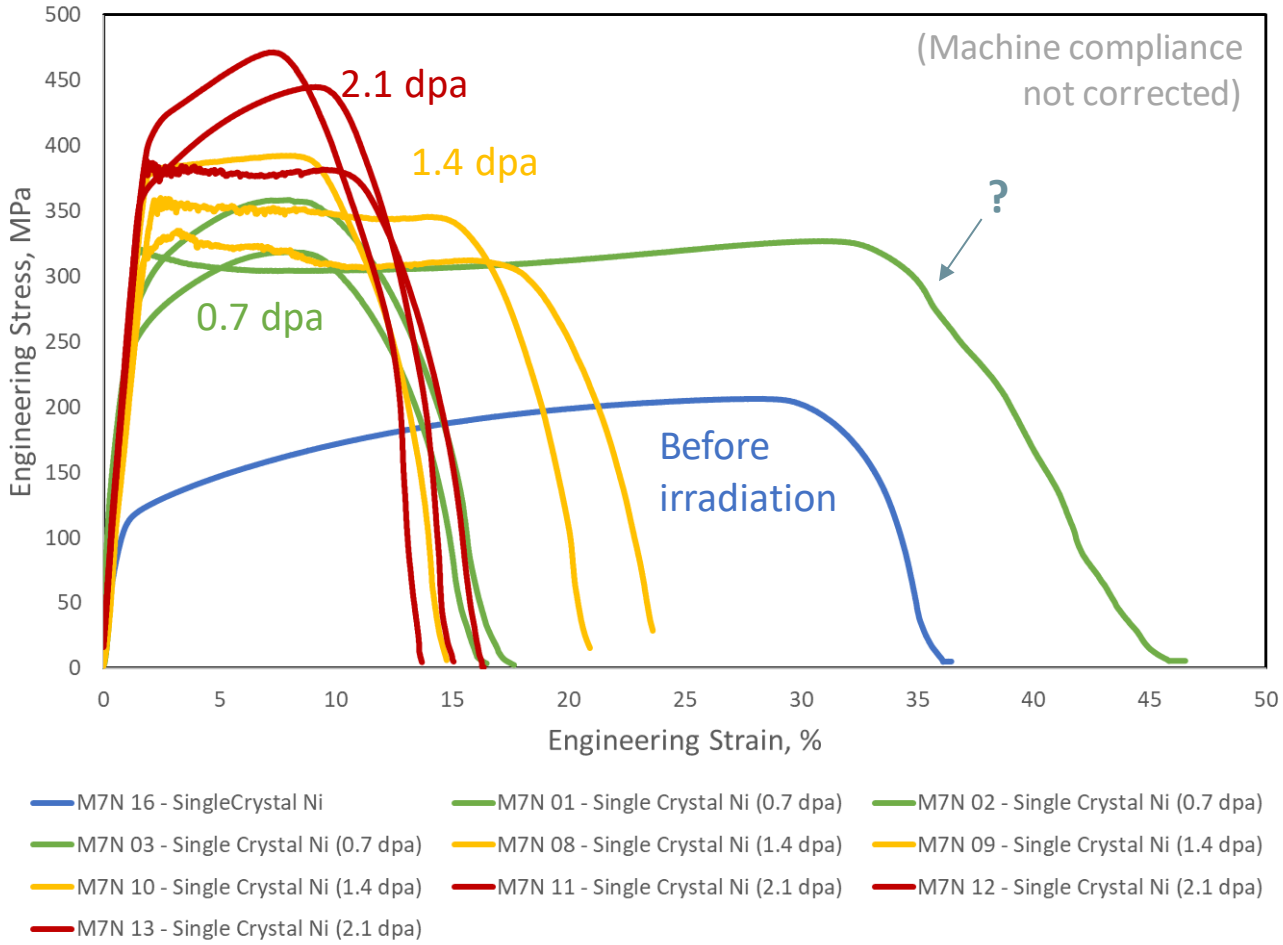

Tensile ductility decreased by a factor of > 2 upon irradiation but didn't change greatly with further increasing dpa

1D Dispersoid

Al (+ 1 vol% CNT)

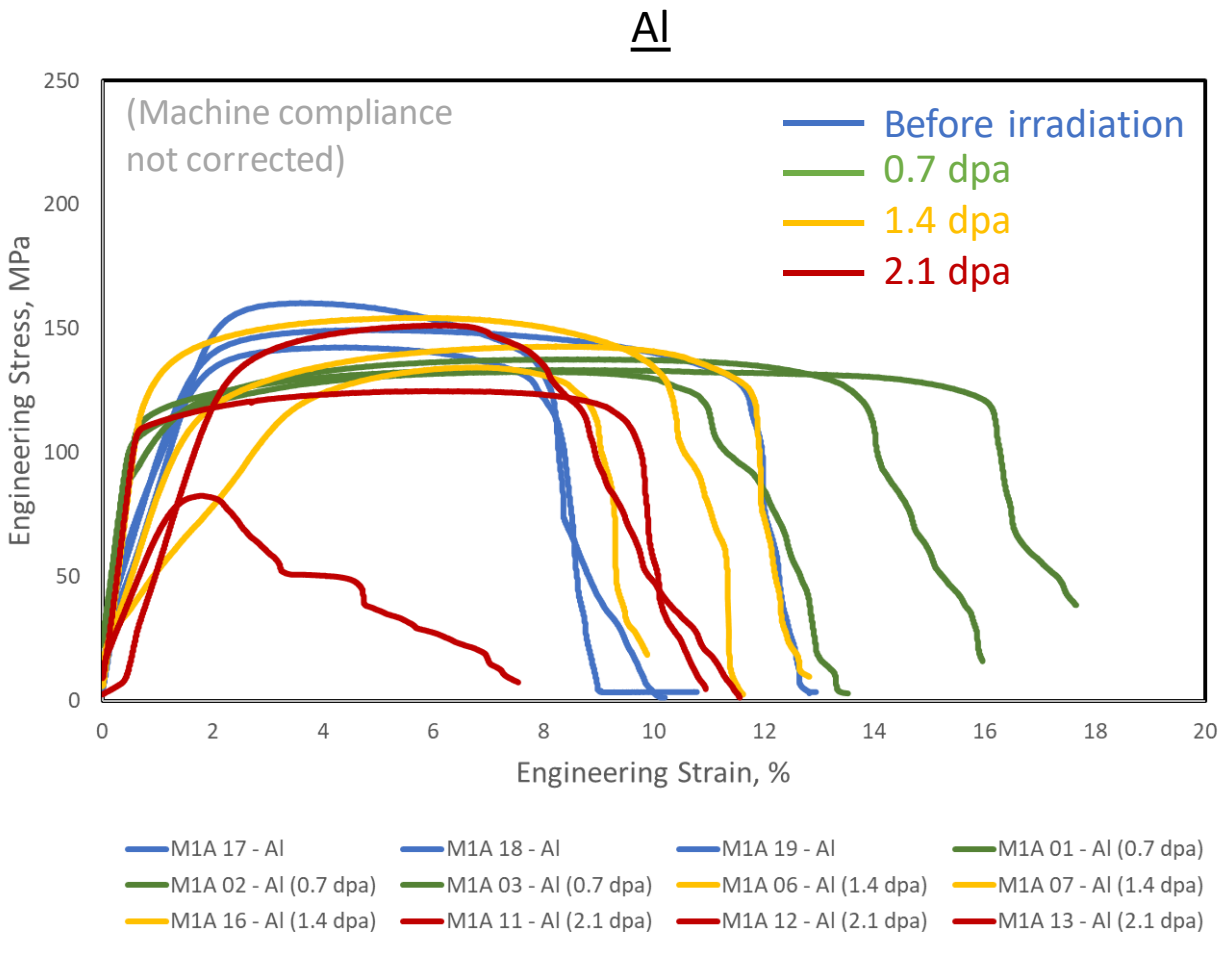

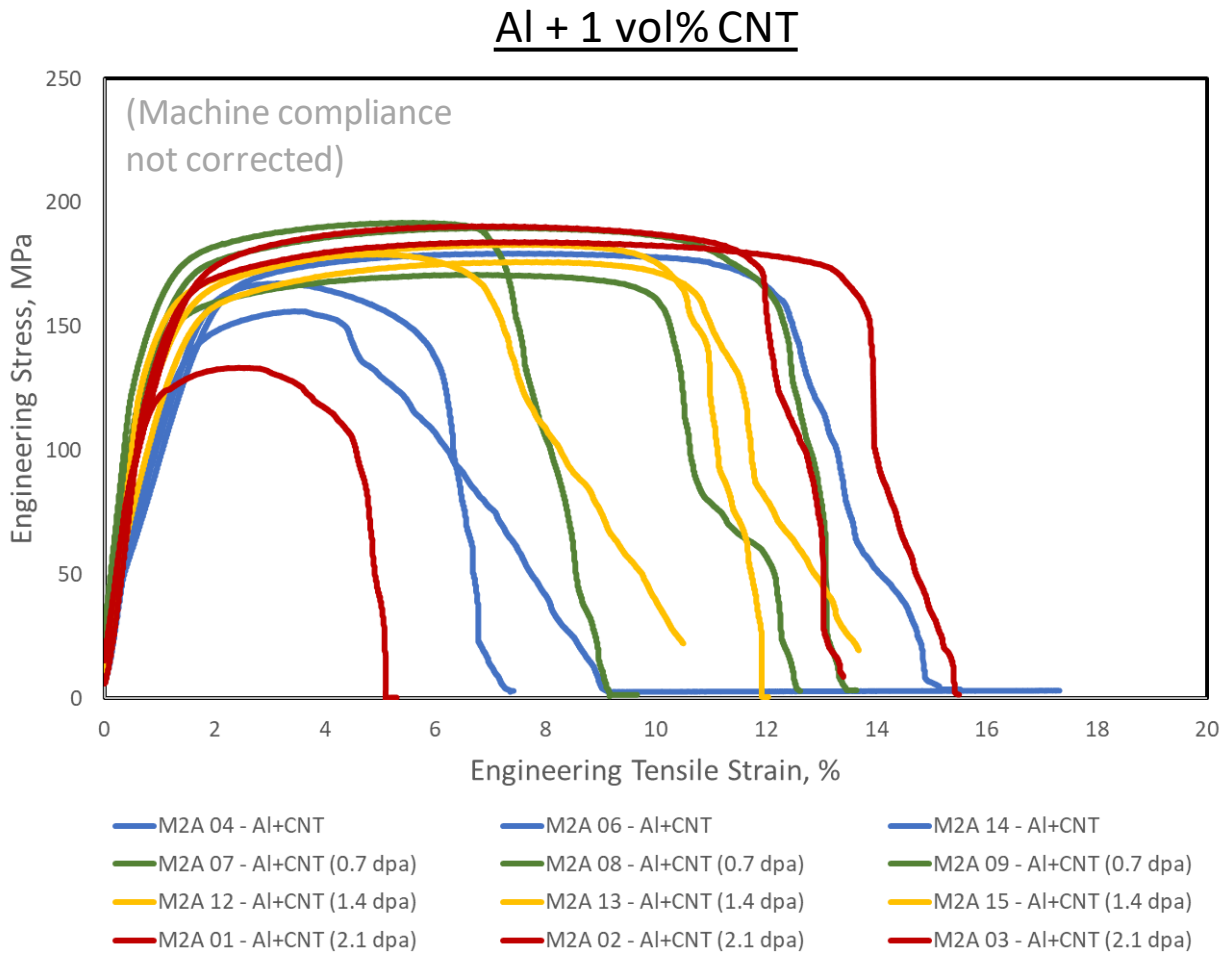

- Higher strength, but significant manufacturing variabilities
- Tensile ductility about the same
- No significant radiation embrittlement: low T_M(Al)=1000K

0D Dispersoid

9Cr-1W Steel (+ 2 wt% $Y_2Ti_2O_7$)

Without $Y_2Ti_2O_7$

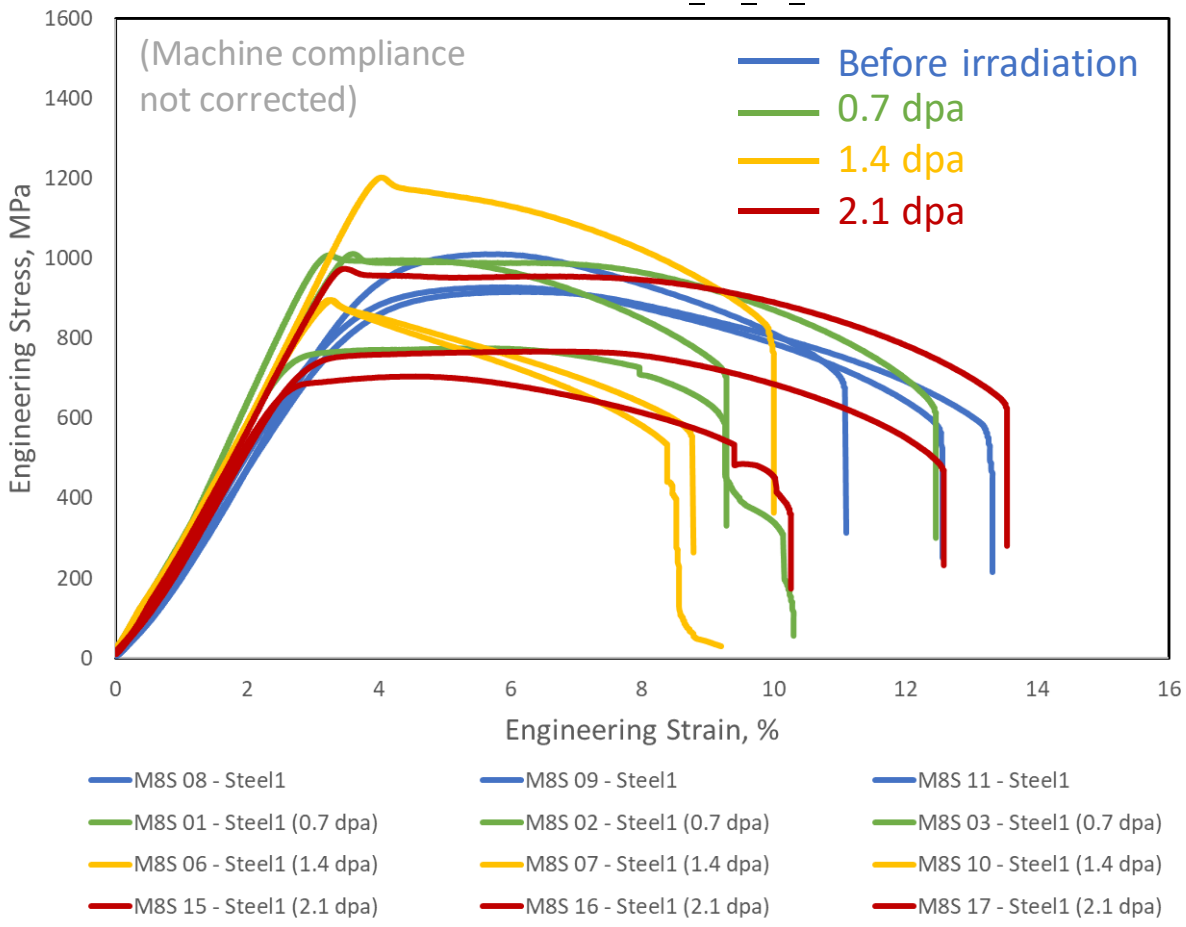

With 2 wt% $Y_2Ti_2O_7$

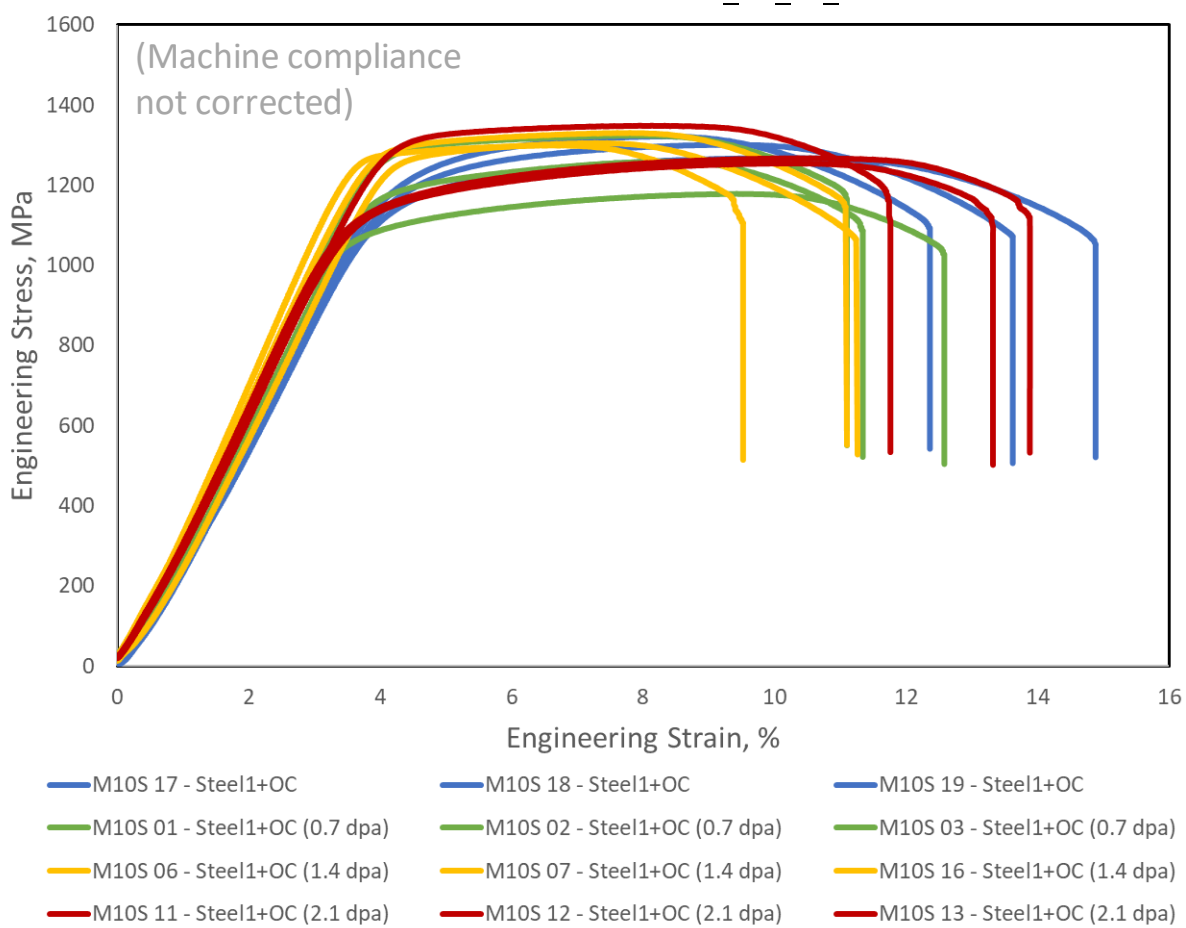

- Not large radiation embrittlement – F/M are intrinsically more radiation tolerant due to internal interfaces
  - The 2wt% YTO provides higher strength and ductility

0D Dispersoid

15Cr-7Ni Steel + 1 vol% TiC

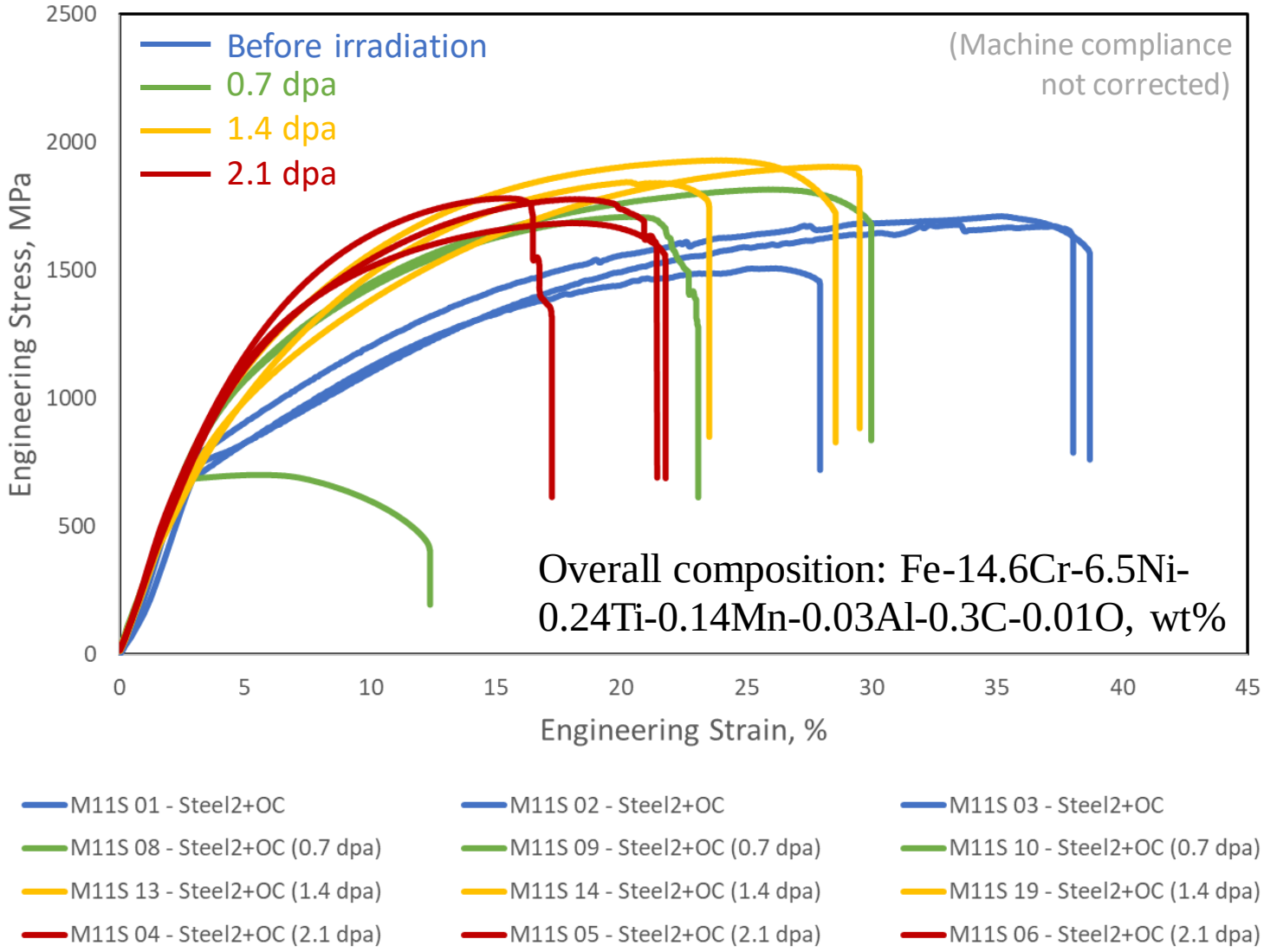

This sample had ~5% martensite before tensile tests and radiation

Tensile ductility decreases with radiation but is still greater than that of 9Cr-1W steel with $Y_2Ti_2O_7$, and it also exhibits significant work hardening capability.

0D Dispersoid

15Cr-7Ni Steel + 1 vol% TiC

1.4 dpa, before deformation

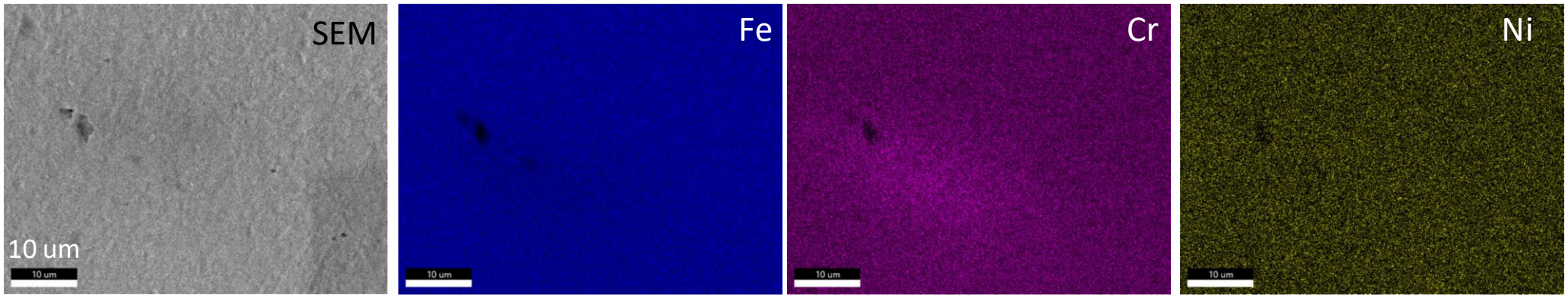

Cr-rich near TiC (observed both before and after irradiation)

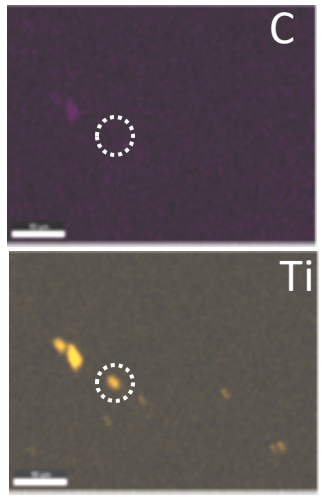

Ti-rich particles other than TiC are present (**Not observed before irradiation**)

2.1 dpa, before deformation

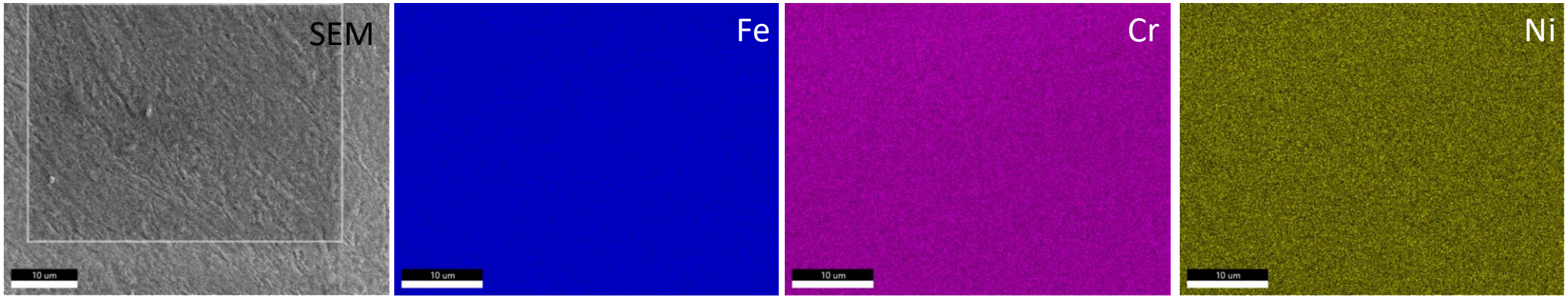

Further exploration is needed regarding TiC fraction, composition, spatial distribution, etc.

0D Dispersoid

15Cr-7Ni Steel + 1 vol% TiC

> 1 dpa, before deformation

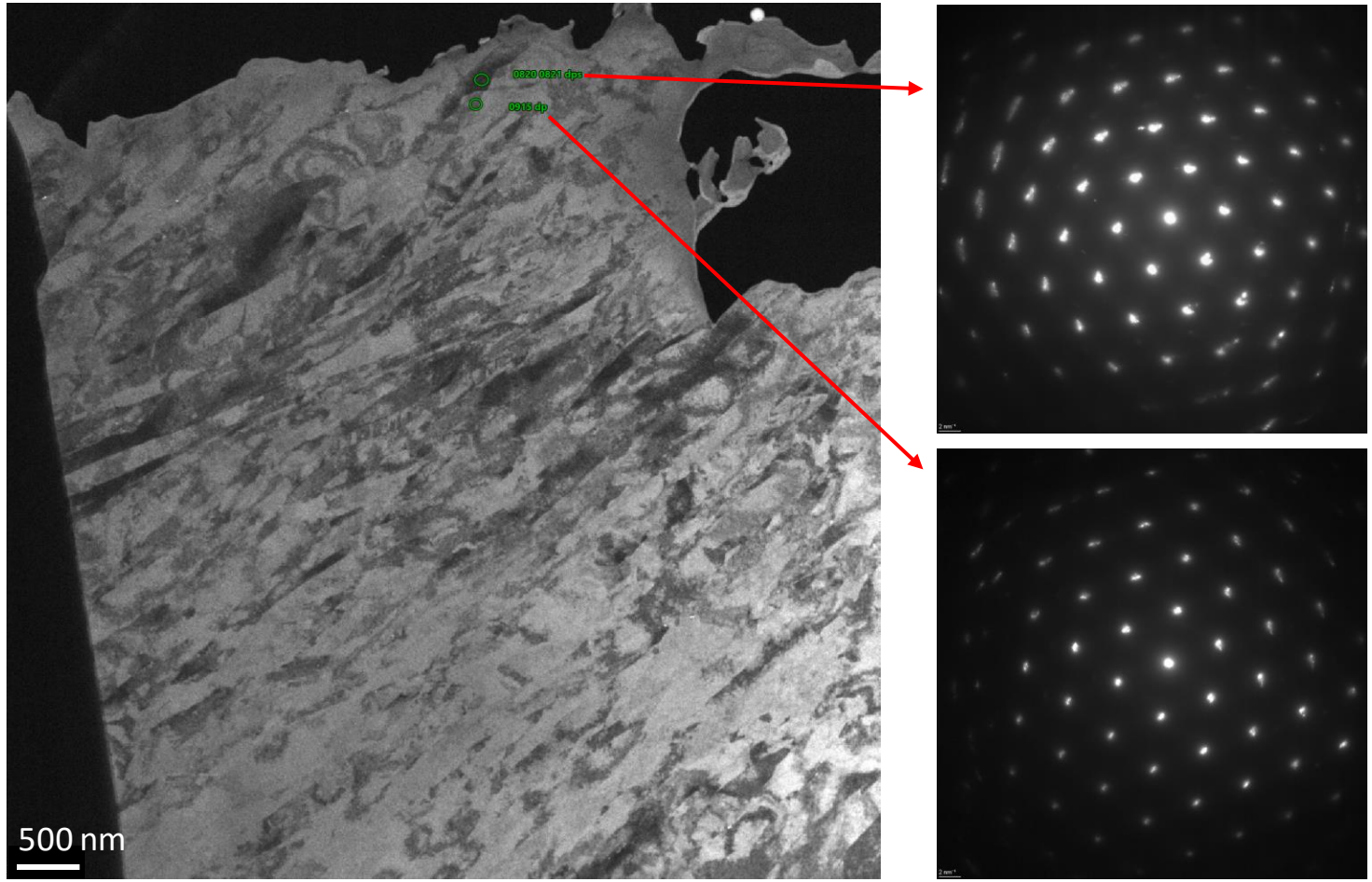

Highly nanostructured, accompanied by the presence of martensite

0D Dispersoid

15Cr-7Ni Steel + 1 vol% TiC

> 1 dpa, before deformation

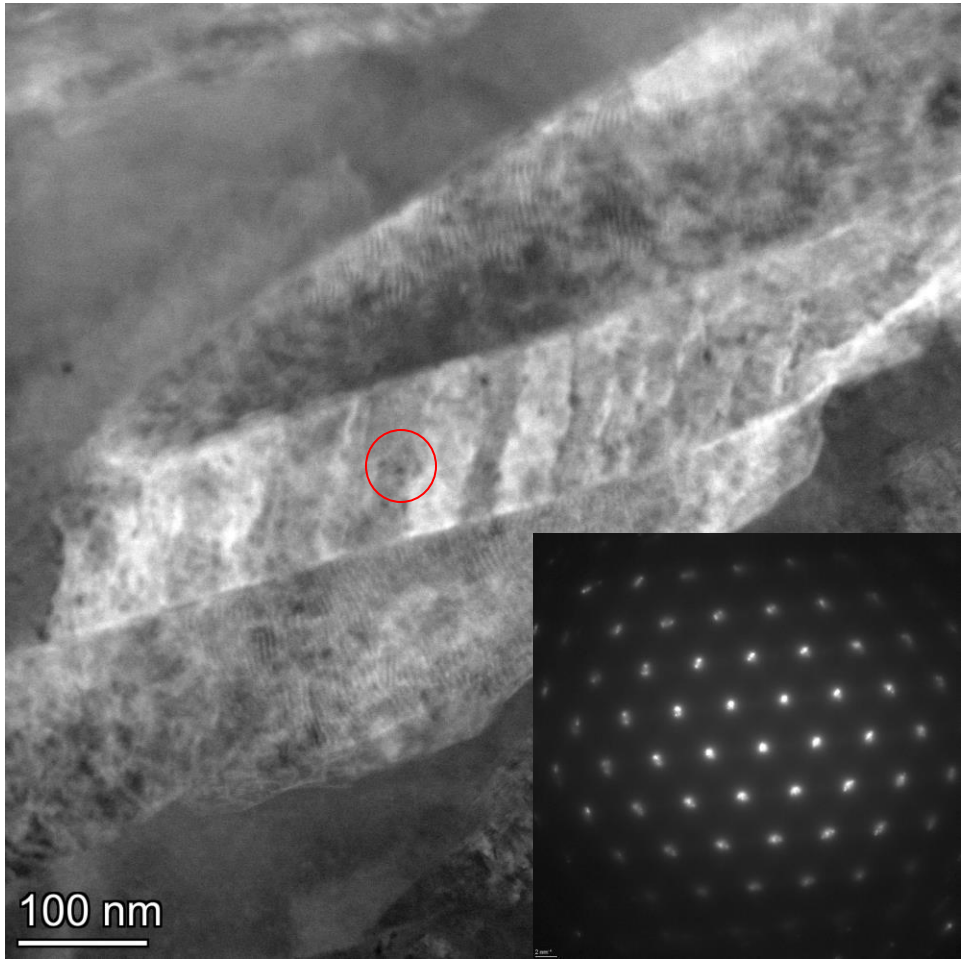

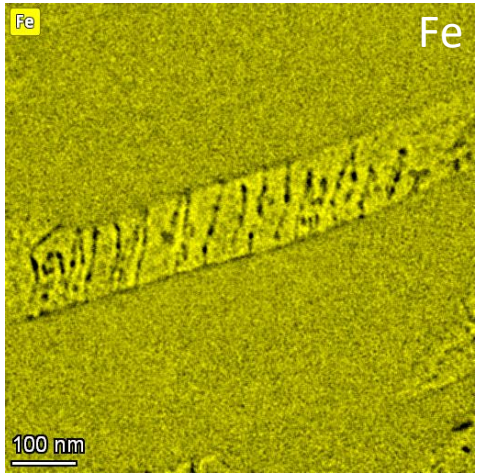

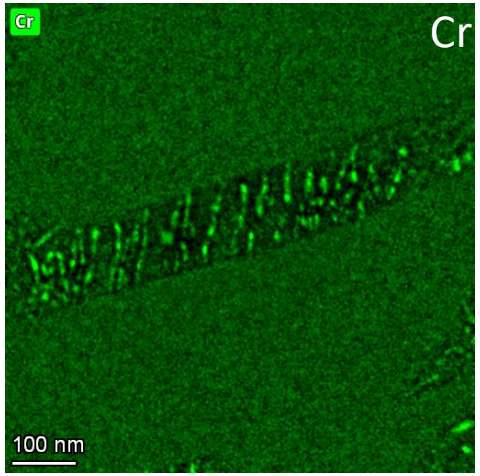

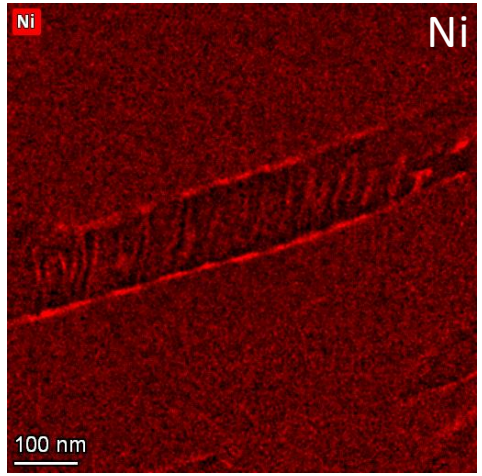

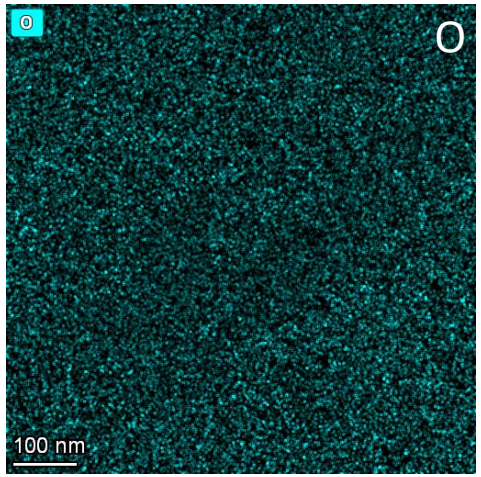

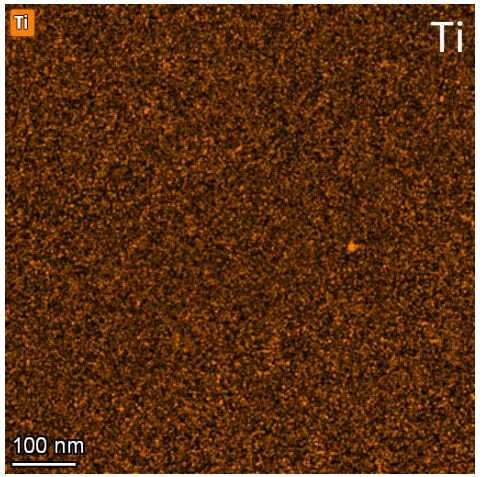

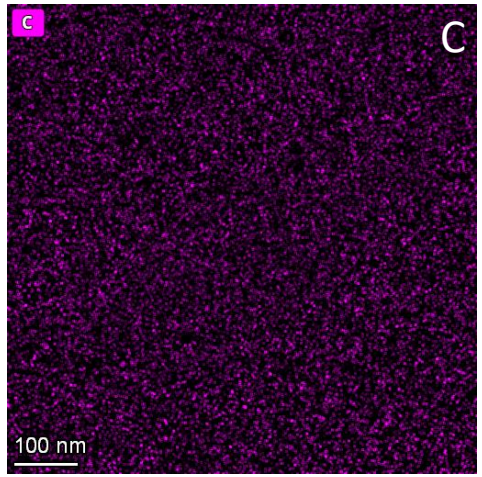

Elemental segregation is observed in martensite after irradiation.
Such elemental segregation was not observed in an atom probe analysis of unirradiated specimens.
The segregation happened during radiation.

0D Dispersoid

15Cr-7Ni Steel + 1 vol% TiC

> 1 dpa, before deformation

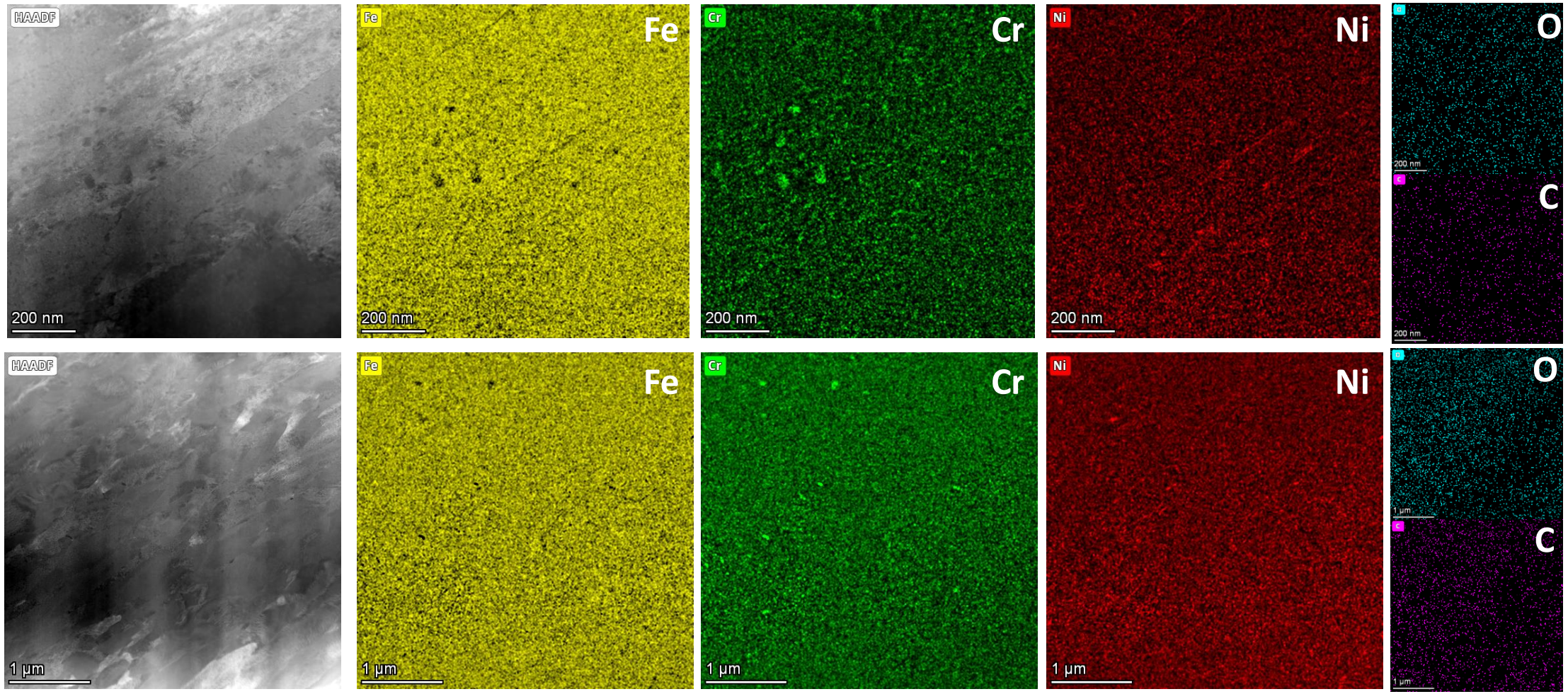

- Particle-like Cr-rich regions and **plate-like Ni-rich regions** were additionally observed.
- Correlations with the spatial distribution of other elements (e.g.,O or C) were **not** clearly seen **at the nanoscale**.

Reconstruction no. R1194

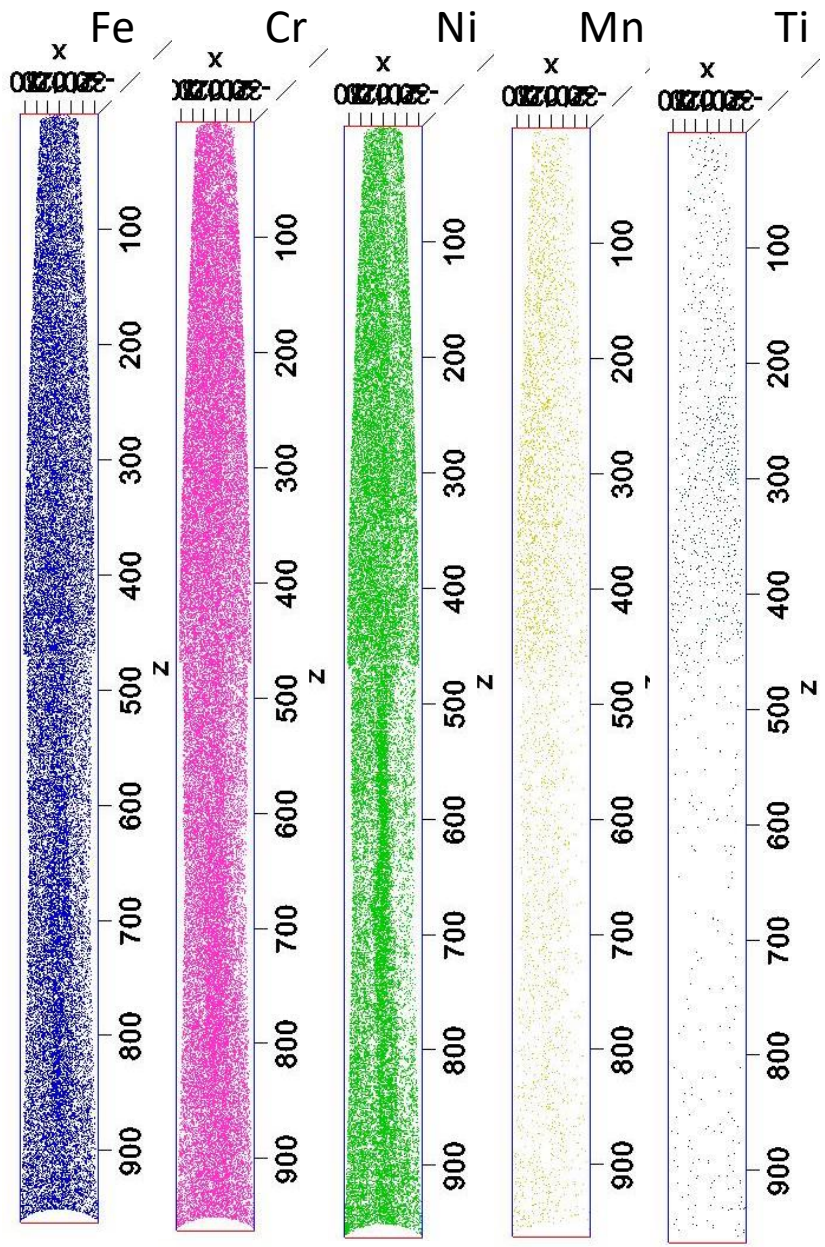

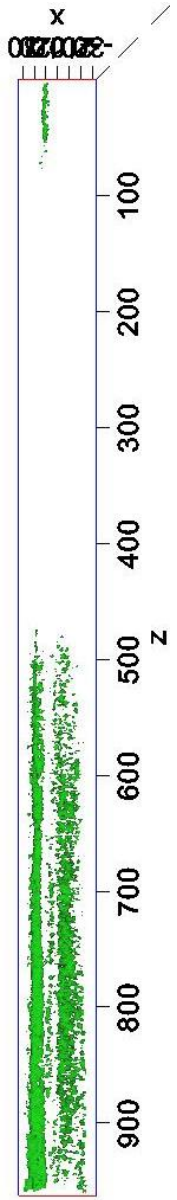

Ni iso-surface 11.2 at.%

Element	At.%	Sigma%
Fe	84.01	0.01
Cr	8.88	0.00
C	1.27	0.00
Ni	4.92	0.00
Ti	0.04	0.00
Mn	0.16	0.00
O	0.23	0.00
H	0.48	0.00

Bulk composition

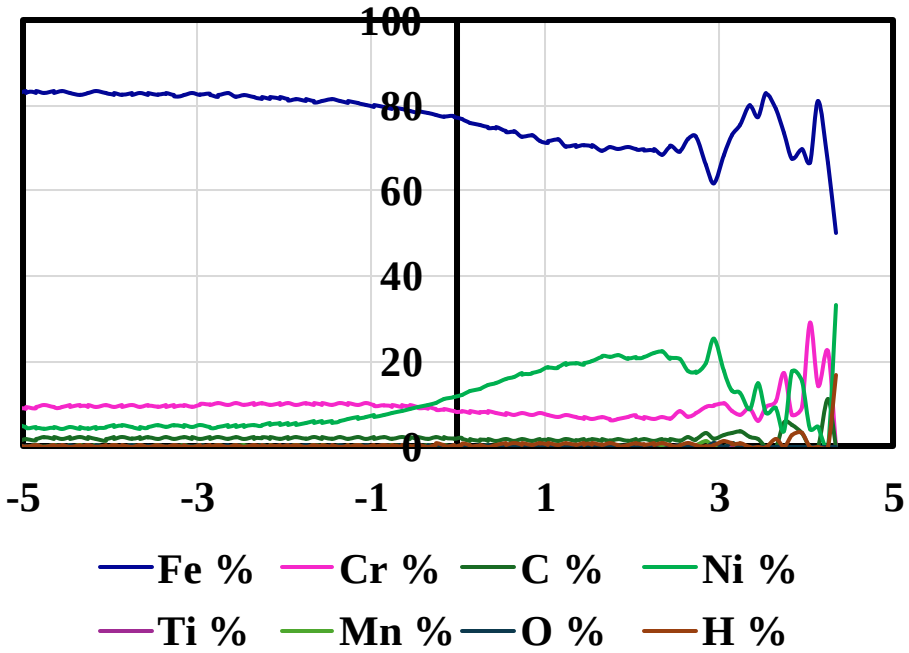

Proxigram across Ni 1.2 at.% isosurface

0D Dispersoid

15Cr-7Ni Steel + 1 vol% TiC

> 1 dpa, before deformation

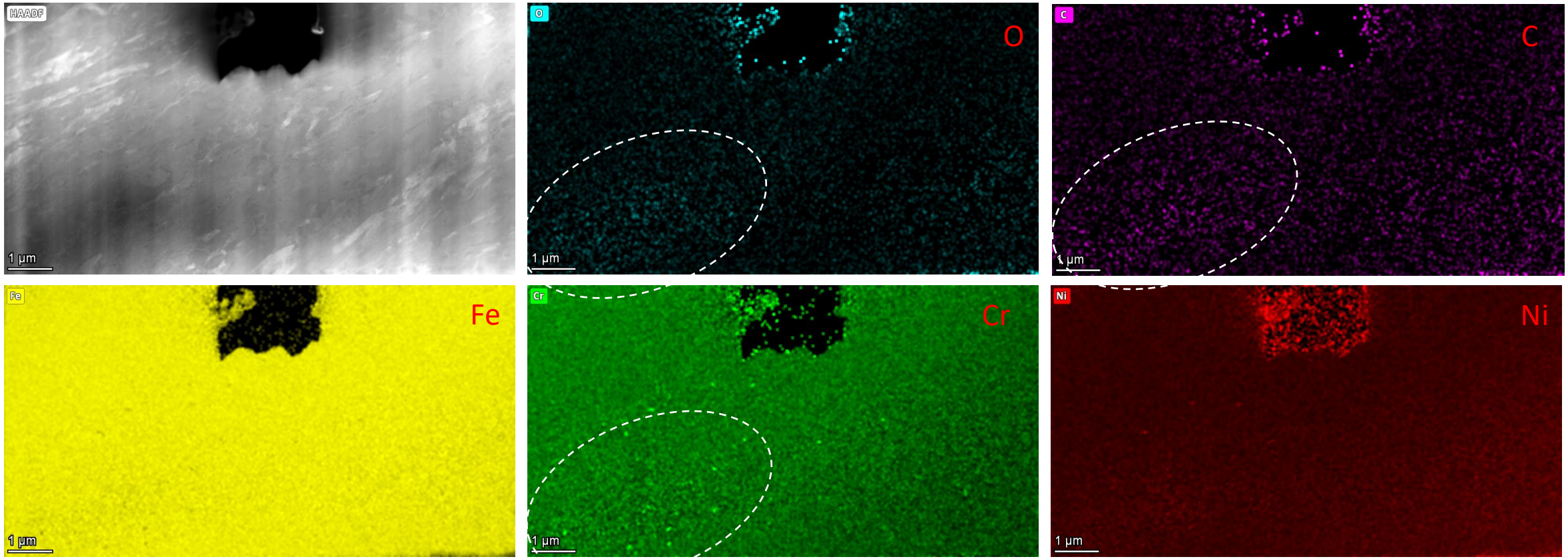

That being said, oxygen and carbon contents were richer in regions exhibiting segregation at a larger scale.

0D Dispersoid

15Cr-7Ni Steel + 1 vol% TiC

> 1 dpa, before deformation

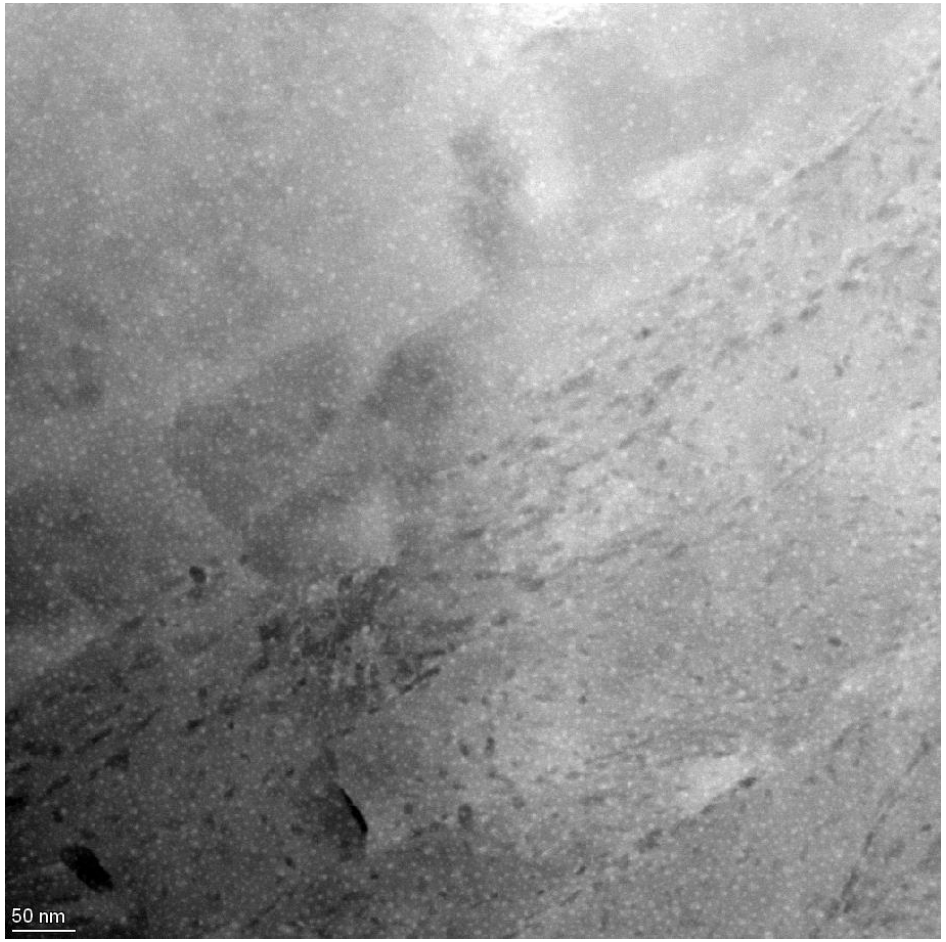

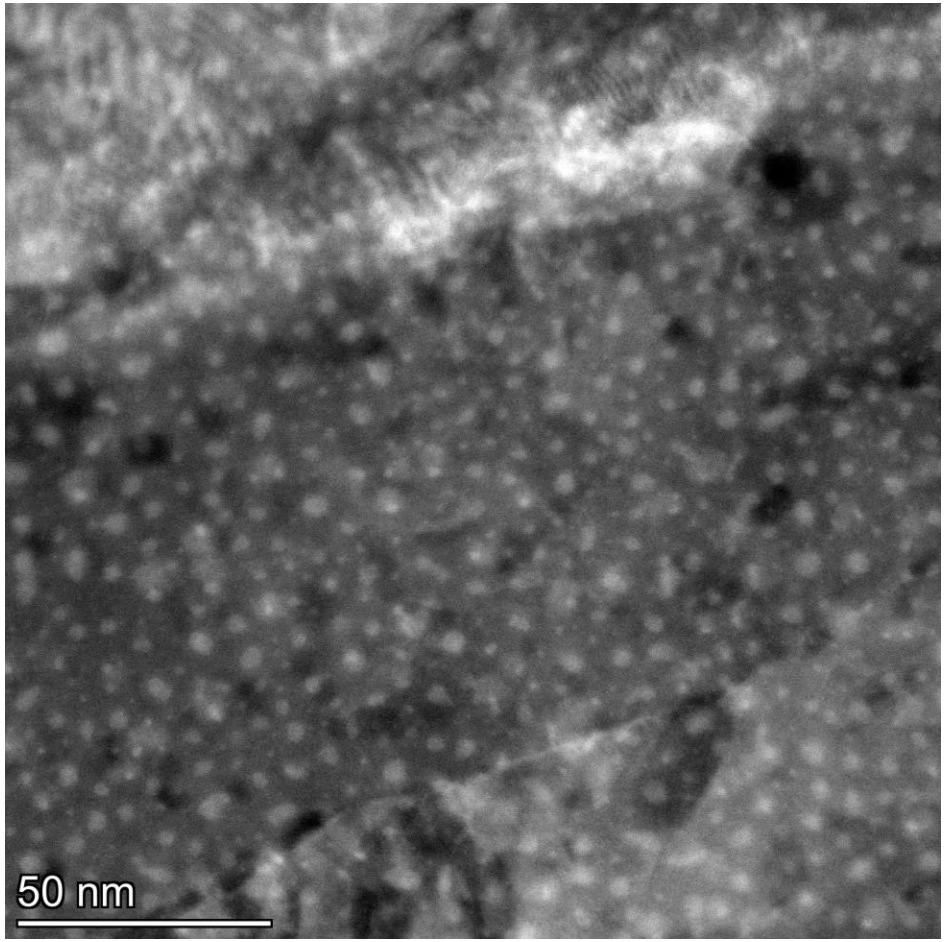

Voids with a diameter of a few nanometers formed upon irradiation
This material, however, showed tolerance to radiation

E. Tekoglu, A.D. O'Brien, J. Liu, B-M. Wang, S. Kavak, Y. Zhang, S.Y. Kim, S-T. Wang, D. Agaogullari, W. Chen, A.J. Hart and J. Li, "**Strengthening additively manufactured Inconel 718 through in-situ formation of nanocarbides and silicides**," *Additive Manufacturing* **67** (2023) 103478.

E. Tekoglu, A.D. O'Brien, Jong-Soo Bae, Kwang-Hyeok Lim, Jian Liu, Sina Kavak, Yong Zhang, So Yeon Kim, Duygu Agaogullari, Wen Chen, A. John Hart, Gi-Dong Sim, Ju Li, "**Metal Matrix Composite with Superior Ductility at 800 ºC: 3D Printed In718+ZrB_2 by Laser Powder Bed Fusion**," *Composites Part B* **268** (2024) 111052

Commercial metal AM system EOS M290 **SLM** printing system for powder bed fusion

Optomec LENS 450 is also used to implement DED printing

In718+SiC Composite Powder Production

Inconel 718

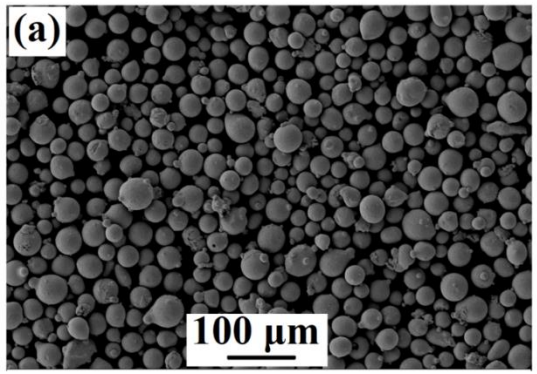

SiC Nanowires

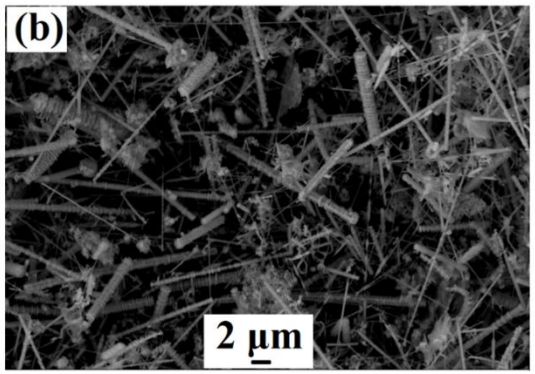

In718 + 2 vol% SiC

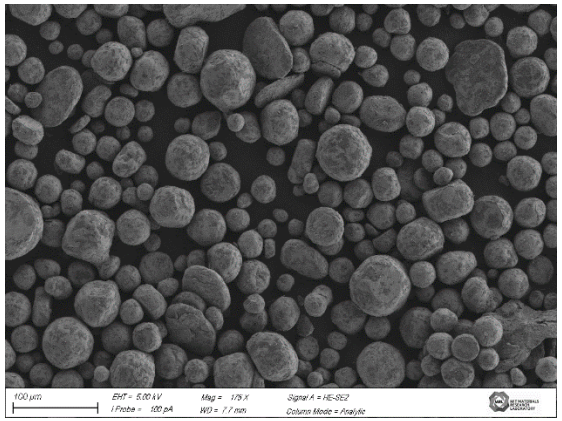

TEM EDX of FIB'ed single particle post-milling

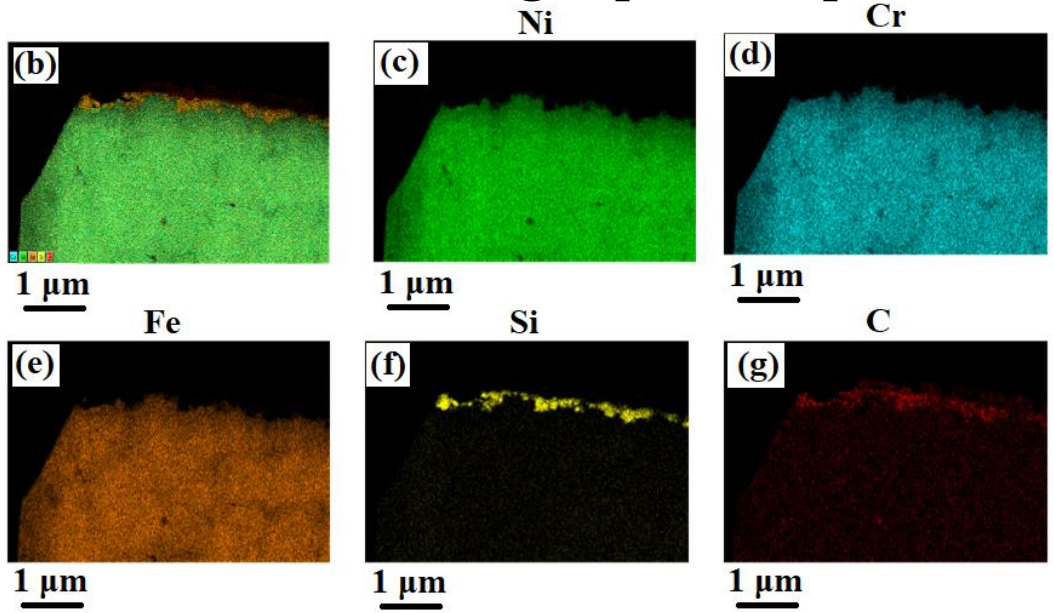

RT tensile properties of In718+SiC

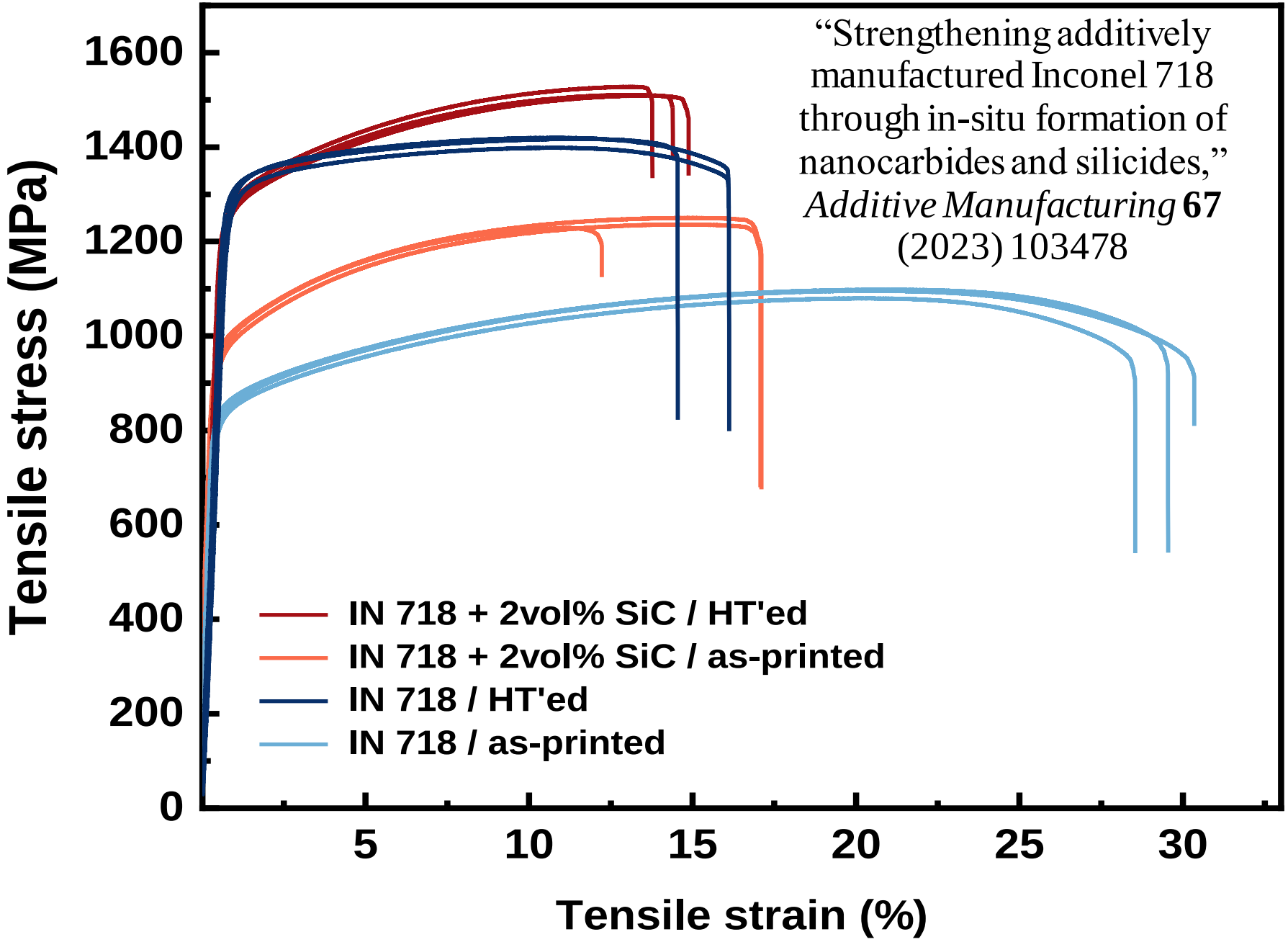

LPBF of In718+ZrB_2

E. Tekoglu, A.D. O'Brien, Jong-Soo Bae, Kwang-Hyeok Lim, Jian Liu, Sina Kavak, Yong Zhang, So Yeon Kim, Duygu Agaogullari, Wen Chen, A. John Hart, Gi-Dong Sim, Ju Li, "**Metal Matrix Composite with Superior Ductility at 800 ºC: 3D Printed In718+ZrB_2 by Laser Powder Bed Fusion**," *Composites Part B: Engineering* **268** (2024) 111052

Unlike Boron-10 with a gigantic thermal neutron capture cross-section of **3980 barn**, Boron-11 has a thermal neutron capture cross-section of only **0.005 barn**

Yunsong Jung and Ju Li, "Boron-10 stimulated helium production and accelerated radiation displacements for rapid development of fusion structural materials," *Journal of Materiomics* **10** (2024) 377-385

Fabrication of $In718+ZrB_2$

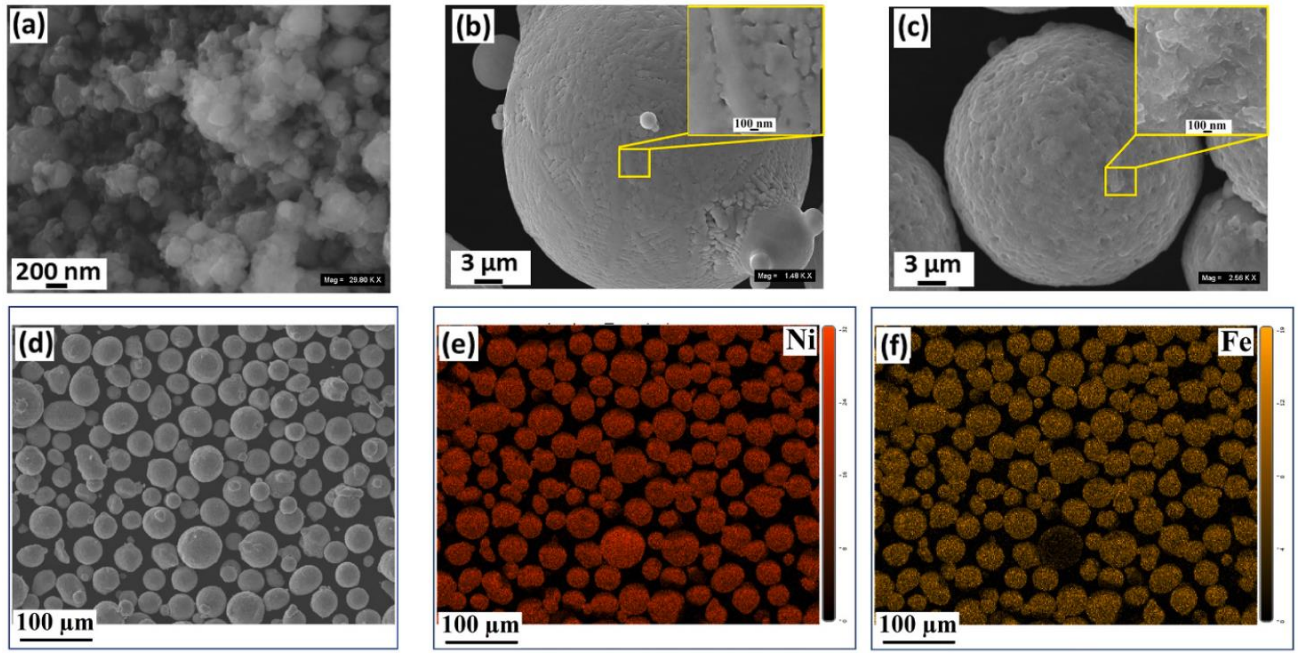

(a) commercial ZrB_2 powders, **(b)** In718 particle surface before blending, **(c)** ZrB_2 decorated In718 particle surface after blending. **(d-f)** SEM micrographs and EDX mappings of In718 + ZrB_2 powders after blending.

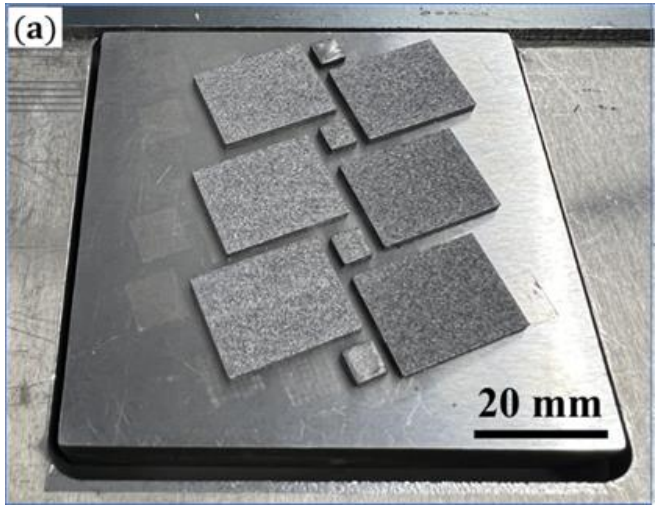

$In718+ZrB_2$ samples printed at EOS M290

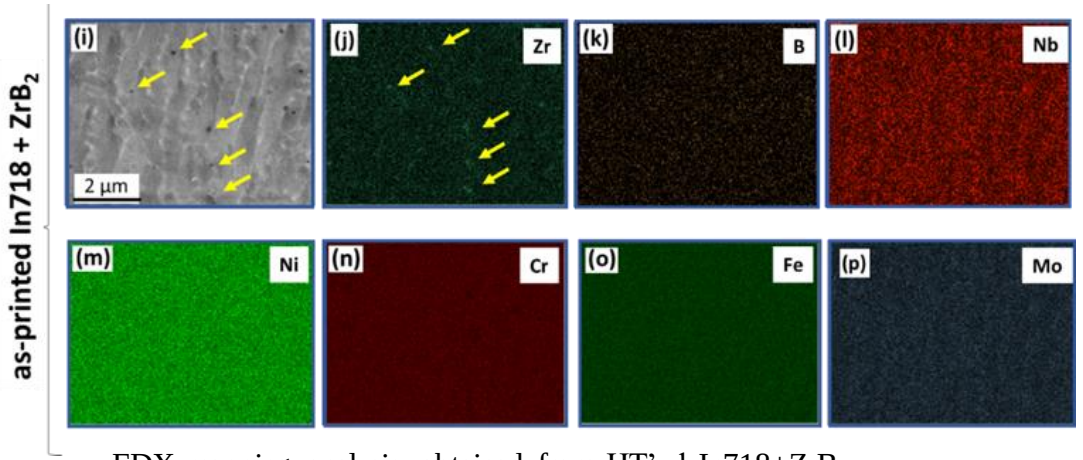

EDX mapping analysis obtained from HT'ed $In718+ZrB_2$ (yellow arrows indicate Zr-rich regions).

CT reconstructions of In718 vs In718+ZrB_2

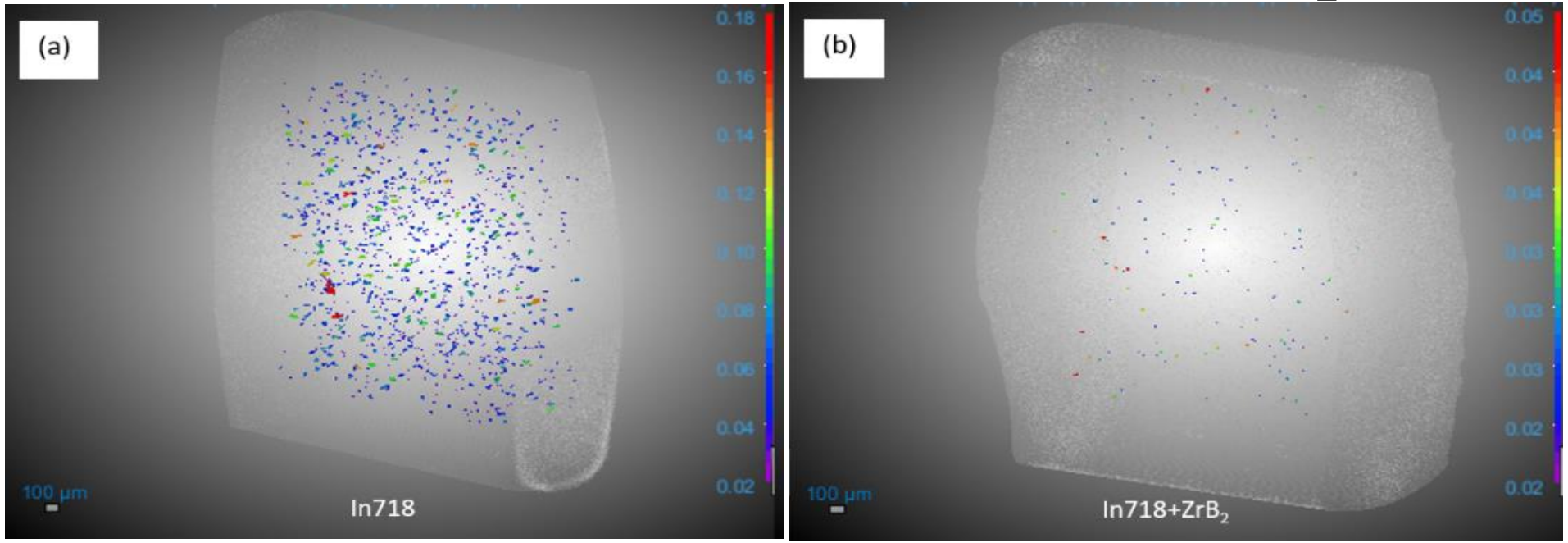

Xradia 620 Versa X-ray CT

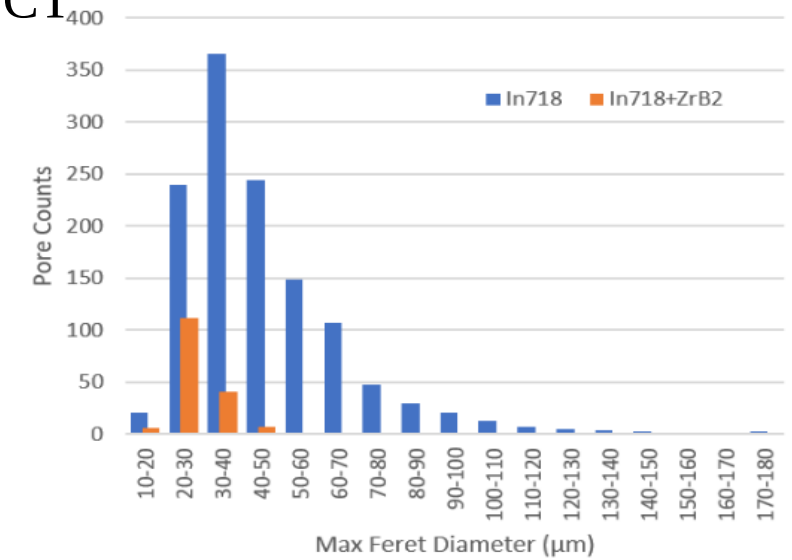

X-ray CT reconstructions displaying pores with diameters >20µm formed during printing of **(a)** In718 and **(b)** In718+ZrB_2 samples. **(c)** Histogram of pore counts for unfortified and fortified samples organized by maximum Feret diameter.

RT tensile properties of In718+ZrB_2

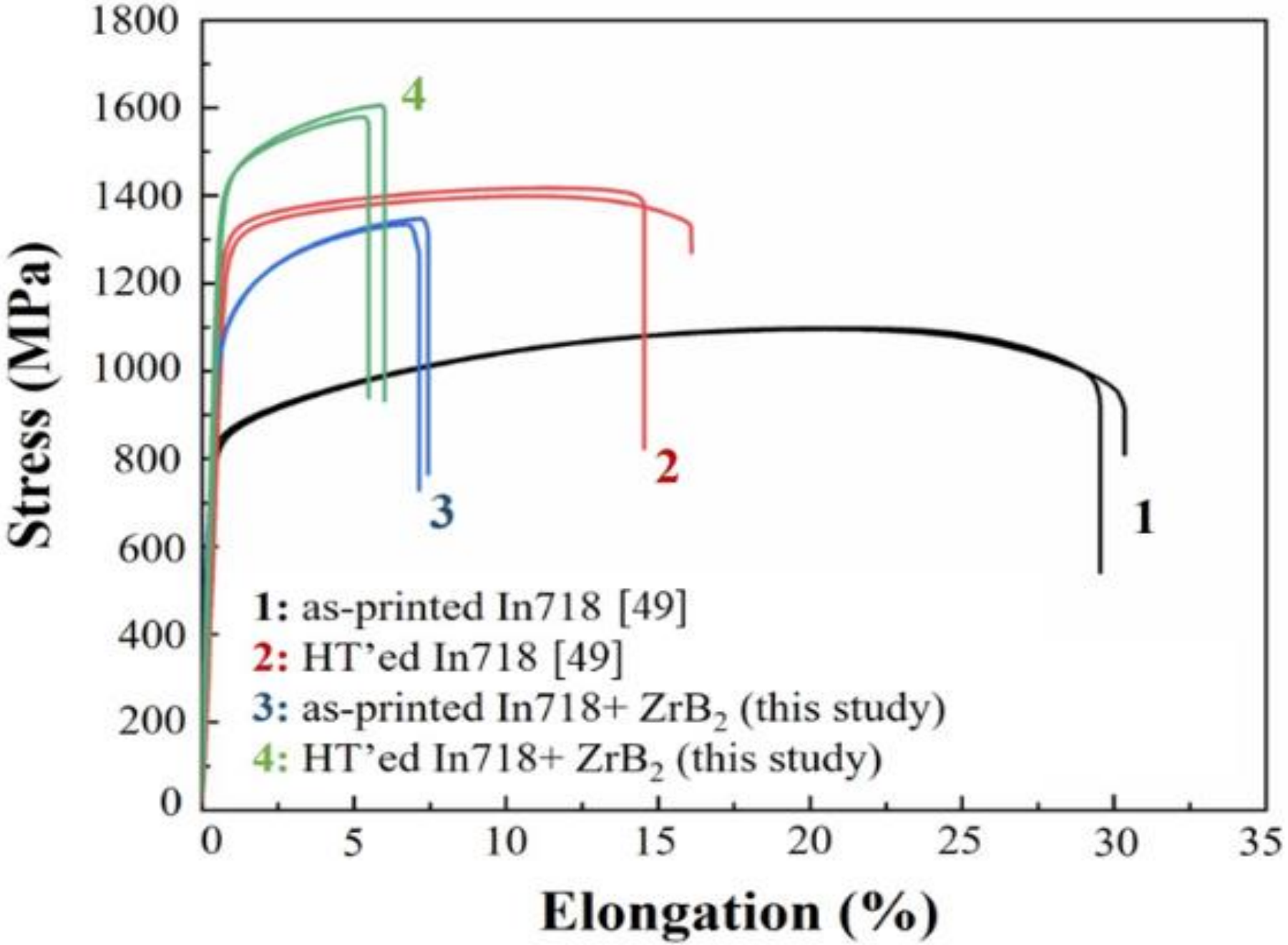

EBSD analysis

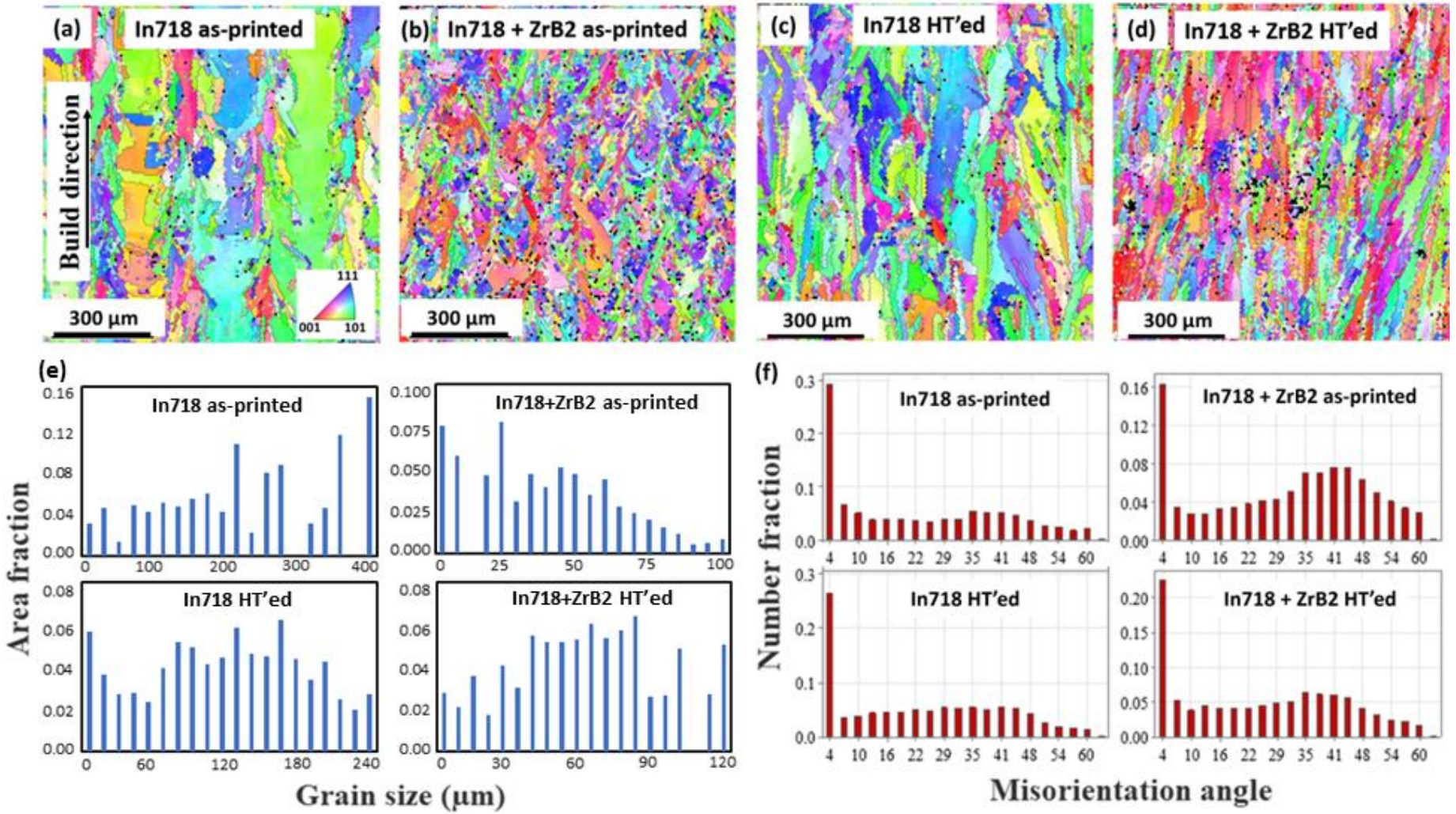

(a-d) EBSD orientation maps obtained from LPBF'ed samples and corresponding **(e)** grain size distribution and **(f)** misorientation angle distribution plots.

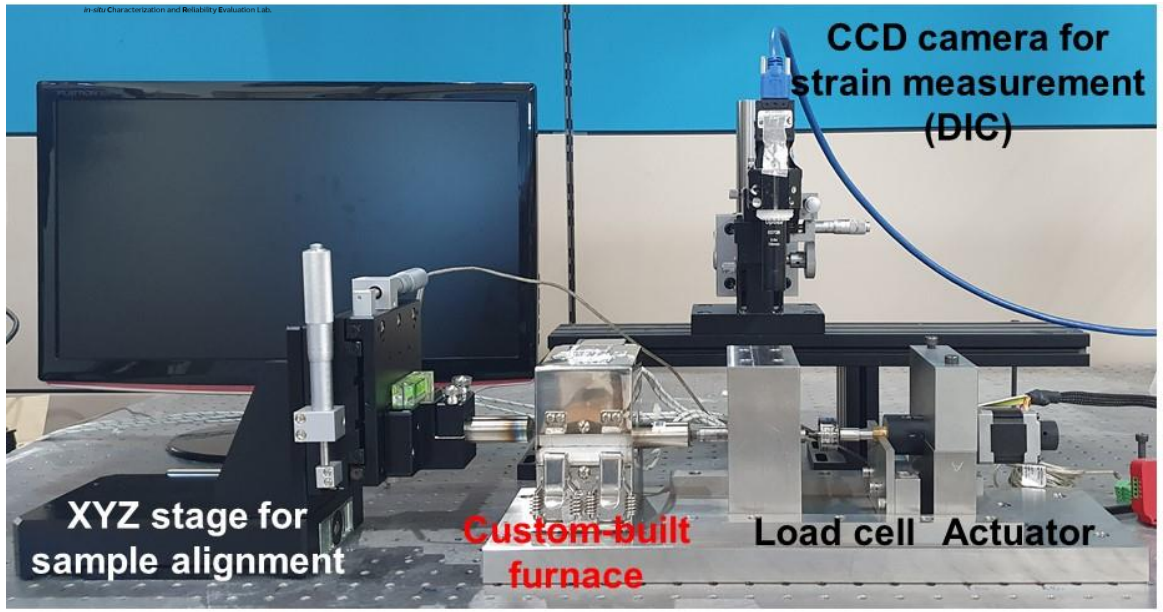

Custom-Built Mesoscale Mechanical Tester

- Load capacity: 125 N
- Temperature limit: 800 ℃
- Displacement range: 0 ~ 13 mm

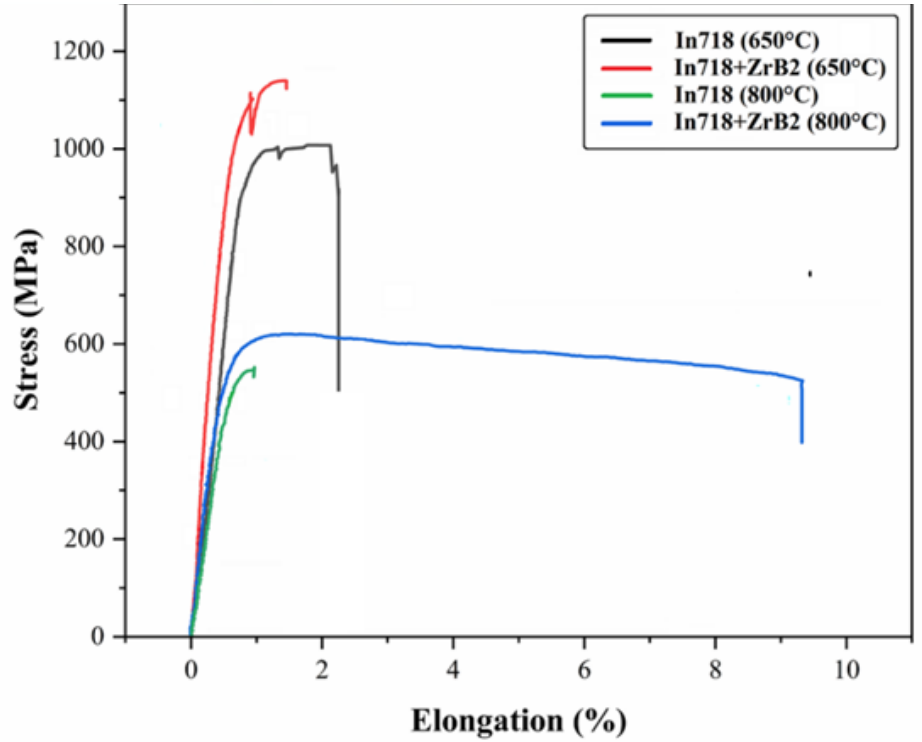

Collaboration with Prof. Gi-Dong Sim at KAIST

Sample	HT'ed In718	HT'ed In718+ZrB_2
650 ºC σ_{YS} (MPa)	983.4	1086.7
650 ºC σ_{UTS} (MPa)	1008.0	1162.3
650 ºC Elongation (%)	2.1	1.5
800 ºC σ_{YS} (MPa)	501.3	552.2
800 ºC σ_{UTS} (MPa)	556.2	603.1
800 ºC Elongation (%)	1.0	9.2

Improvement of Ductility Dip at 800˚C

Deformed In718+ZrB_2 at 800 °C

(Collaboration with Prof. Gi-Dong Sim at KAIST)

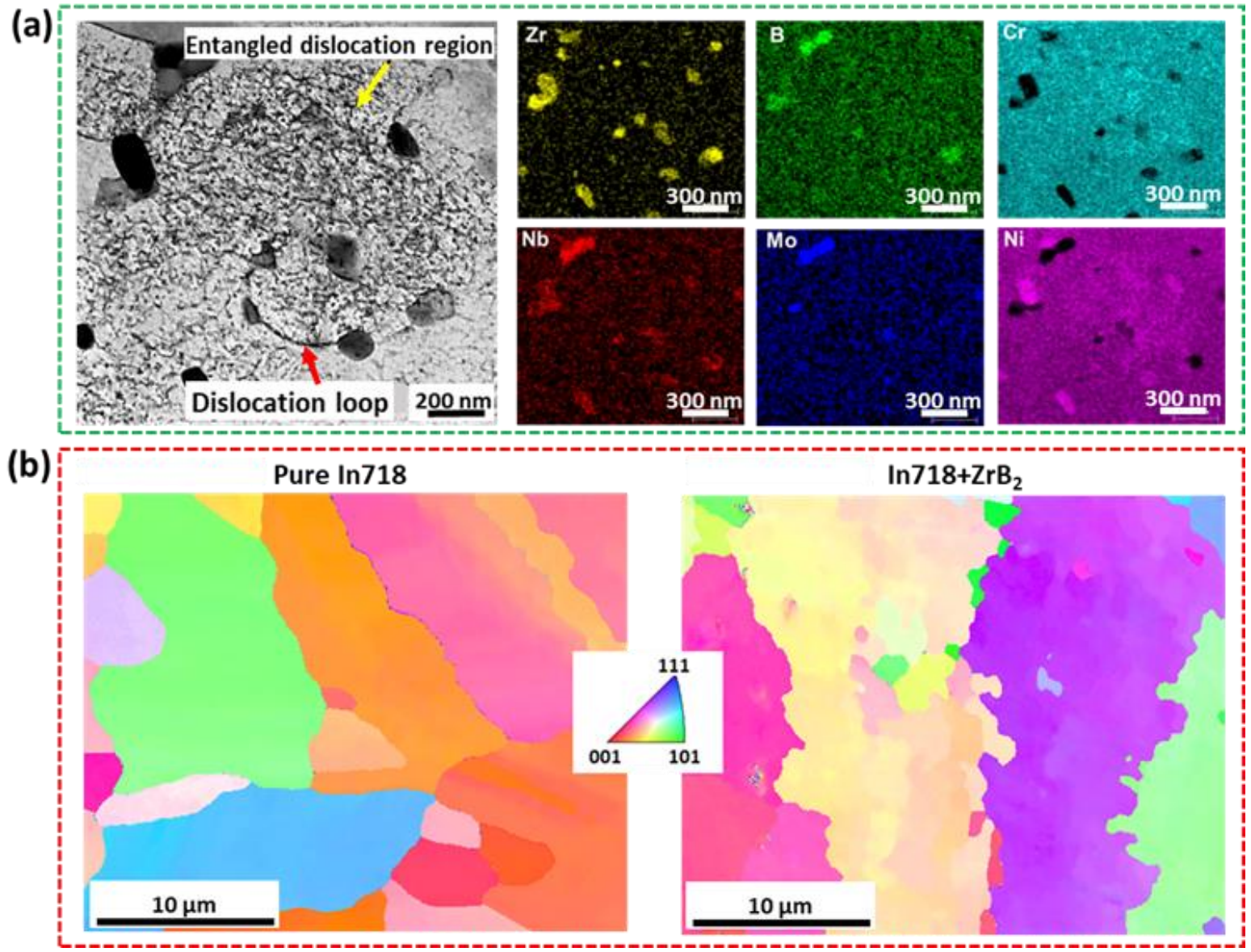

(a) STEM image and EDX mapping obtained from HT'ed In718+ZrB_2 after 800°C tensile test showing dislocation loop and entanglement in the microstructure and **(b)** EBSD maps obtained from HT'ed In718 and In718+ZrB_2 showing the difference of grain boundary morphologies.

LPBF of In939+TiB_2

Emre Tekoglu, Jong-Soo Bae, Mohammed Alrizqi, Alexander D. O'Brien, Jian Liu, Krista Biggs, So Yeon Kim, Aubrey Penn, Ivo Sulak, Wen Chen, Kang Pyo So, Gi-Dong Sim, A. John Hart , Ju Li, "**Additive manufacturing of crack-free, strong and ductile In939+TiB2 by Laser Powder Bed Fusion**,"
to be submitted

In939-based composites

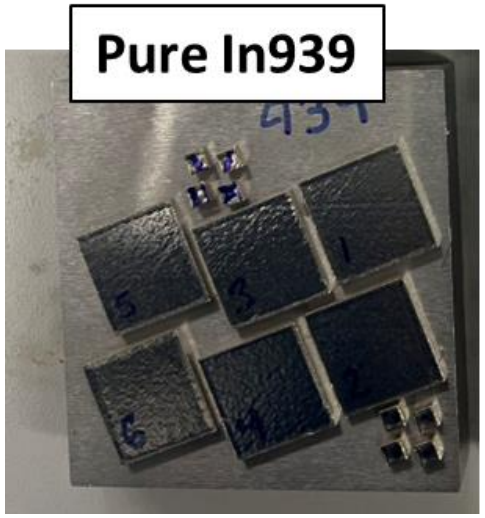

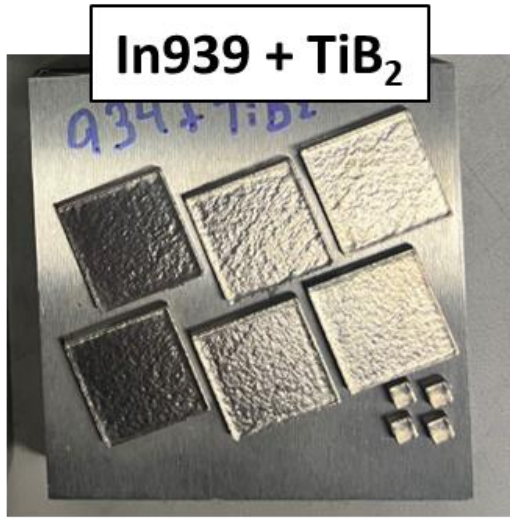

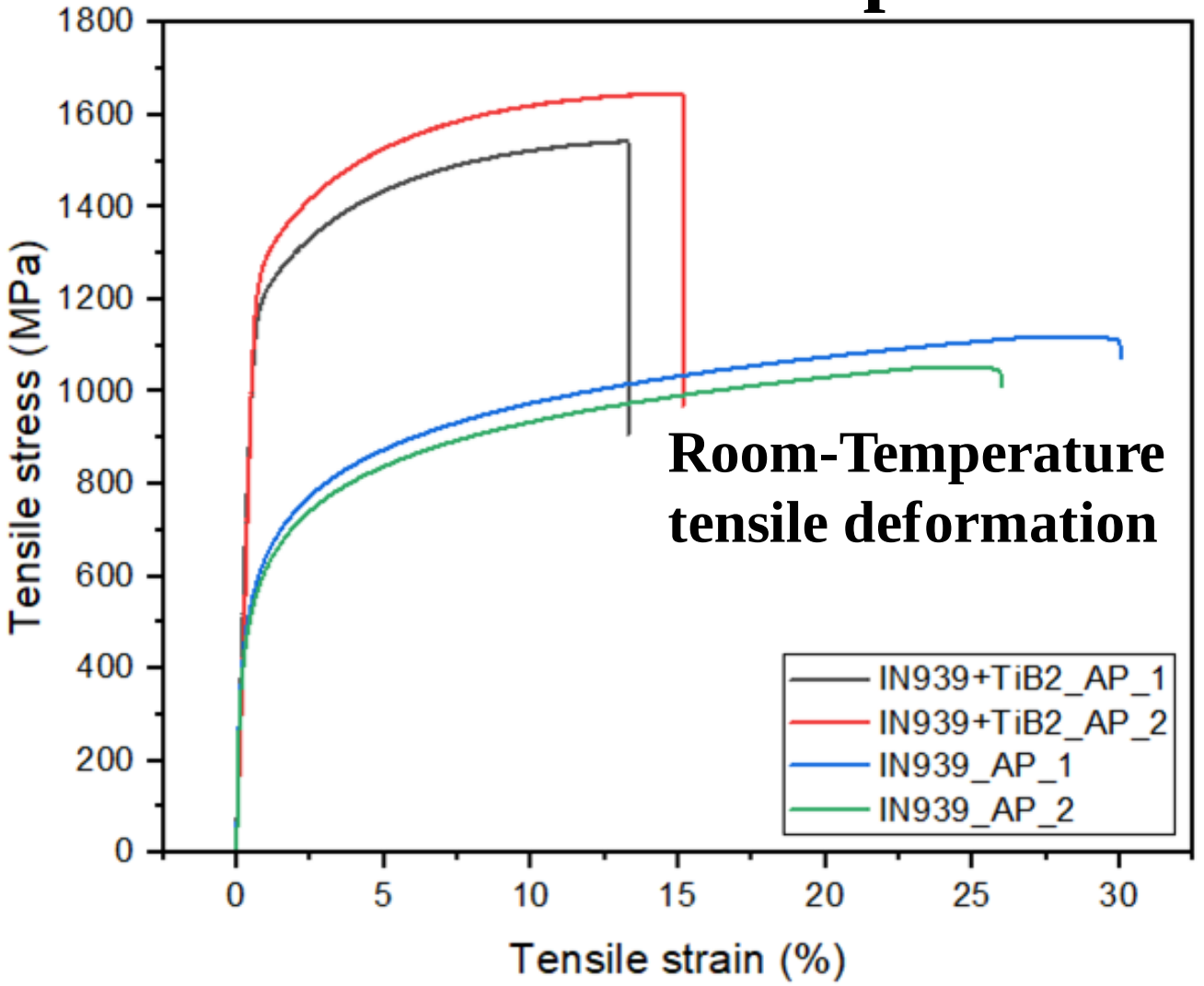

Fabrication of In939-based composites

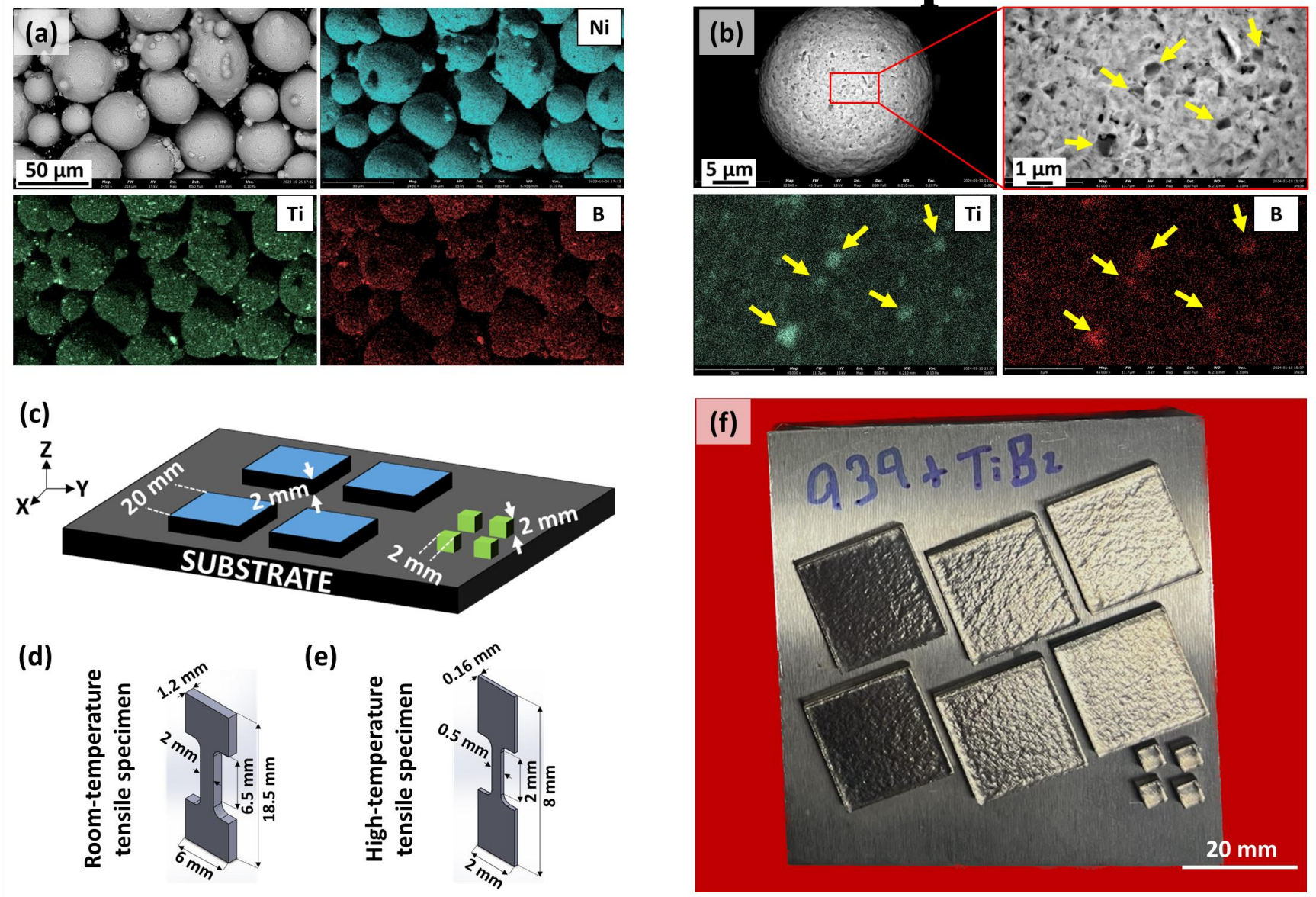

(a, b) SEM micrographs and EDX mapping analysis of In939 particles decorated with TiB_2 after blending. **(c)** Illustration of samples produced via LPBF. **(d)** Geometry and dimensions of room-temperature tensile specimens machined by wire EDM. **(e)** Geometry and dimensions of high-temperature tensile specimens machined by wire EDM. **(f)** In939+TiB_2 samples fabricated by LPBF using the EOS M290 system, shown prior to removal from the build plates.

LPBF parameter optimization

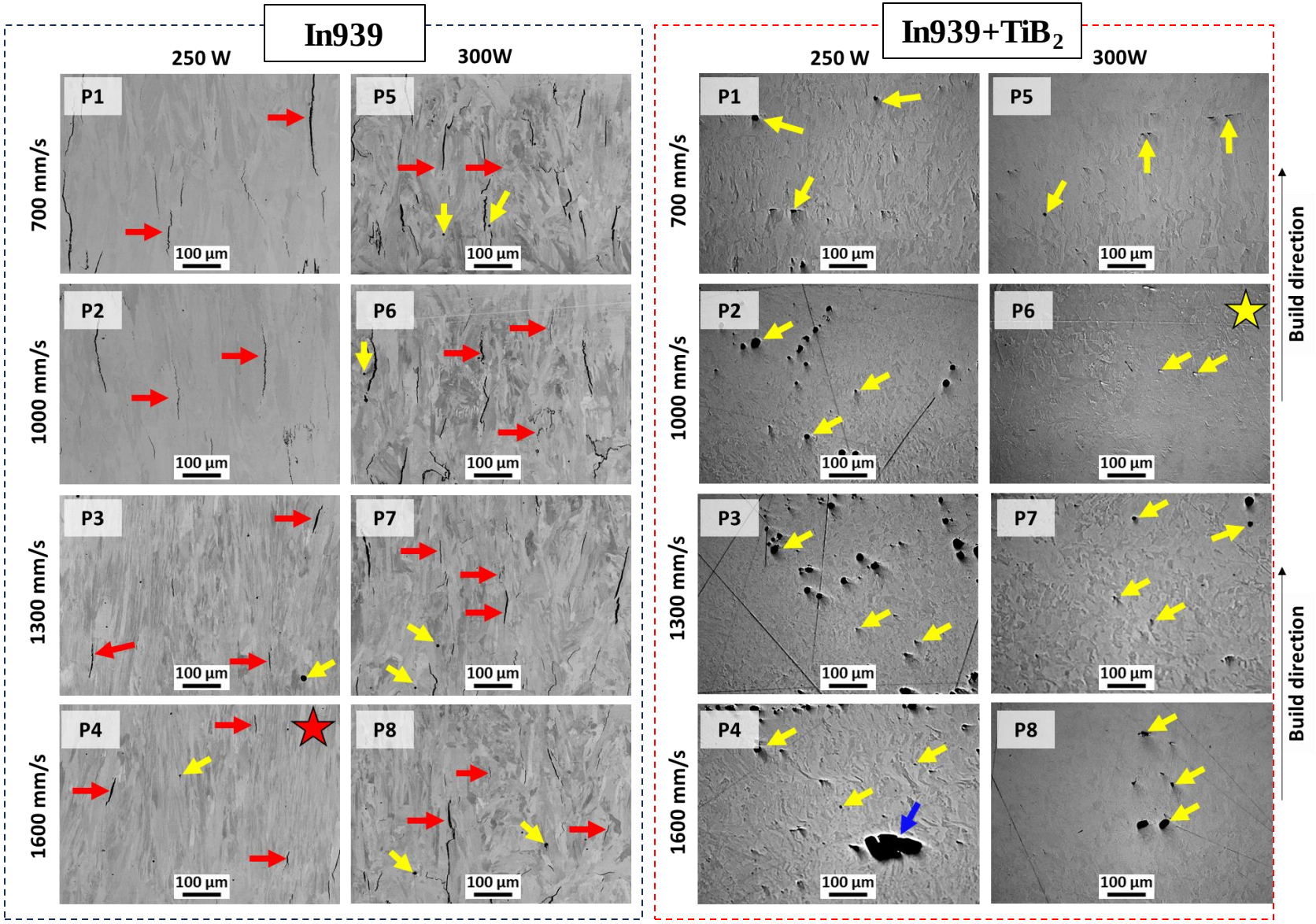

SEM images of LPBF'ed samples of both In939 and In939+TiB_2 under varying laser power and scan speed. The images demonstrate that the addition of TiB_2 particles notably inhibits cracking, as evident in the cross-sectional SEM images. Cracks and porosities are highlighted using red and yellow arrows, respectively.

Hot-tearing crack

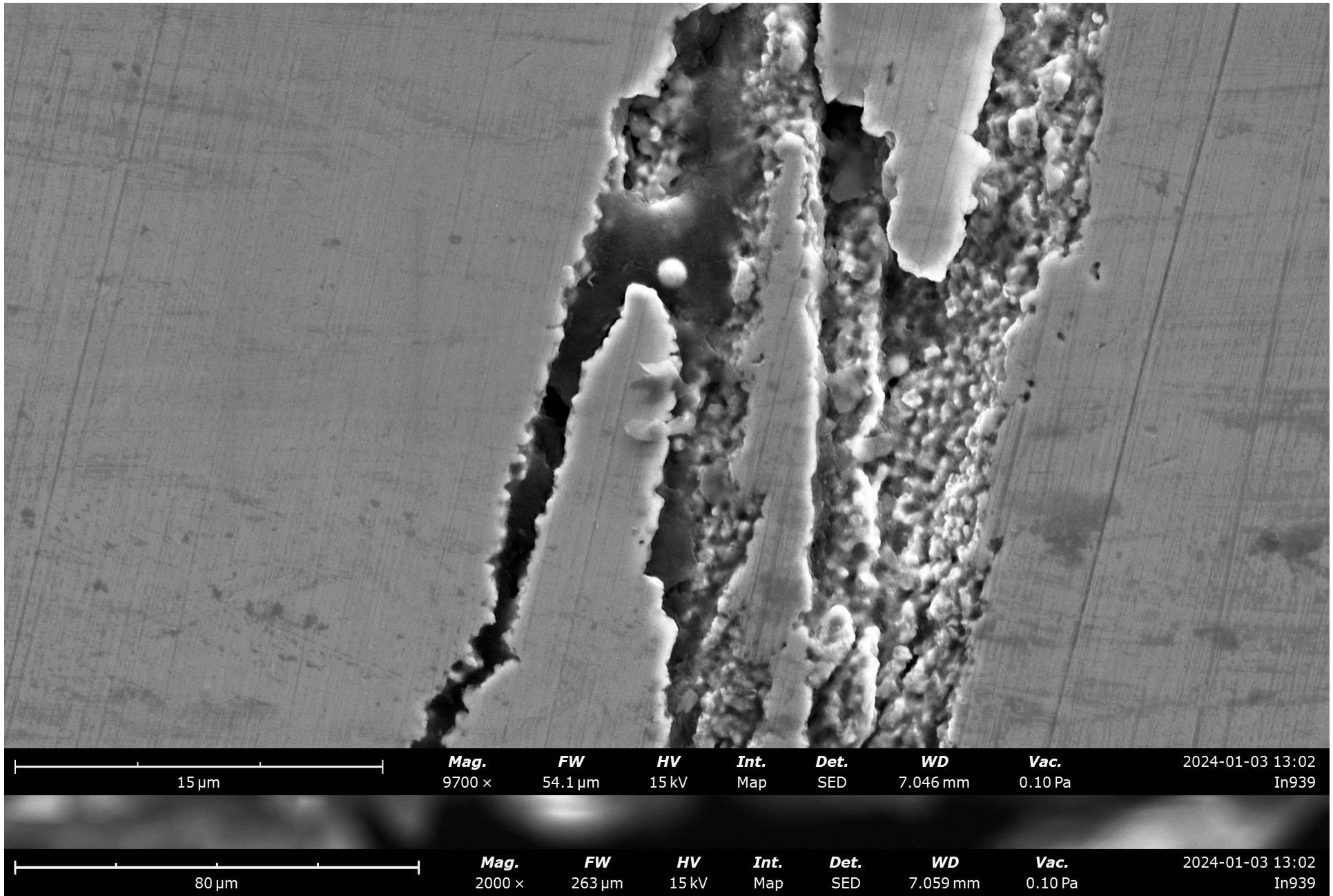

Defect distribution in LPBF optimized specimens

LPBF-optimized In939

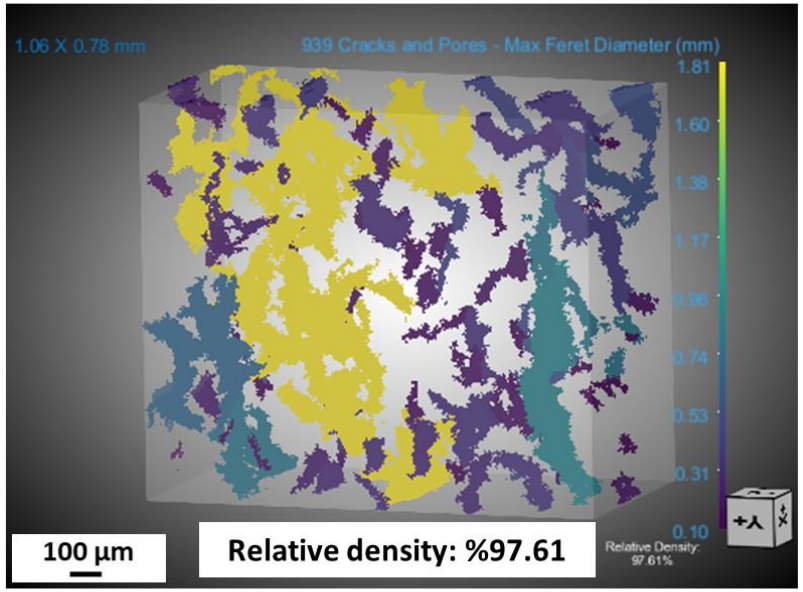

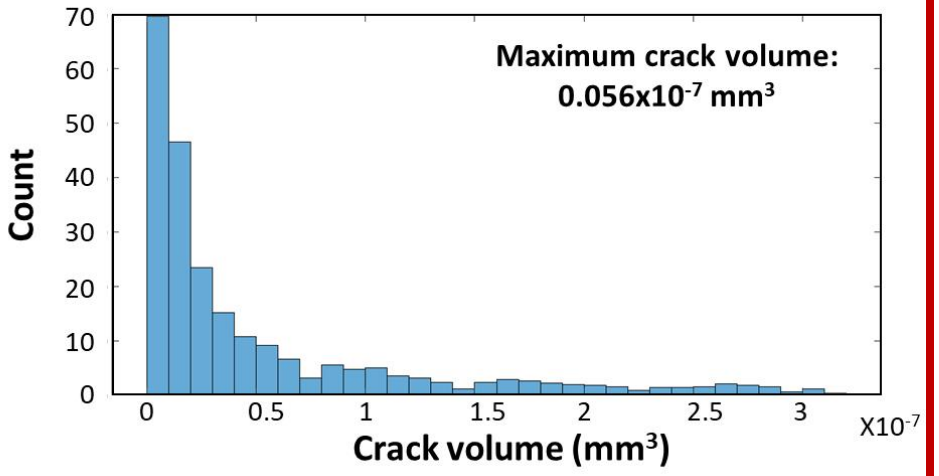

LPBF-optimized In939+TiB_2

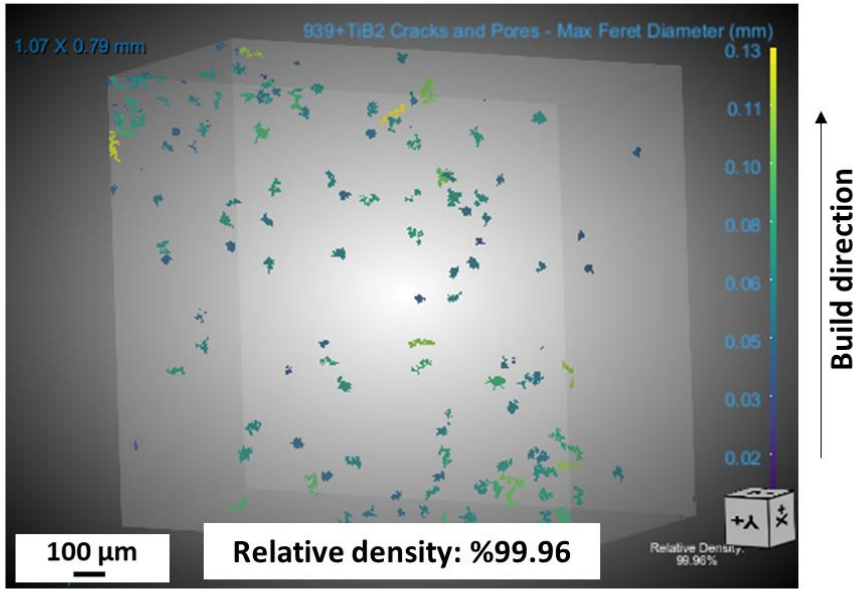

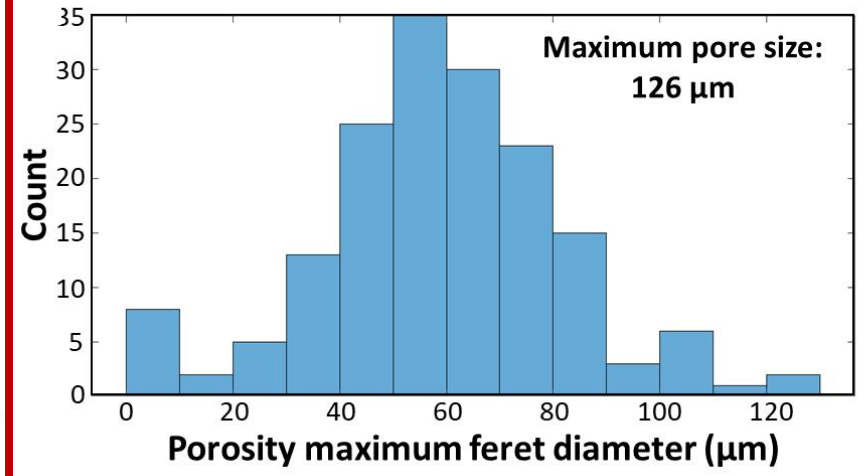

Summary of defect formation in the three alloys.

	Cracking			Porosity	Lack of fusion
	Solidification	Liquation	Solid state		
ABD-850AM	N	N	N	Y	Y
CM247LC	Y	Y	Y	Y	Y
IN939	Y	N	Y	Y	Y

(i) solidification cracking (hot-tearing crack)
(ii) liquation cracking (GB liquid film)
(iii) solid-state cracking (strain-age crack (SAC), ductility dip crack (DDC), >100um crack).

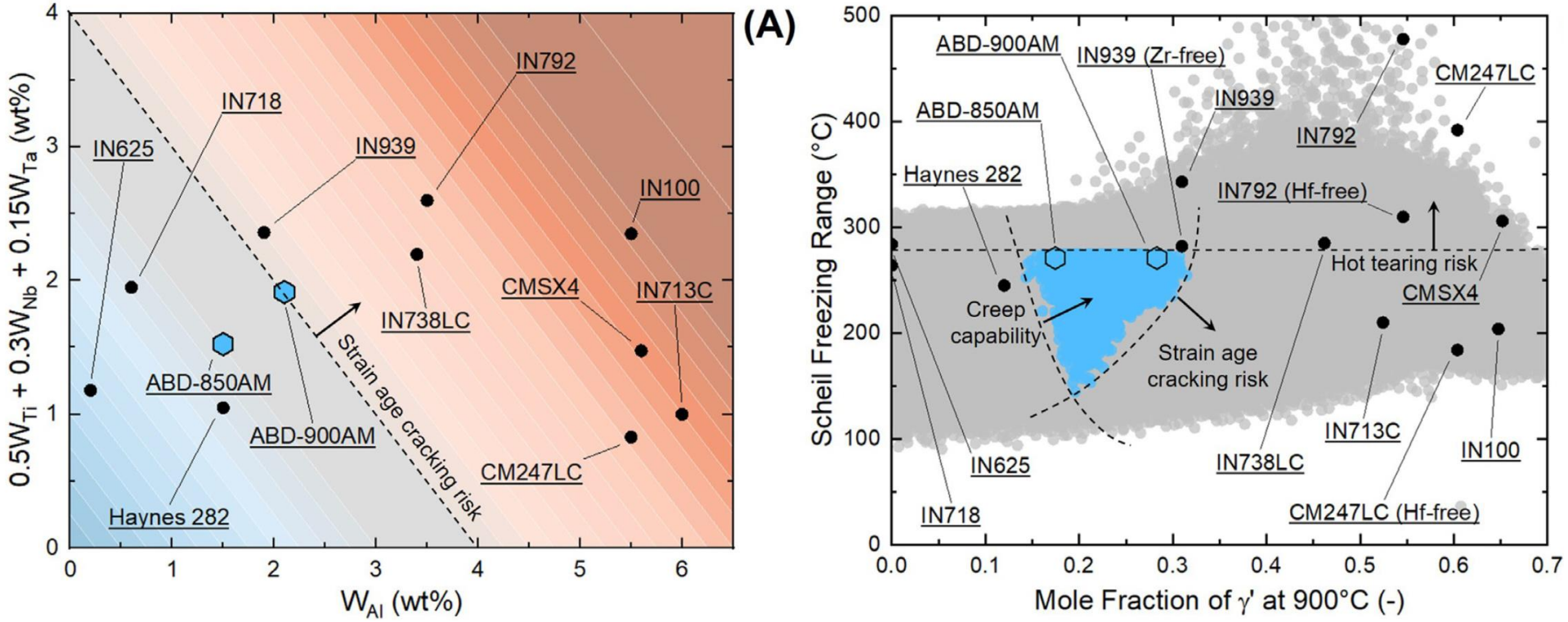

Yuanbo T. Tang, Chinnapat Panwisawas, Joseph N. Ghoussoub, Yilun Gong, John W.G. Clark, André A.N. Németh, D. Graham McCartney, Roger C. Reed, "**Alloys-by-design: Application to new superalloys for additive manufacturing**," *Acta Materialia* **202** (2021) 417.

Cracking susceptibility coefficient (CSC) assessment through Thermo-Calc

$$CSC = \frac{t(0.99) - t(0.9)}{t(0.9) - t(0.4)} \approx \frac{T(0.9) - T(0.99)}{T(0.4) - T(0.9)}$$

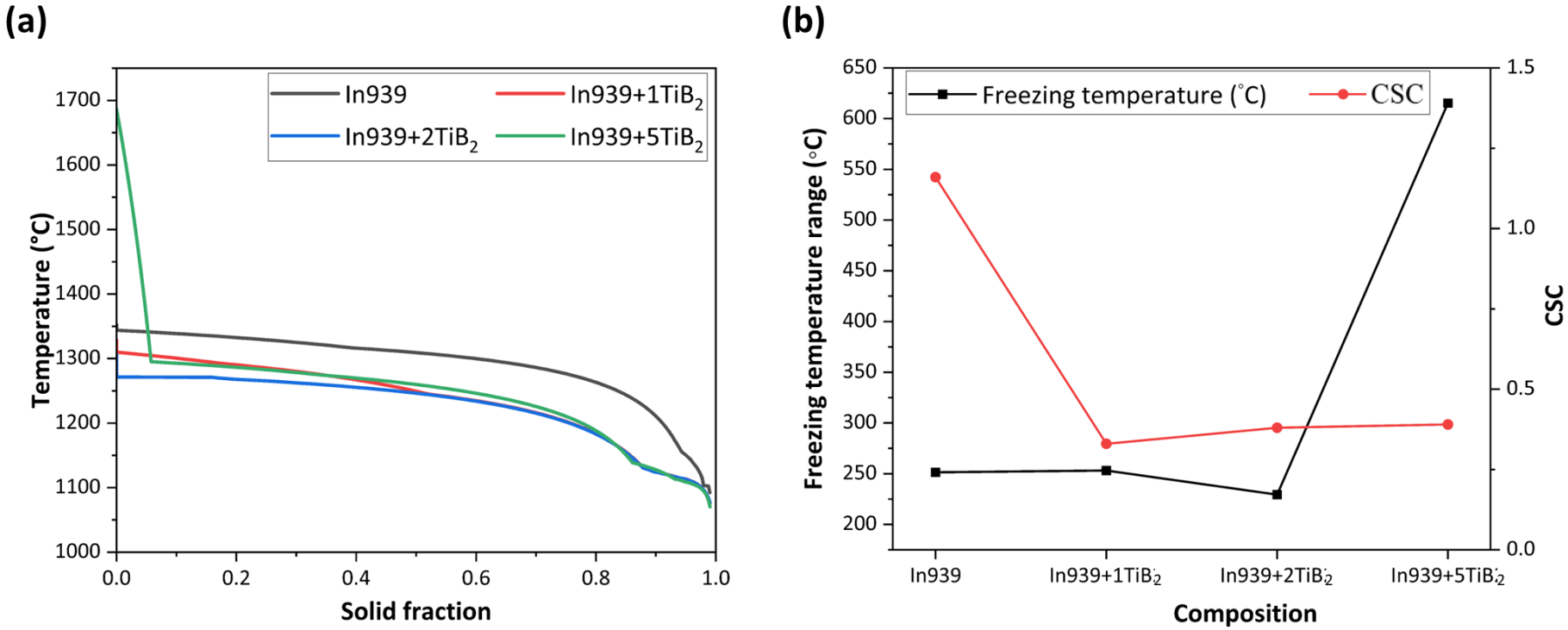

(a) Scheil-Gulliver curves of In939 with different TiB_2 contents, and **(b)** Freezing temperature range and HCS values with respect to composite formulations (Scheil-Gulliver curves were plotted based on the Aziz model for solute trapping, which is designed for high solidification speeds in additive manufacturing).

High-temperature tensile performance of In939+TiB_2

(Collaboration with Prof. Gi-Dong Sim at KAIST)

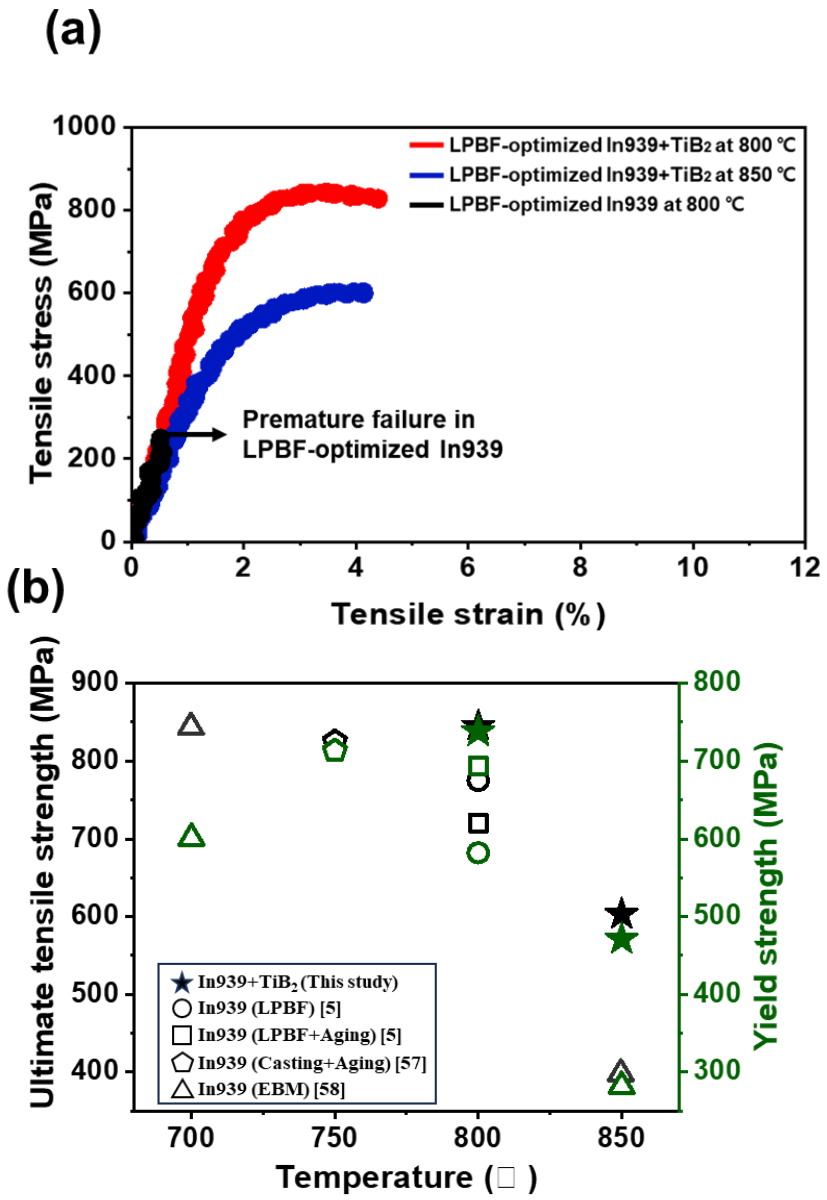

Superior high-temperature strengths of In939+TiB_2 compared to other In939 as reported in the literature

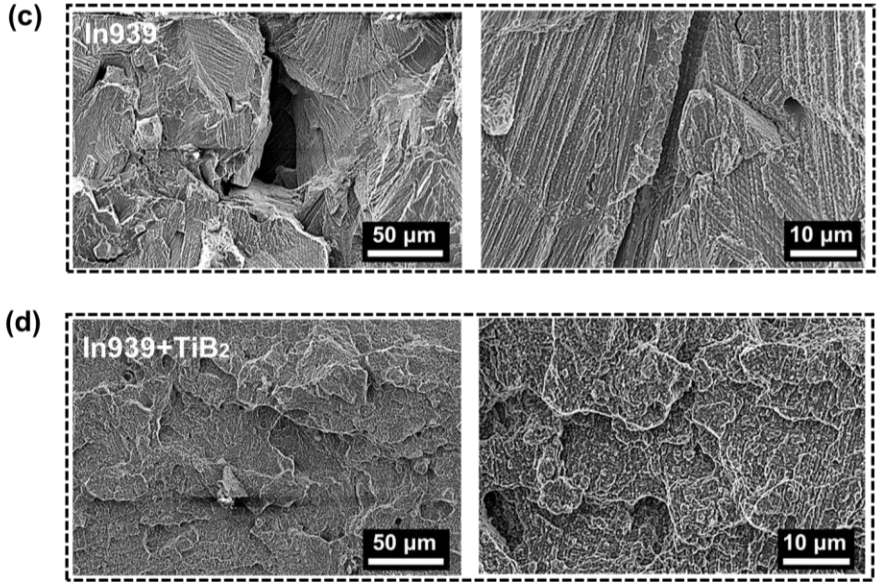

Fig. Fracture surfaces of **(c)** In939 and **(d)** In939+TiB_2 at 800 °C.

Comparison of 800 °C and 850 °C tensile properties of LPBF-optimized In939 + TiB_2 and other In939 materials from the literature.

Material	Condition	T (°C)	YS (MPa)	UTS (MPa)	El (%)
In939 [5]	LPBF	800	582	775	8
In939 [5]	LPBF+aging	800	694	720	9
In939 [58]	EBM	700	601	843	11
		850	282	397	7.5
In939 [57]	Casting + aging	750	713	825	3
In939+TiB_2	LPBF	800	738	845	4.3
		850	471	603	4.1

LPBF of In625-based MMCs

Emre Tekoglu, Jong-Soo Bae, Ho-a Kim, Kwang-Hyeok Lim, Jian Liu, So Yeon Kim, Aubrey Penn, Wen Chen, A. John Hart, Joo-Hee Kang, Chang-Seok Oh, Ji-Won Park, Fan Sun, Sangtae Kim, Gi-Dong Sim, Ju Li, "**Superior high-temperature mechanical properties and microstructural features of LPBF-printed In625-based metal matrix composites**" to be submitted (2024).

In625-based composites

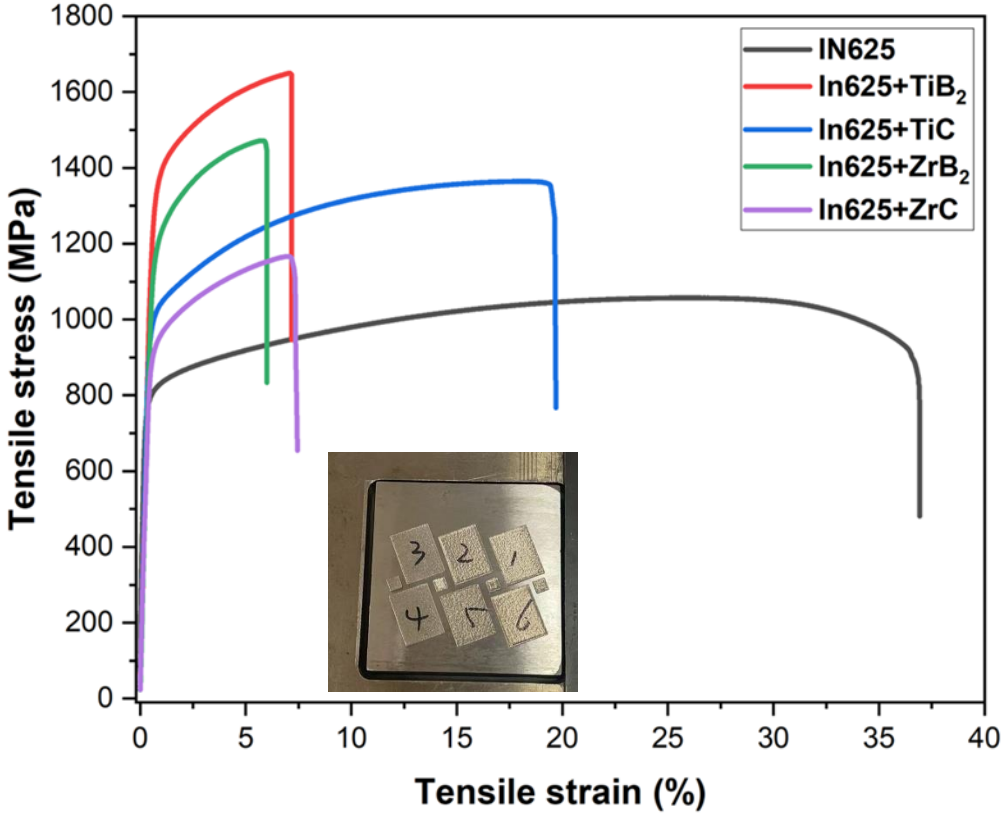

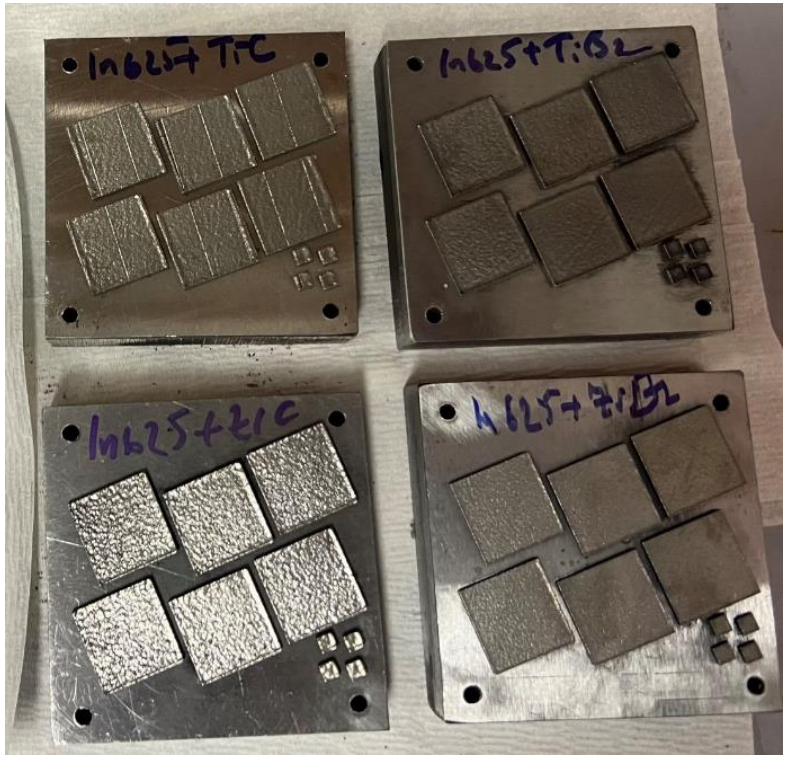

Fabrication of In625-based composites

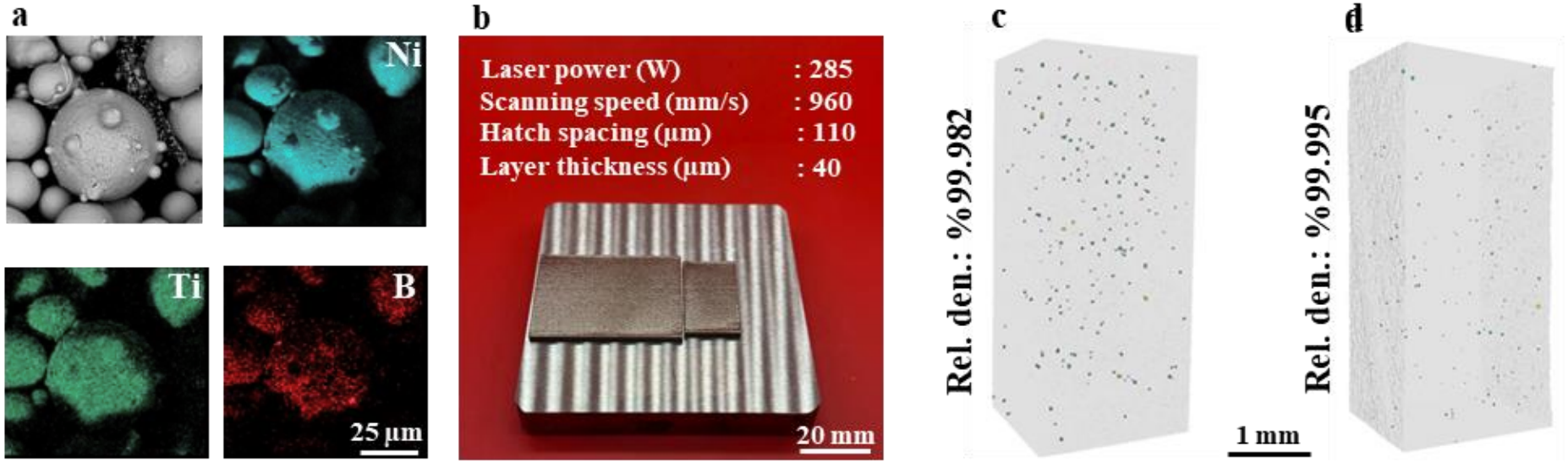

(a) SEM micrographs of TiB_2 decorated In625 particles after blending**, (b)** In625+TiB_2 samples fabricated by LPBF using EOS M290 system, shown prior to removal from the build plates, **(c-d)** 3D CT reconstructions displaying pores formed during printing of In625 and In625+TiB_2 samples

RT tensile properties of In625-based MMCs

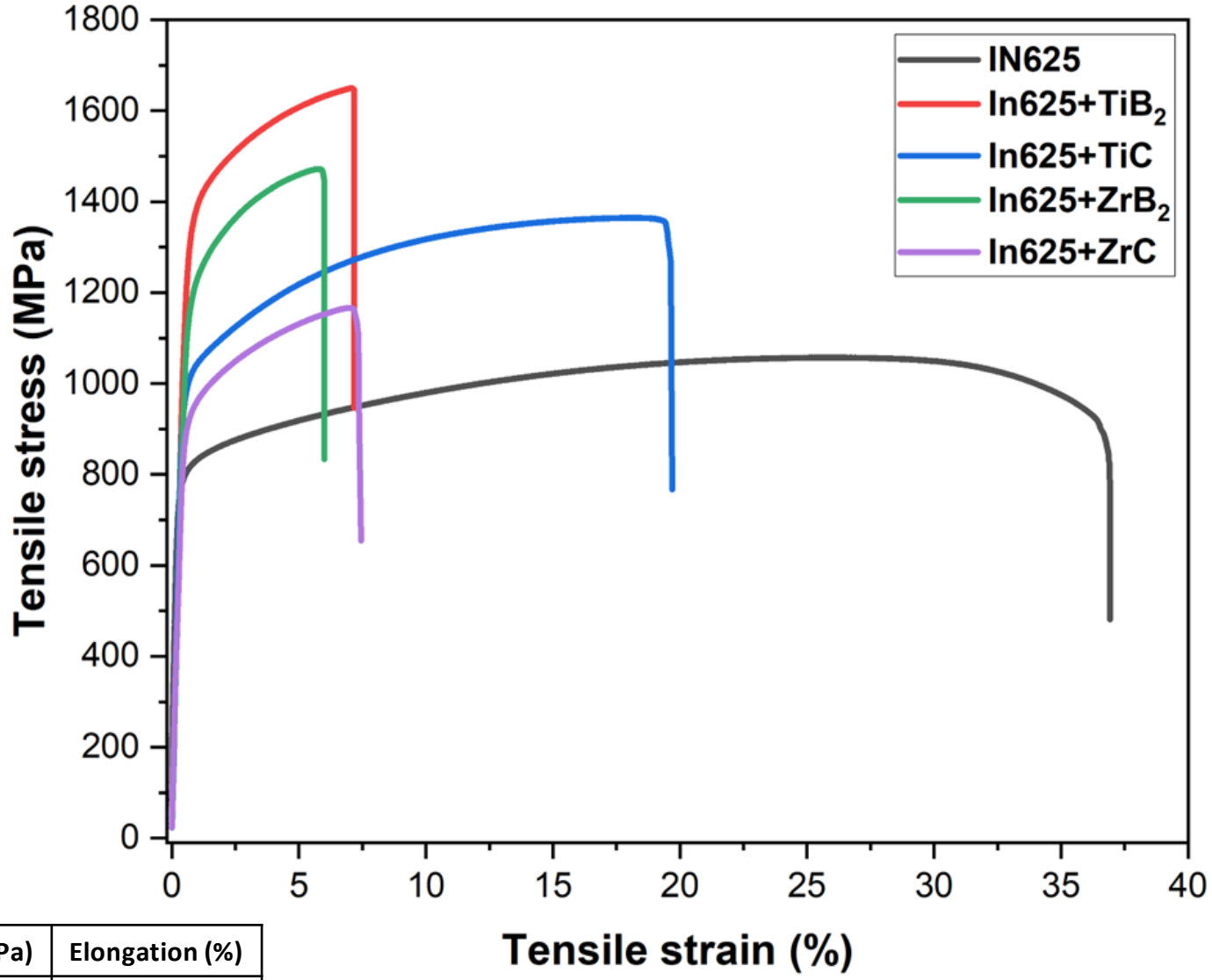

Sample	σ_{YS} (MPa)	σ_{UTS} (MPa)	Elongation (%)
In625	841	1054	36.9
In625+TiB_2	1386	1649	7.2
In625+TiC	1093	1364	19.7
In625+ZrB_2	1297	1471	6
In625+ZrC	998	1165	7.5

High-temperature tensile properties of In625-based MMCs

(Collaboration with Prof. Gi-Dong Sim at KAIST)

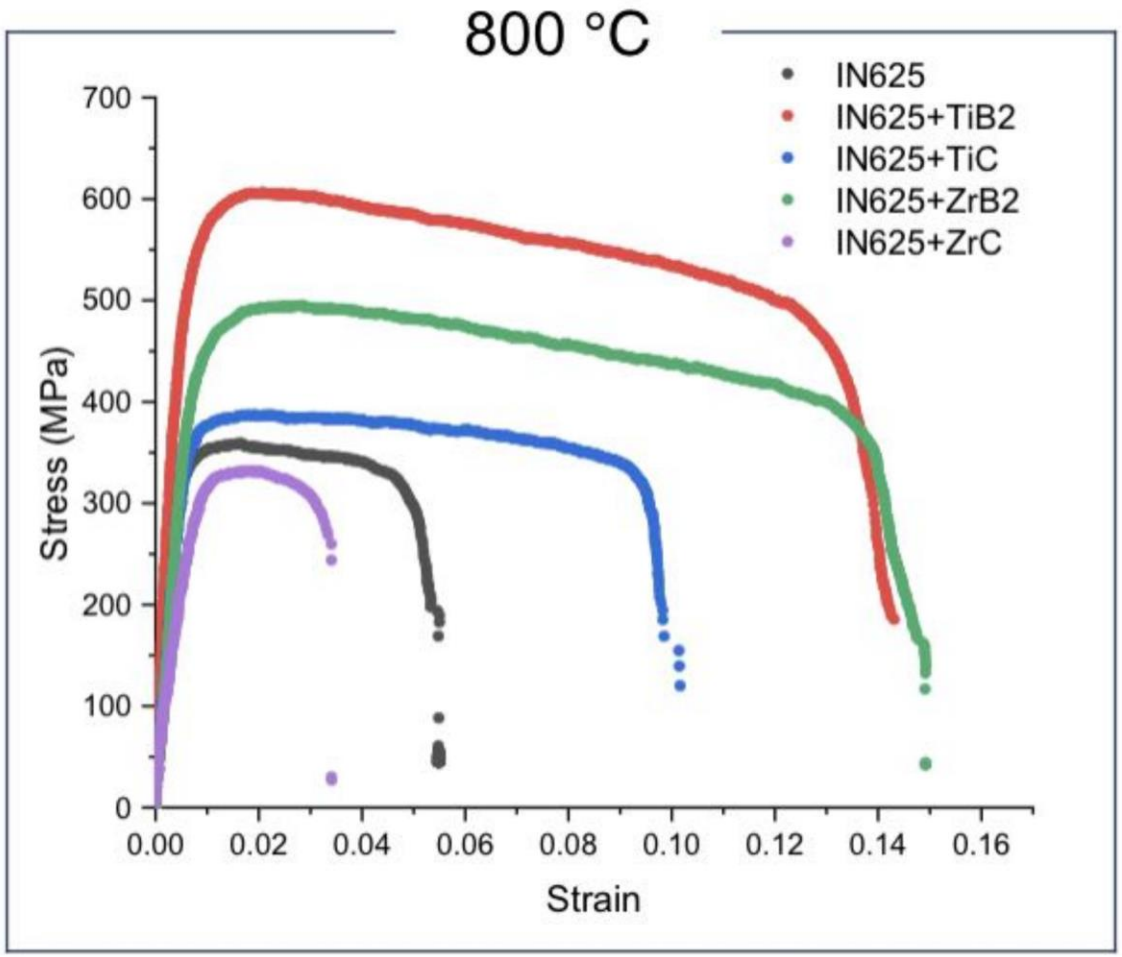

Stress-strain curves of pure In625 and MMCs at 800 ℃

Table. Stress-strain values of pure In625 and MMCs at 800 ℃

Sample	σ_{YS} (MPa)	σ_{UTS} (MPa)	Elongation (%)
In625	332	358	5.4
In625+TiB_2	520	605	14.3
In625+TiC	362	387	10.1
In625+ZrB_2	435	495	14.9
In625+ZrC	313	331	3.4

Creep properties of In625-based MMCs

(Collaboration with Prof. Sangtae Kim at Hanyang University)

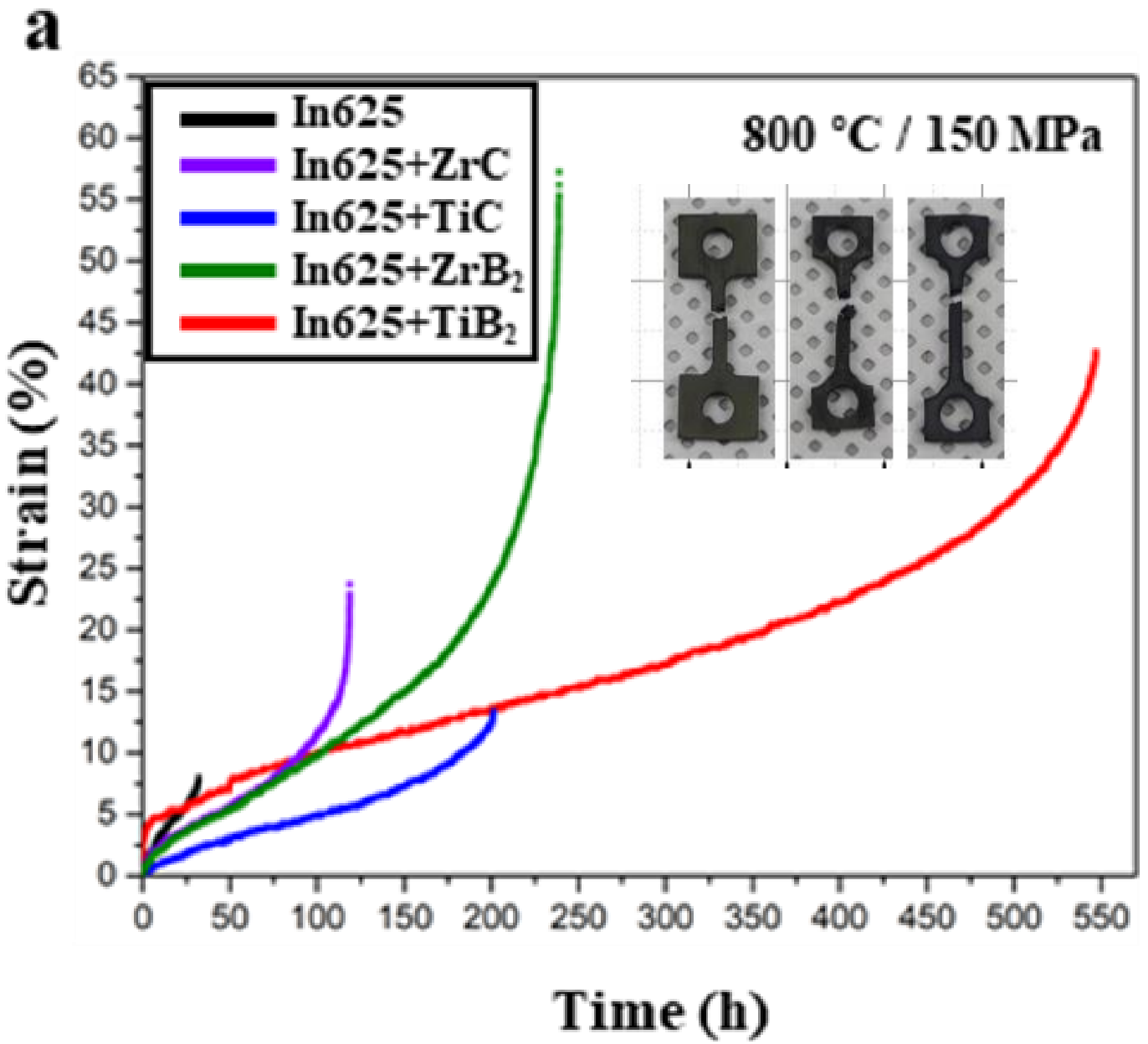

Creep test results for specimens of In625, In625+ZrC, In625+TiC, In625+ZrB_2, In625+TiB_2 under conditions of 800 °C and 150 MPa

In-situ TEM analysis of In625+TiB_2 up to 1000 ºC

(Collaboration with Prof. Fan Sun at ParisTech)

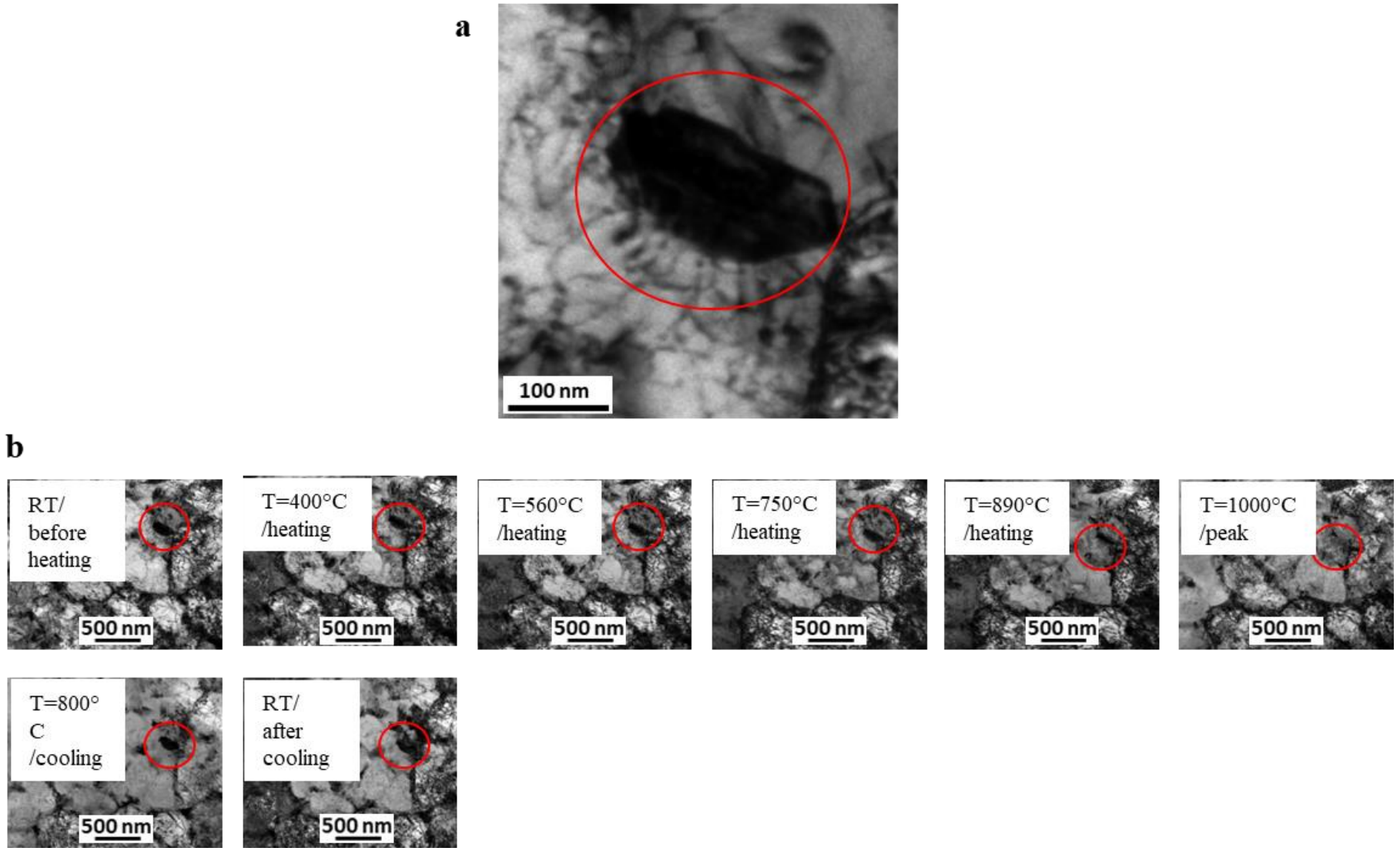

(a) TEM image highlighting the CrB_2 particle, **(b)** temperature-dependent evolution of a CrB_2 particle, indicated by a red circle, with a 100 nm width and 200 nm length.

LPBF Metal-Matrix Composites

1. Carbide and boride additives significantly suppressed grain size, printing defects (cracks & porosity)

2. Impressive room-T and high-T strength / ductility / creep of as-printed samples

Thank you!

Questions?

Fabrication of In718+ZrB_2

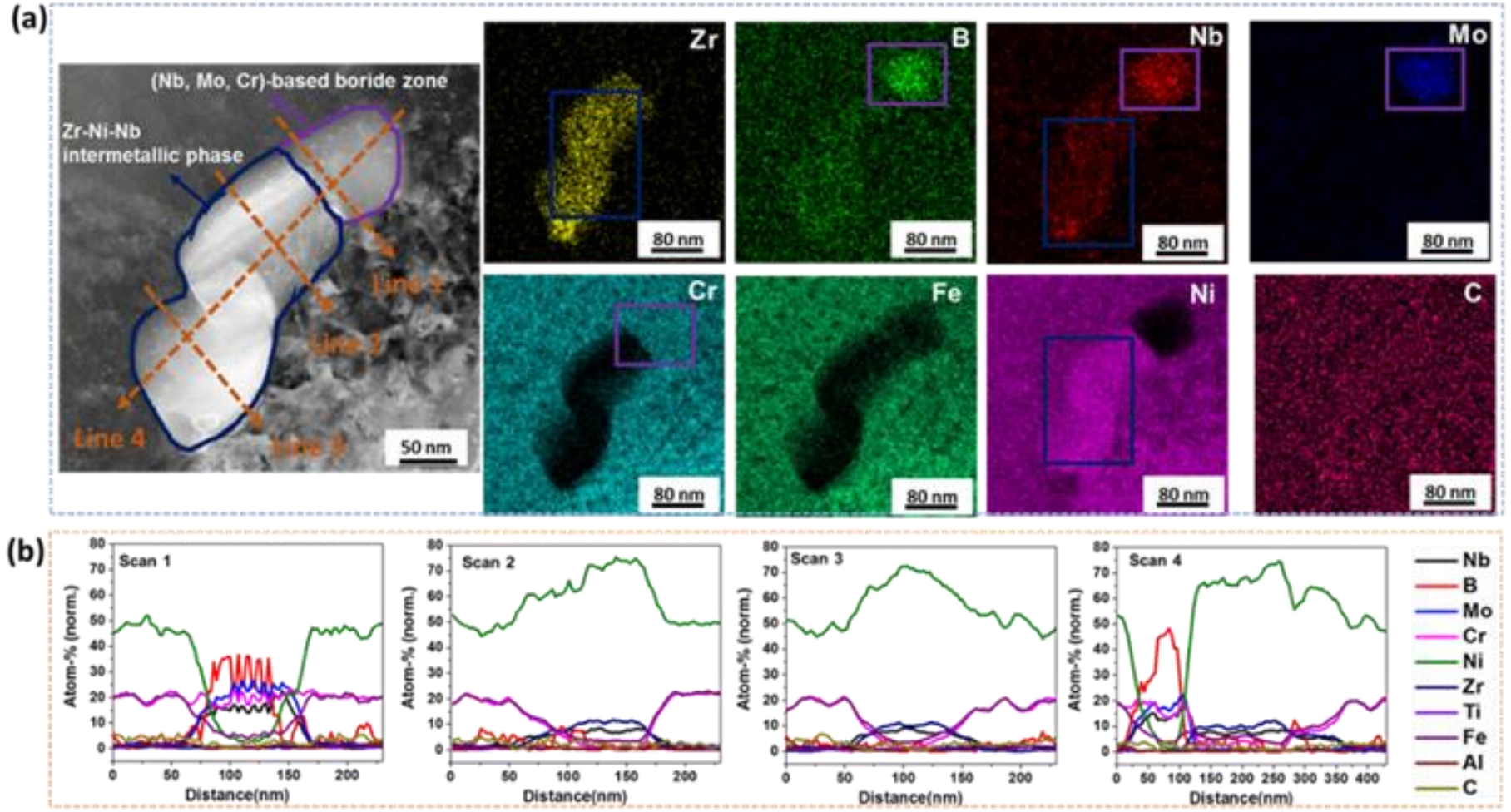

(a) STEM/EDX mapping analysis obtained from HT'ed In718+ZrB_2 focusing on an exchange reaction zone between Zr, B and **Nb, Mo, Cr**, **(b)** High magnification STEM/EDX line profiles obtained from HT'ed In718+ZrB_2 focusing on exchange reaction zone between Zr, B and Nb, Mo, Cr.

Microstructure of as-printed samples

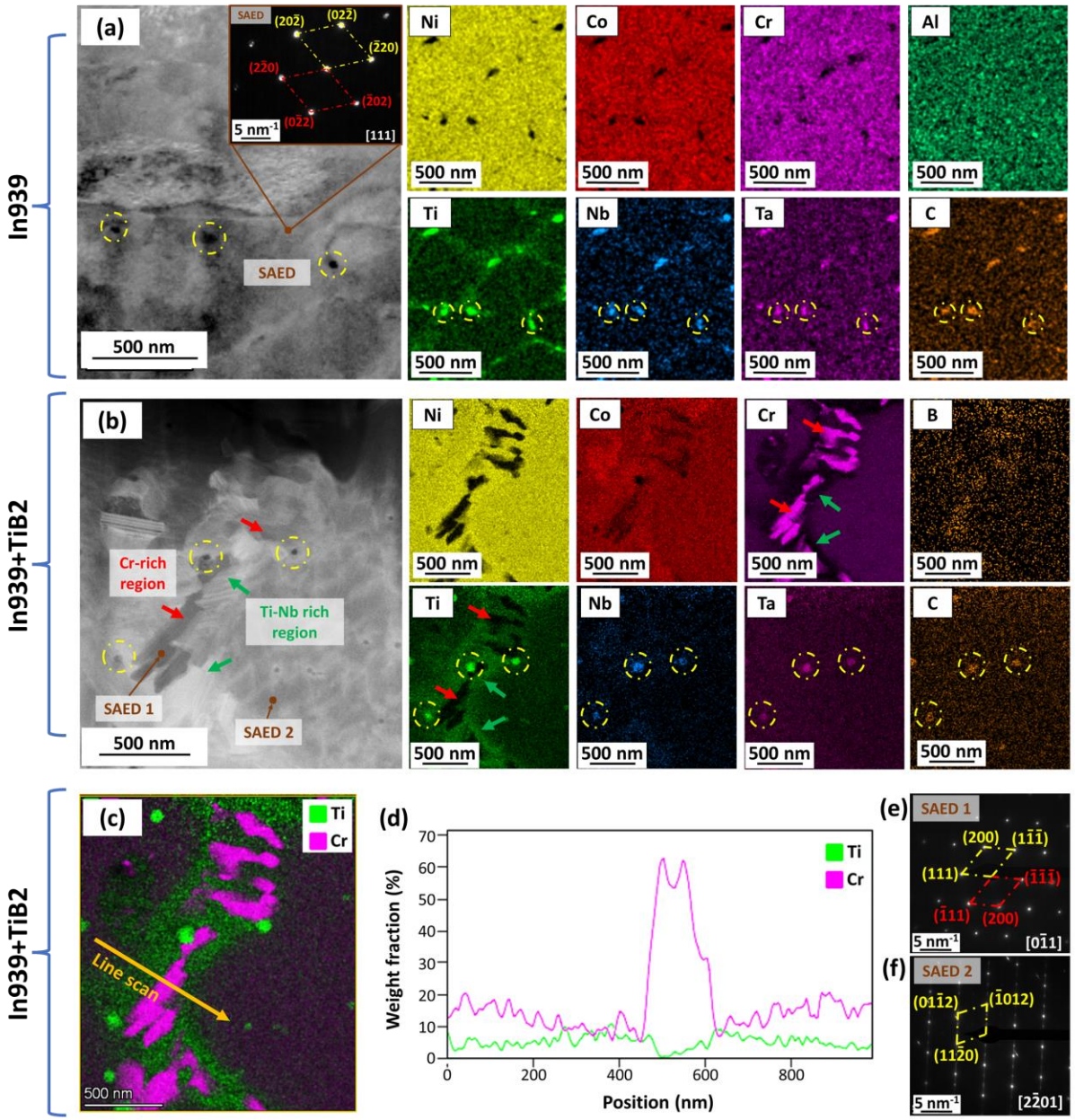

(a) Darkfield STEM/EDX mapping showing the **carbide precipitation** in LPBF-optimized In939,

(b) Darkfield STEM/EDX mapping showing of LPBF-optimized In939+TiB_2. showing the **Cr-based boride and surrounding Ti-rich zone** revealing the exchange reaction between TiB_2 and Cr.

(c-d) STEM/EDX mapping of LPBF-optimized In939+TiB_2 and corresponding line scan analysis showing the **concentration profile of Cr and Ti along exchange reaction zone.**

(e) SAED pattern obtained from gamma matrix revealing the **non-existence of other precipitates** in LPBF-optimized In939+TiB_2 (i.e. gamma prime)

(f) SAED pattern obtained from Cr and B rich region revealing the formation of **CrB_2** in LPBF-optimized In939+TiB_2.

EBSD grain size distribution and texture

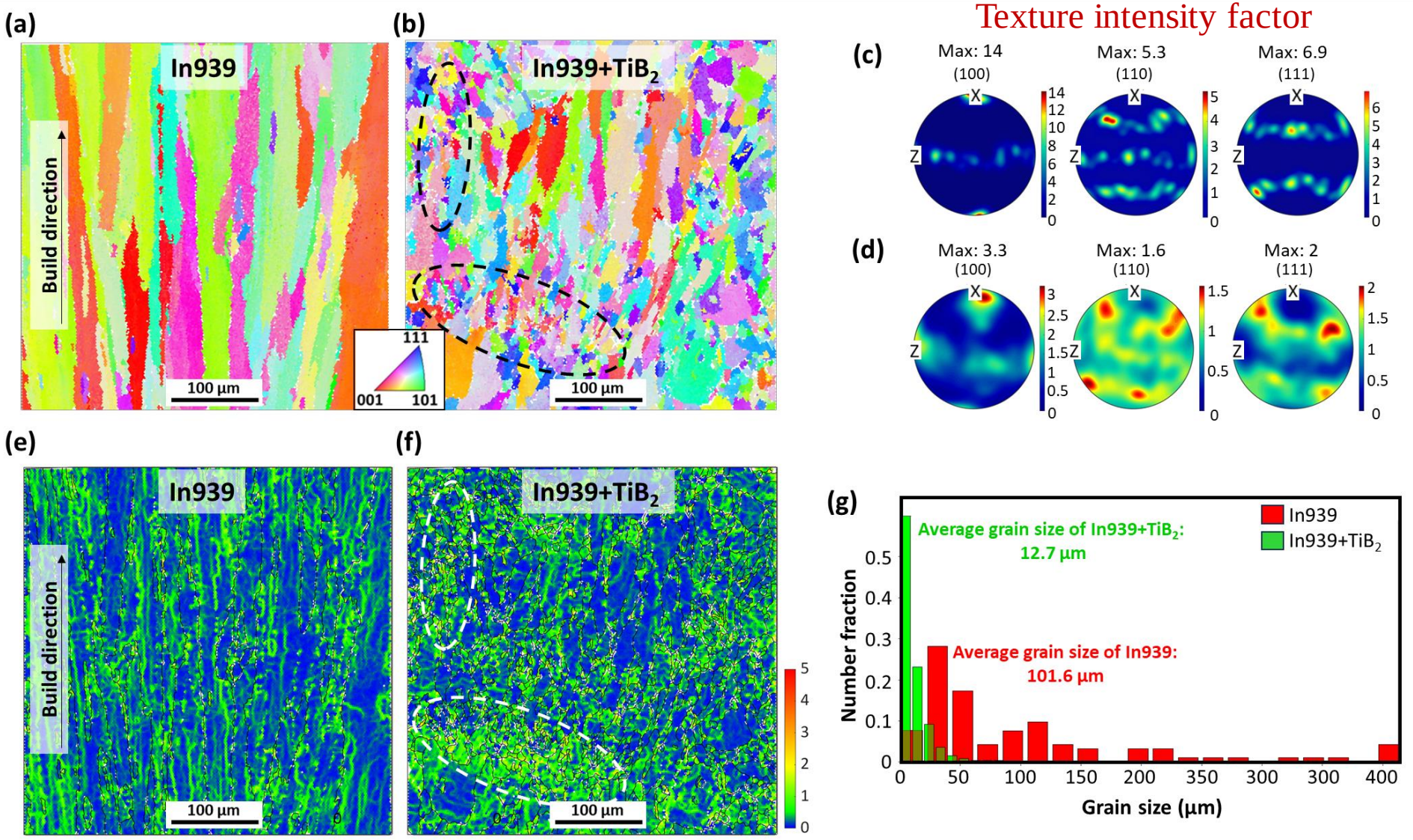

EBSD results obtained from LPBF-optimized In939 and In939+TiB_2: **(a,b)** inverse pole figure maps, **(c,d)** pole figures (PF), **(e,f)** Kernel average misorientation maps (KAM), and **(g)** grain size distribution plot. Please note that the equiaxed fine grains are highlighted within white dashed regions.

Pure In939: Carbides and oxides exist in the vicinity of long cracks. Furthermore, cracking propagates along GBs

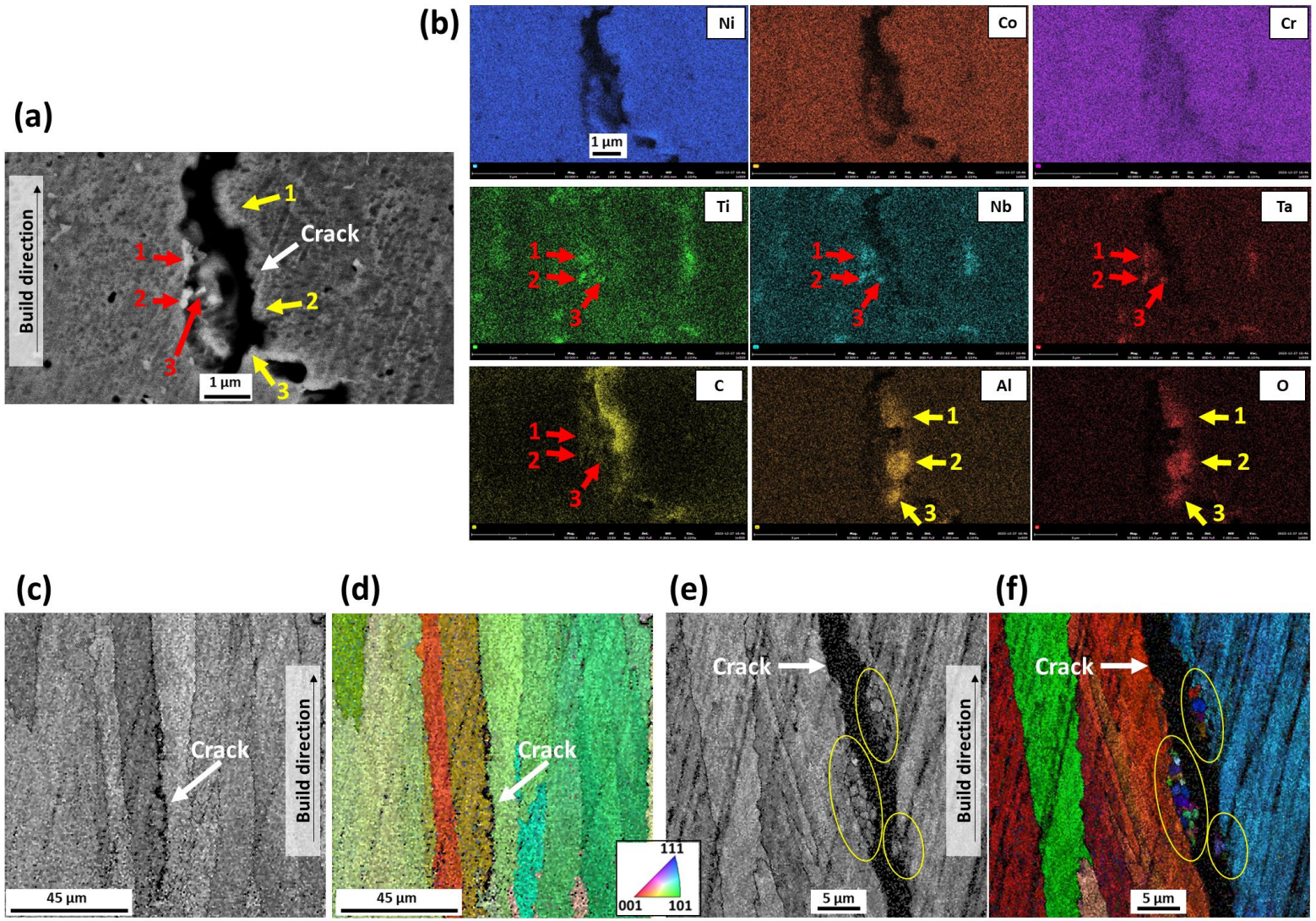

(a,b) SEM/EDX analysis focusing on cracking region, please note that Ti-, Nb-, Ta-based carbides and Al-based oxides indicated by red and yellow arrows. **(c-f)** inverse pole figure maps obtained from cracking zones.

Microstructural properties of as-printed specimens

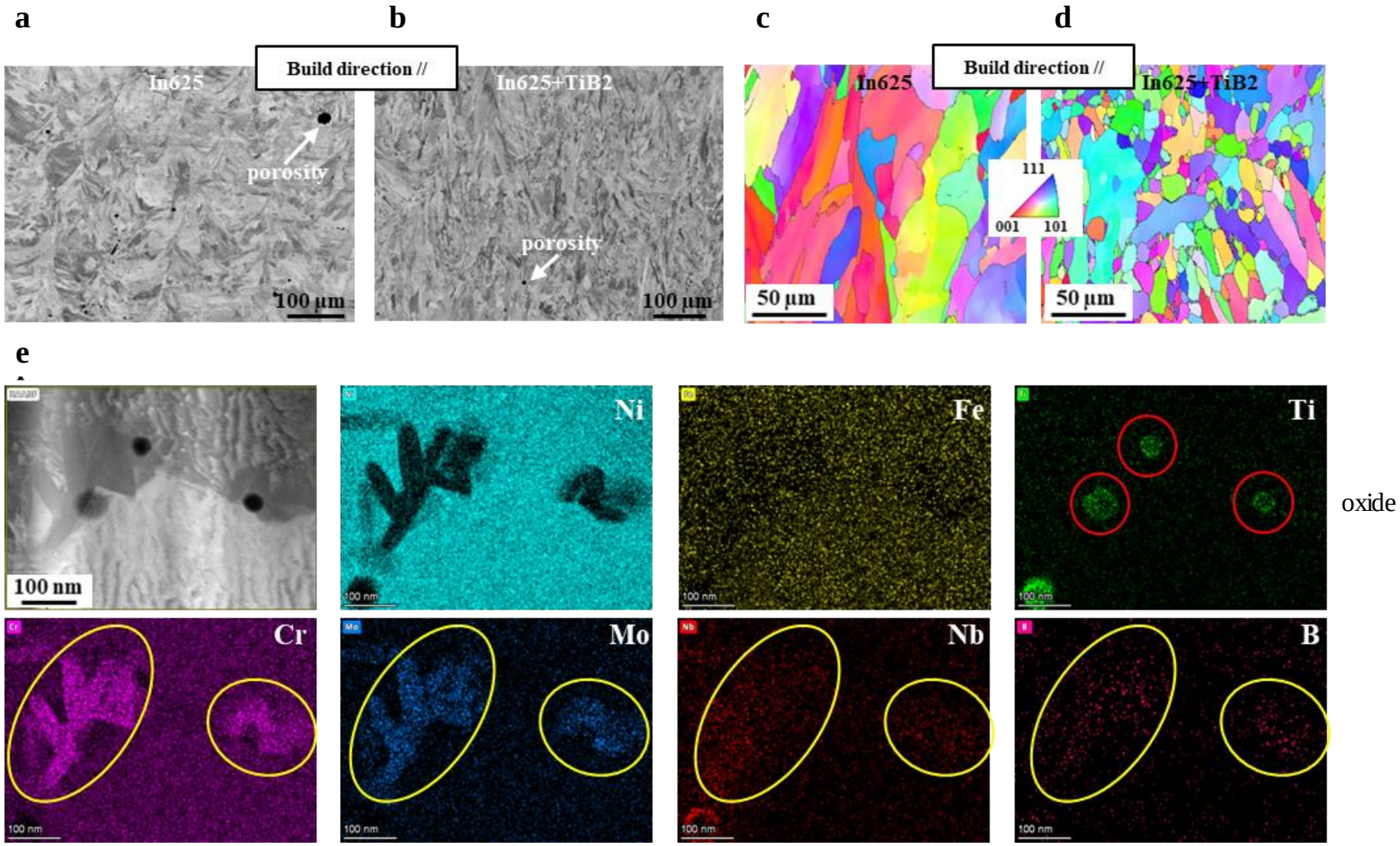

(a-d) SEM images obtained from In625 and In625+TiB_2, (g-h) EBSD orientation maps obtained from In625 and In625+TiB_2 revealing the reduction in grain size, **(e)** STEM/EDX mapping micrographs obtained from In625+TiB_2 shows the exchange reaction zone between **Cr, Mo, Nb**, Ti, and B.

Deformed In625+TiB_2 at 800 °C

(Collaboration with Prof. Gi-Dong Sim at KAIST)

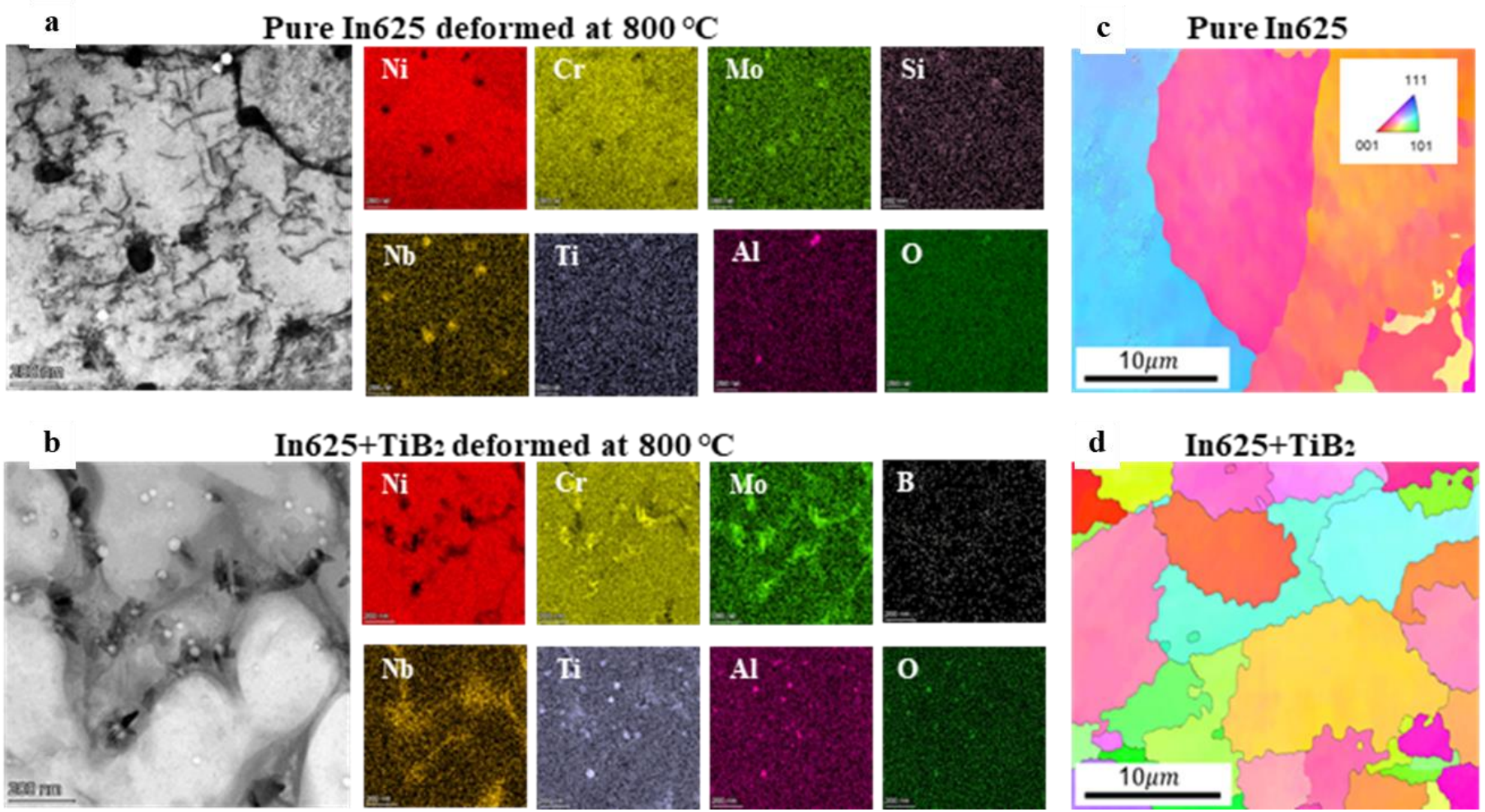

(a) BF-TEM image and STEM-EDS map of deformed In625 and **(b)** In625+TiB_2; **(c)** Characteristics of grain boundaries in pure In625 and **(d)** In625+TiB_2 as confirmed through IPF maps.

Aluminum-Carbon Nanotube Composites

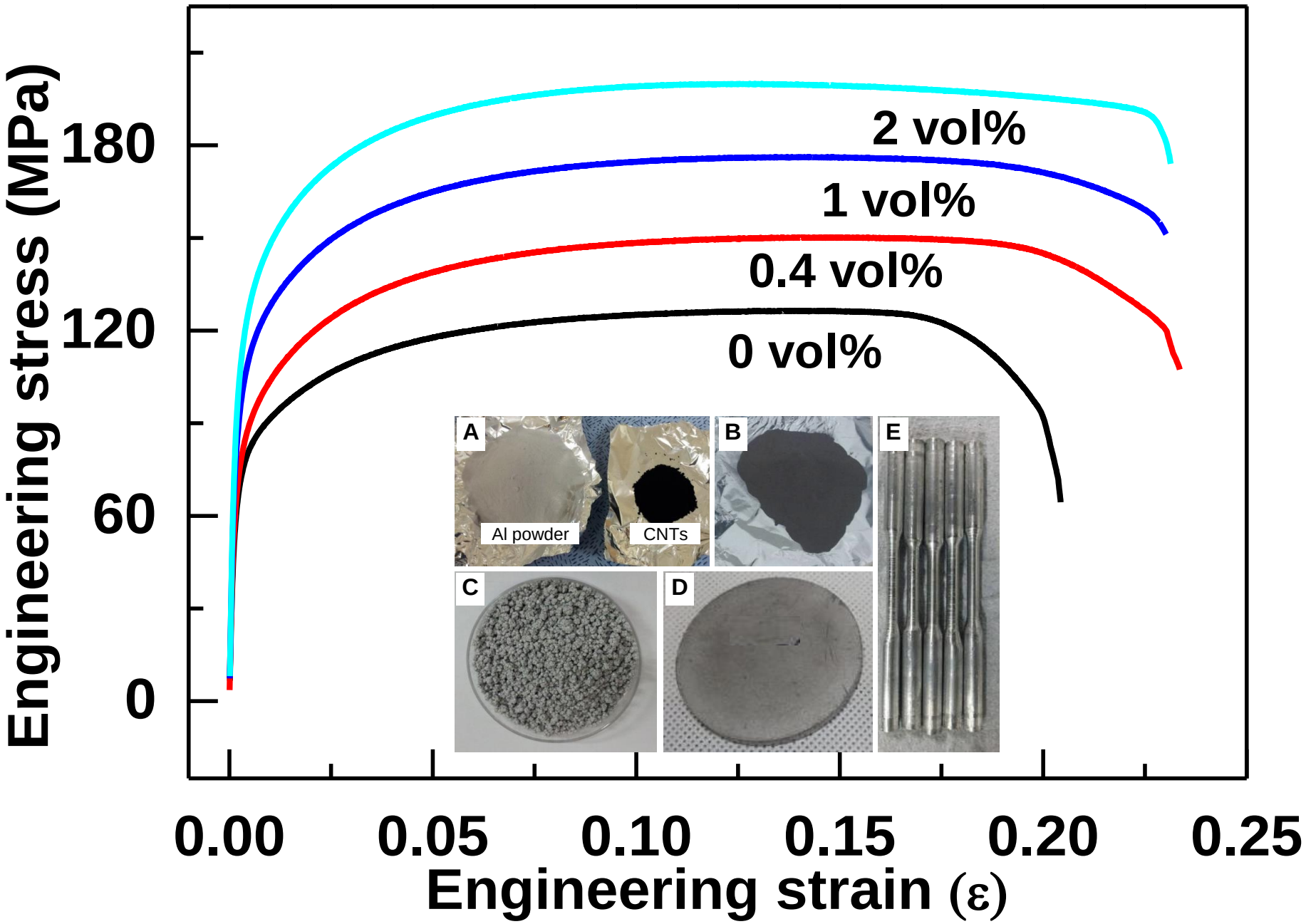

100keV He ion, fluence $10^{17}/cm^2$, peak dose 3.5 DPA

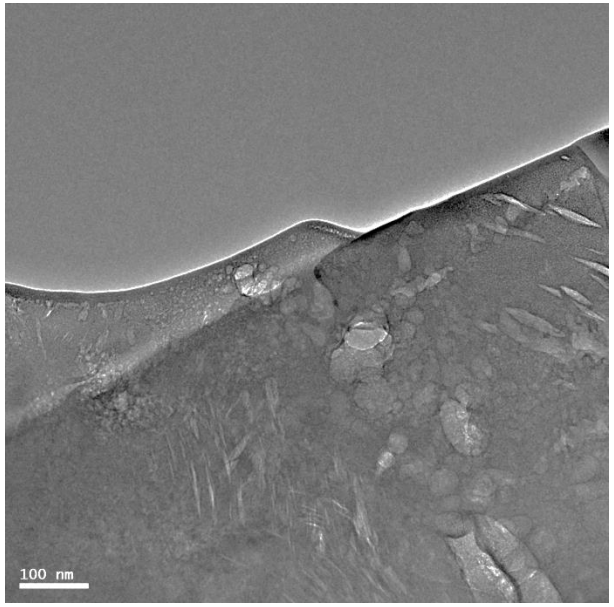

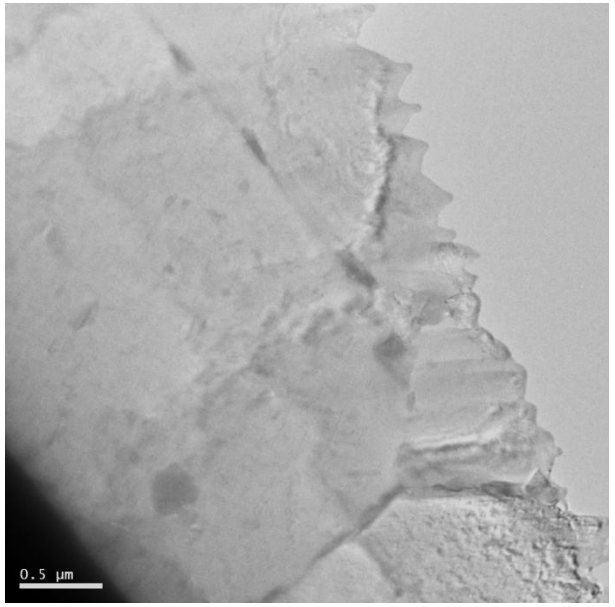

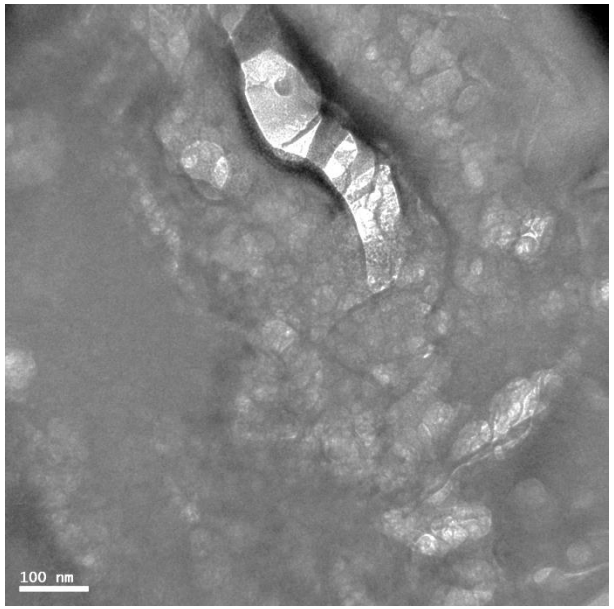

Nano Energy
22 (2016) 319

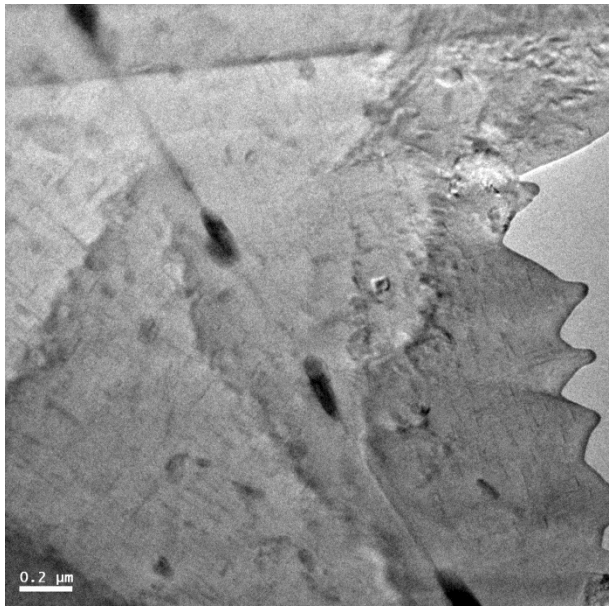

pure Al: pore size 5~50 nm

0.5wt%CNT/Al: no pore observed

2D Dispersoid

Cu (+ 1 vol% Graphene)

Cu

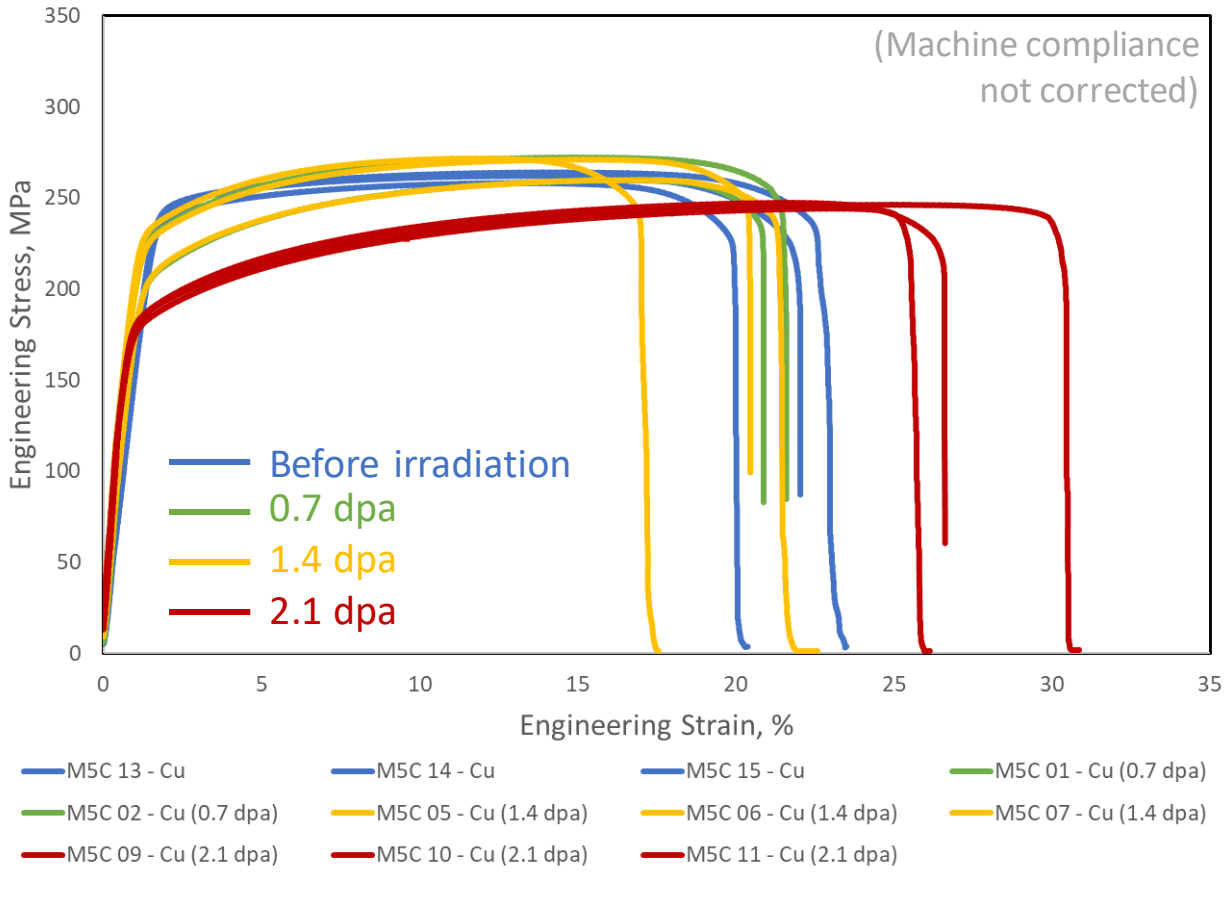

Cu + 1 vol% graphene

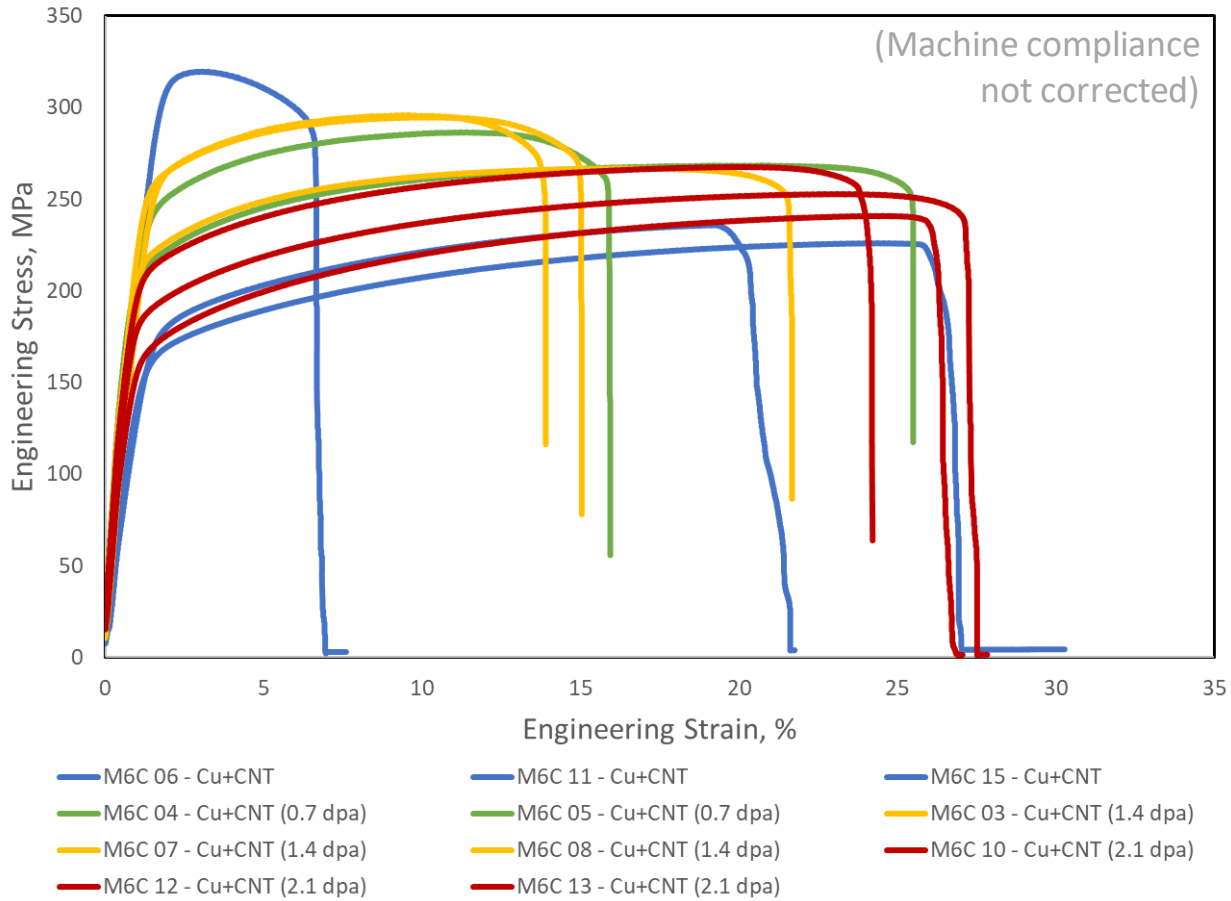

Adding “2D” graphene was not beneficial to strength or ductility or radiation tolerance (mislabeling of dpa may have occurred?)

1000 appm = 0.1 at% doesn't sound like a lot – but Helium goes to GBs

Helium-storing 2nd phases?

Use low-E_{embed} phase to shield/protect higher-E_{embed} phase GBs

H-W. Xu†, S.Y. Kim†, D. Chen, J-P. Monchoux, T. Voisin, C. Sun* and **J. Li***, "Materials Genomics Search for Possible Helium-Absorbing Nano-Phases in Fusion Structural Materials," *Advanced Science* **9** (2022) 2203555.

Helium Embedding Energy dictates Damage Location?

Half-Heusler alloy

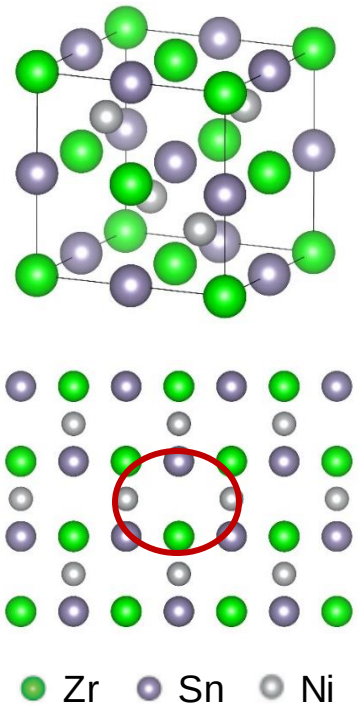

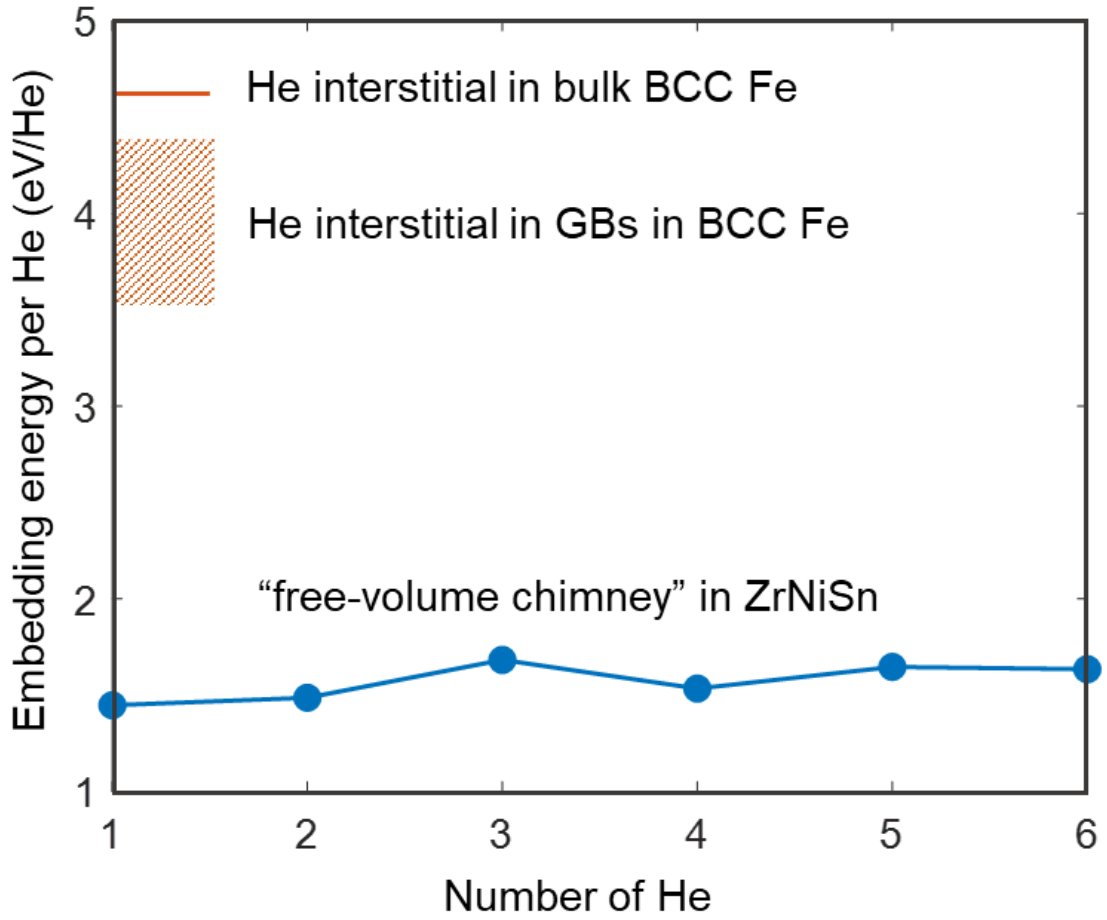

Inspired by the discussion with Prof. Greg Olson

Helium Absorption and Damage Avoidance

Ti-48Al-2W-0.08B (at%) with a γ-α_2 nano-lamellar structure

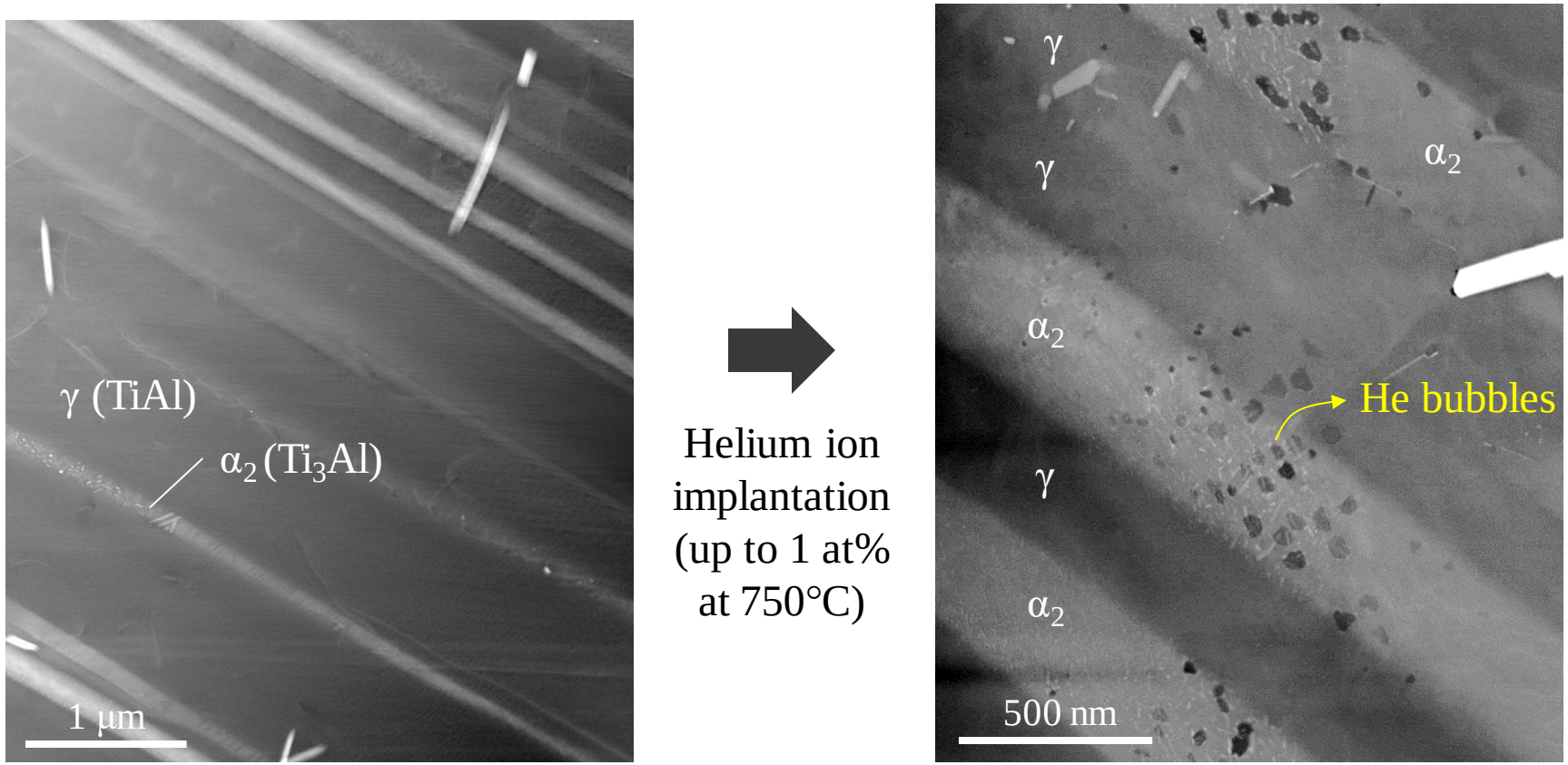

Helium bubbles formed mostly in α_2 phase without noticeable interfacial segregation, leaving γ phase almost intact.

$\mathcal{E}_{emb}$: Energy Required to Embed a Helium Atom

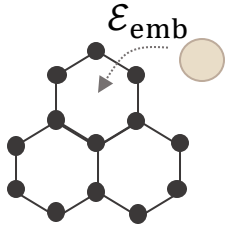

γ (TiAl)

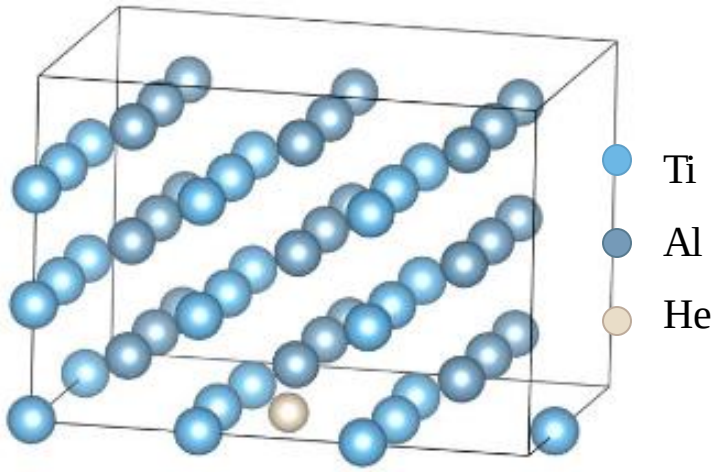

$\mathcal{E}_{emb}$= 3.4 eV/He

α_2 (Ti_3Al)

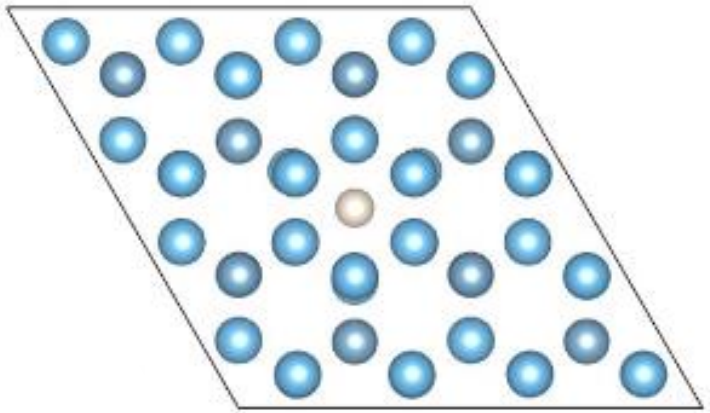

$\mathcal{E}_{emb}$= 2.9 eV/He

"Easier to embed helium"

$\Delta\mathcal{E}_{emb} \geq 0.5$ eV/He enough to enable preferential helium absorption strategy, similar to Fe-GB versus Fe-lattice.

ε_{emb} Correlates with the "Atomic Free Volume"

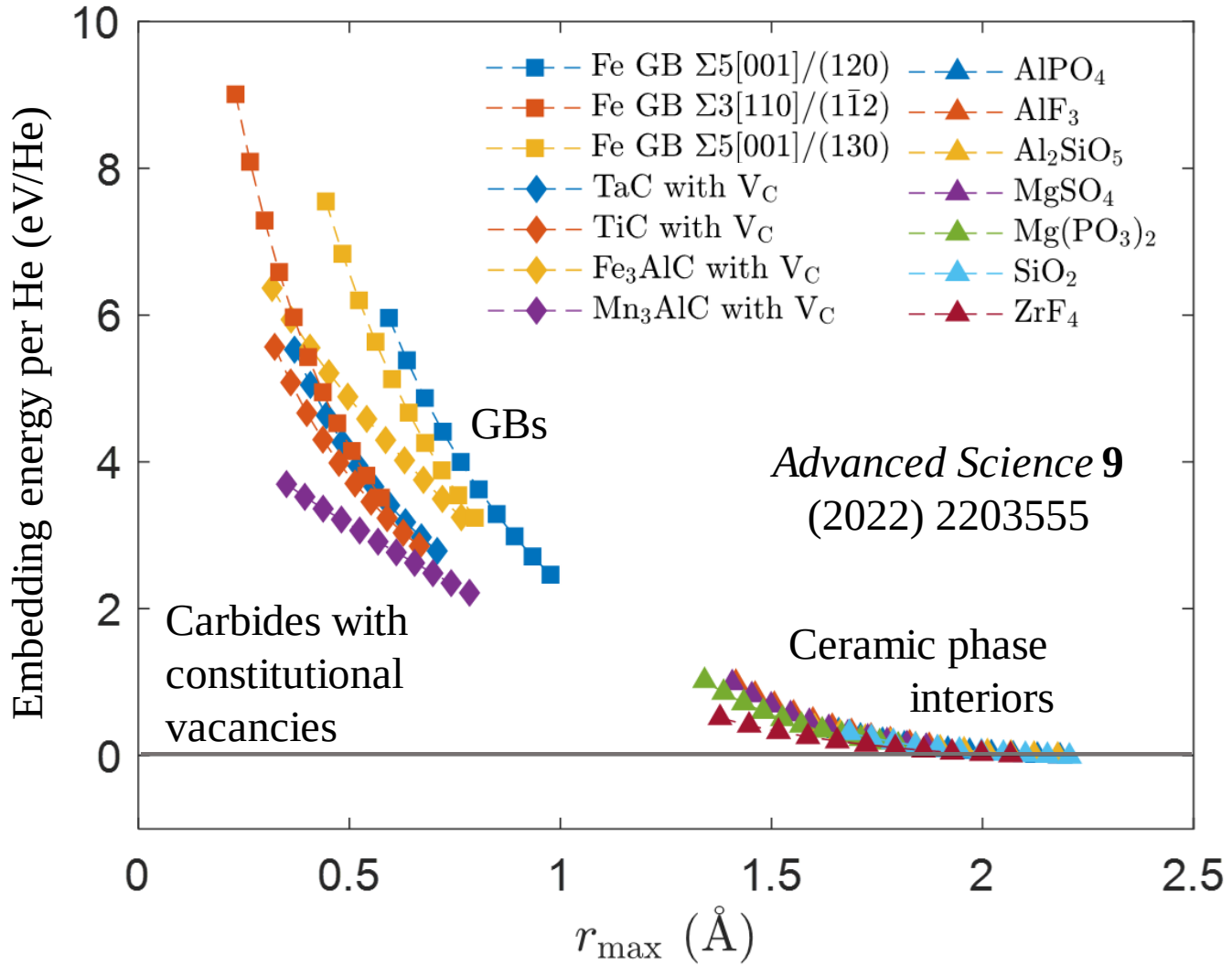

Atomic-scale free volume is indeed a reliable indicator of low helium embedding energy.

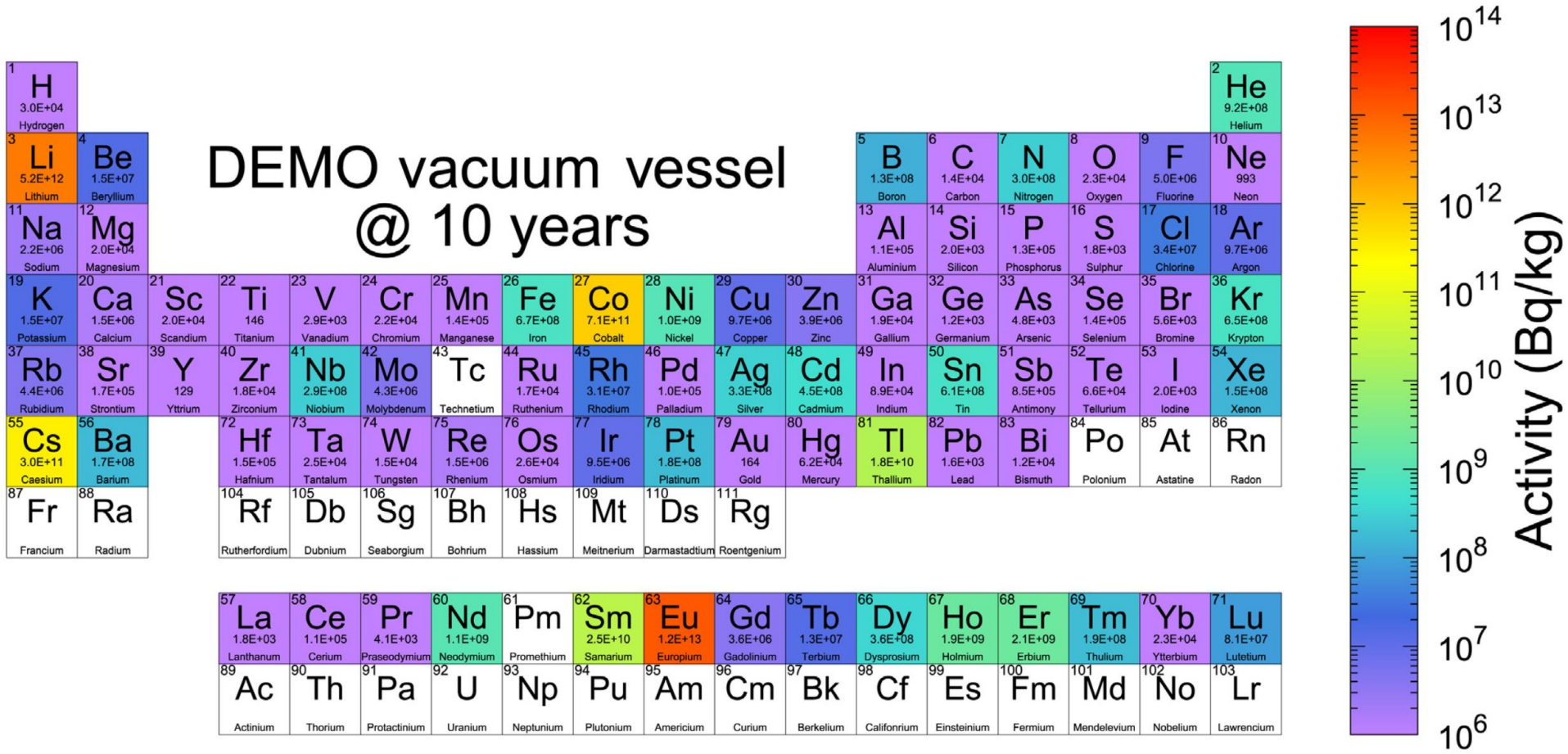

Fig. 10. Periodic table showing the total becquerel activity from each element after 10 years of decay cooling following a 2-fpy irradiation in a DEMO vacuum vessel (VV) environment. The colour of each element reflects the activity according to the Bq/kg legend, but the absolute values are also given beneath each element symbol.

Mark R. Gilbert, Michael Fleming, Jean-Christophe Sublet, "Automated inventory and material science scoping calculations under fission and fusion conditions", *Nuclear Engineering and Technology* **49** (2017) 1346

Screening of Helide Forming Phases

Helium absorbing capability

- Atomic-scale free volume, r_{max} (the radius of the largest sphere that can be fitted in crystal structures) ≥ 1.5 Å

Neutron friendliness

- Neutron absorption cross-section < 1 barn
- Neutron activity < 10^2 MBq/kg 10 years after shutdown

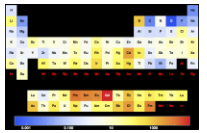

Mechanical robustness

- Bulk modulus > 50 GPa
- Shear modulus > 20 GPa

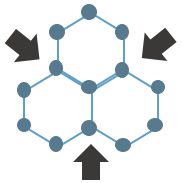

Formula	Materials Project ID	r_{max} (Å)	Average Bulk Modulus (GPa)	Average Shear Modulus (GPa)
$Ca_{72}P_{48}O_{192}$	1197377	1.74	91.71	57.69
$P_{24}Pb_{12}O_{84}$	1203776	1.62	87.50	39.50
$Mg_{10}C_8O_{36}$	1204170	2.21	79.84	40.81
$O_{144}Al_{48}Ca_{72}$	12147	1.63	96.55	64.65
$Ca_2H_8S_2O_{12}$	23690	1.62	80.74	40.69
$Bi_2P_8H_2O_{24}$	24348	1.81	92.20	43.35
$Zr_4P_4O_{18}$	27132	1.61	132.31	71.18
$Bi_4P_{12}O_{36}$	27135	1.70	98.13	47.84
$P_8H_{32}O_{36}$	27141	1.64	83.92	43.67
$Sn_{12}P_8O_{32}$	27493	1.92	72.86	31.93
$Na_8Si_4H_{64}O_{44}$	504605	1.71	74.20	44.55
$Al_6P_{18}O_{54}$	540549	1.63	117.80	65.63

~750 candidate phases were identified (mostly oxides or fluorides).

"Materials Genomics Search for Possible Helium-Absorbing Nano-Phases in Fusion Structural Materials," *Advanced Science* **9** (2022) 2203555

Ceramic – Molten Metal Contact Angle < 90°

```
The first step is to specify the type of estimation and machine learning model you would like to use.
Enter type (1: one metal-one ceramic pair; 2: one metal-list of ceramics; 3: ICSD screening): 2
Enter model (all: model trained using all features; reduced: model trained using a reduced number of features): all
==================================================================
The second step is to specify the systems of interest.
Note that this code is case sensitive. You need to enter "Fe" for iron; "fe" does not work.
Also, you need to enter "Si1O2" for silicon dioxide; "SiO2" does not work.
Enter the metal of interest (e.g., Fe): Li
Upload the csv file with the list of ceramics to the session storage and enter the filename (e.g., filename.csv): lists.csv
Enter the header of the list of ceramics (e.g., ceramic): comp
==================================================================
The third step is to specify the temperature range of interest.
Enter the temperature of interest in Kelvin in the format, "min-max-interval (e.g., 1800-1800-0 or 1800-2300-100)": 500-500-0
```

- The wettability of CaO by molten Li
  - Machine learning model: 119.5°
  - *Ab initio* molecular dynamics si

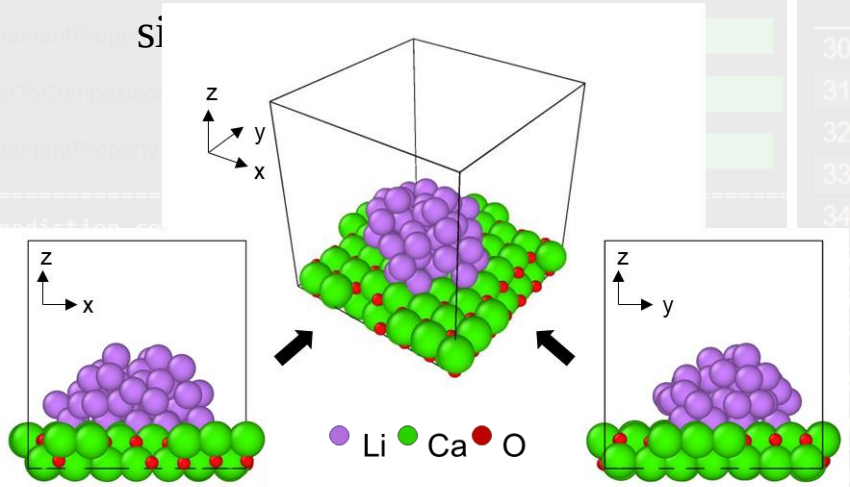

test.csv

31 to 40 of 48 entries | Filter

	Metal	Substrate	Temp	theta_pred
30	Li	CaO	500.0	119.5
31	Li	Pr2O3	500.0	120.9
32	Li	La2O3	500.0	121.3
33	Li	NaI	500.0	111.2
34	Li	Ac2O3	500.0	120.9
	Li	YbO	500.0	119.2
	Li	BaI2	500.0	117.5
	Li	CaH2	500.0	110.2
	Li	Er2O2S	500.0	119.9
	Li	Ho2O2S	500.0	120.0

10 per page 1 2 3 4 5

S.Y. Kim and **J. Li**, "Machine learning of metal-ceramic wettability," *Journal of Materiomics* **8** (2022) 195

Down-Selection of Helide-Forming Phases

- Melting point > 1600 °C for casting
- Phase compatibility: no decomposition when in contact with the matrix
- Interfacial wetting and adhesion: ideally, contact angle less than 90°

Matrix: Fe

Chemical formula	Material project ID	Avg. bulk modulus (GPa)	Avg. shear modulus (GPa)	r_{max} (Å)	Contact angle at 1600 °C (deg.)	Melting point (°C)	Phases at 800 °C for Fe with 1 wt.% of He-absorbing nano-phase
Al_2SiO_5	mp-4753	155.8	97.5	1.90			X
$AlPO_4$	mp-7848	84.6	48.2	1.92			X
SiO_2	mp-546794	93.8	57.5	1.93			
AlF_3	mp-468	116.1	53.0	1.64		X	
$Mg(PO_3)_2$	mp-18620	113.5	60.8	1.57			X
$MgSO_4$	mp-4967	106.8	51.5	1.64			X
ZrF_4	mp-561384	133.4	54.7	1.73		X	

- Decomposition products could also be useful if they have large free volume.
- Less strict atomic-scale free volume criterion (e.g., r_{max} > 1 Å) could also be enough.

Advanced Science **9** (2022) 2203555 | CALPHAD: ThermoCalc (TCFE8)

Composite Design

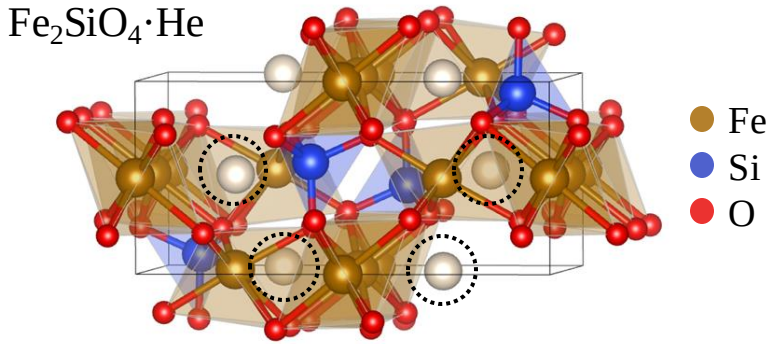

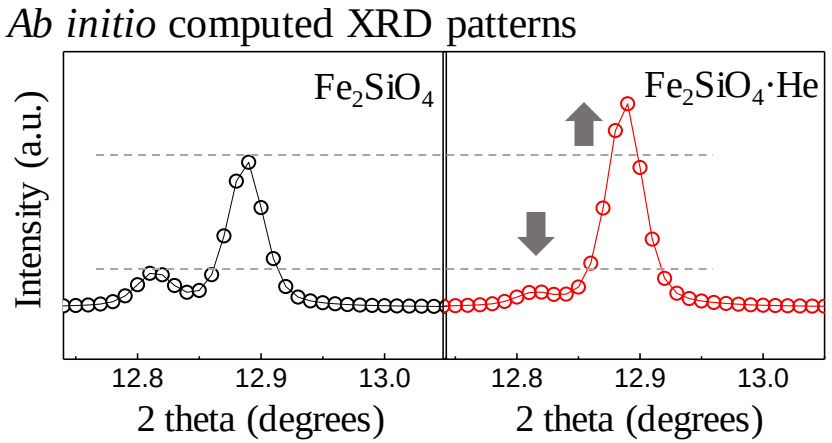

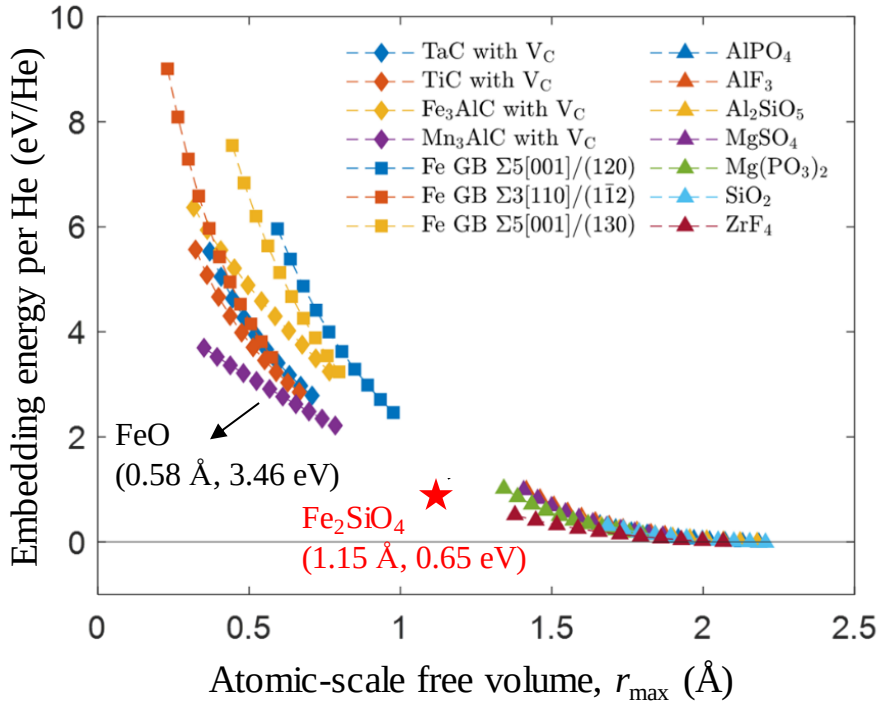

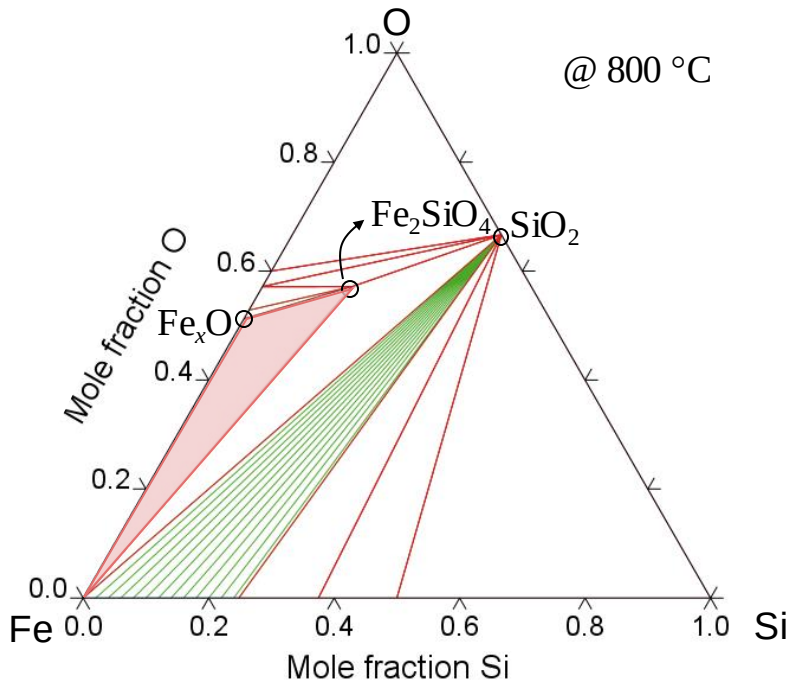

DFT: VASP (GGA-PBE, PAW & plane-wave basis func.) | CALPHAD: ThermoCalc (TCFE8)

S.Y. Kim et al. "Demonstration of Helide Formation for Fusion Structural Materials as Natural Sinks for Helium," *Acta Materialia* **266** (2024).

Experiment Design

Helium ion implantation

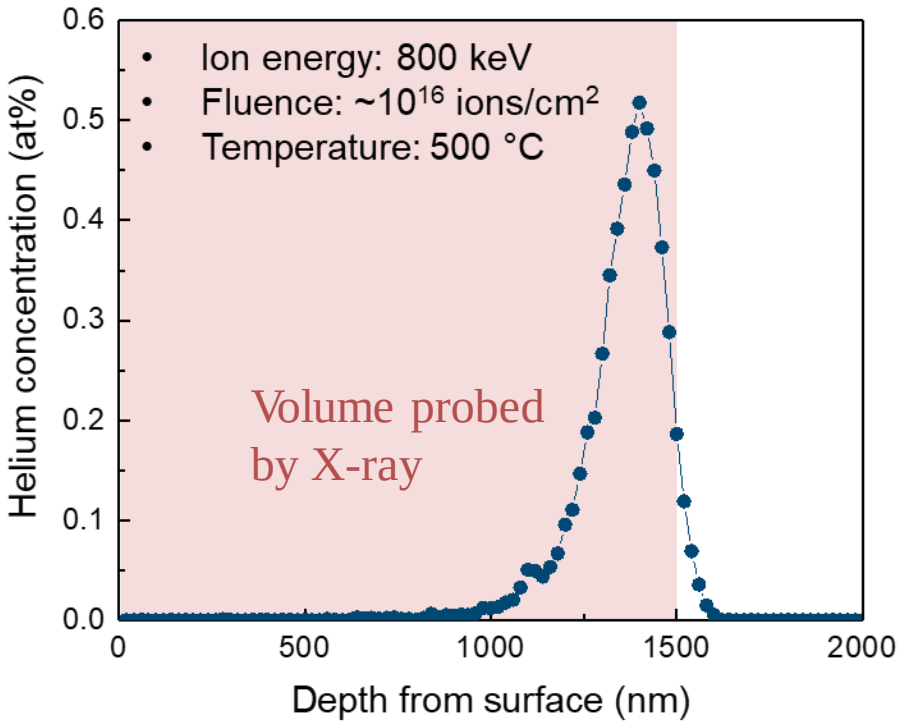

Grazing incidence XRD (GIXRD)

- X-ray incident angle: 1°

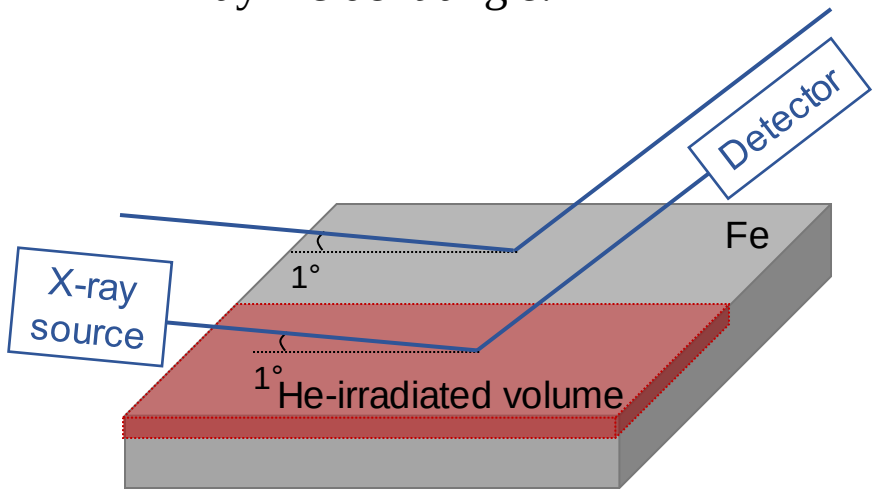

Fe_2SiO_4 to helium ratio = 1:1 (Fe_2SiO_4·He, ~10 at% uptake)

SRIM (Kinchin-Pease) | GIXRD: PLS (5A-XRS)

S.Y. Kim et al. "Demonstration of Helide Formation for Fusion Structural Materials as Natural Sinks for Helium," *Acta Materialia* **266** (2024).

Experimental vs. Computed XRD Patterns

Computed XRD patterns

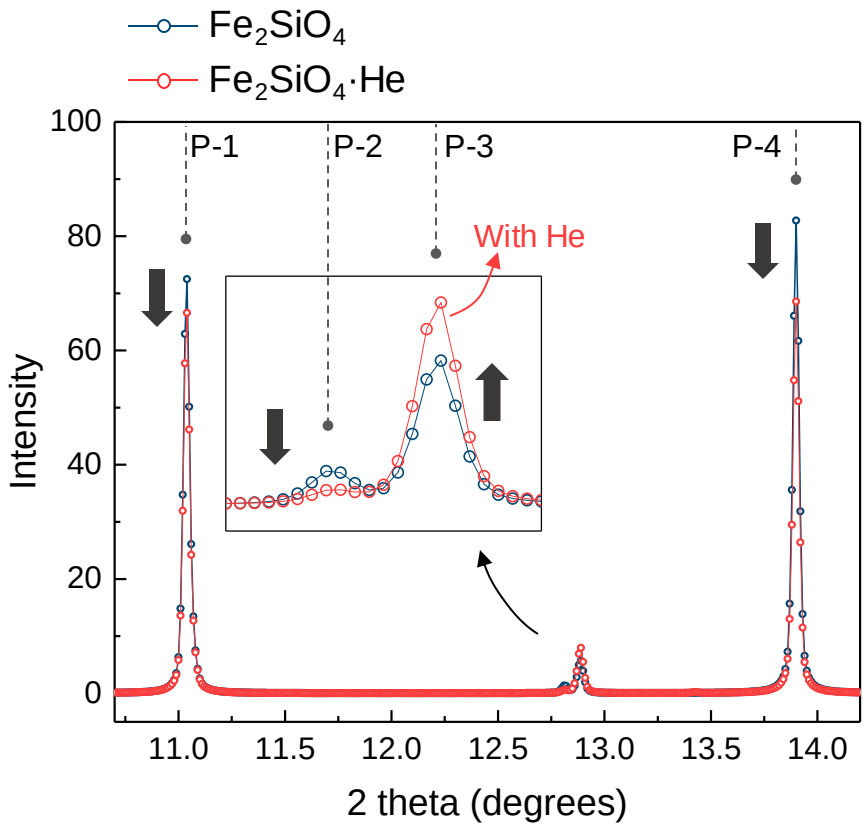

Experimental XRD patterns

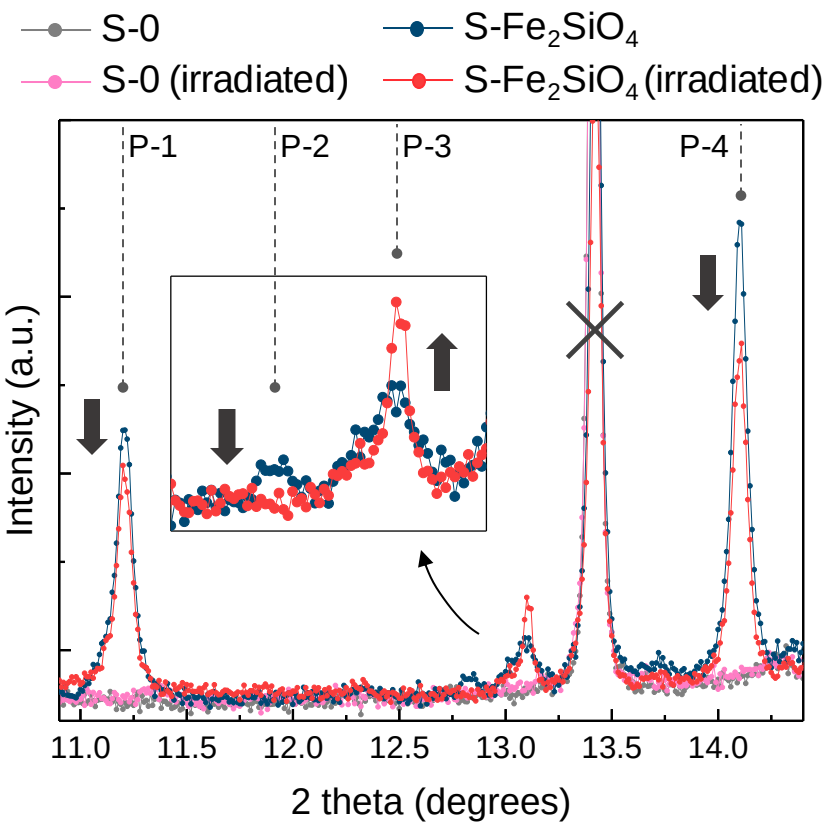

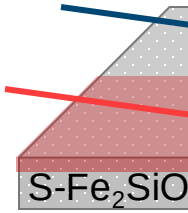

- Peaks related to Fe_2SiO_4: P-1, P-2, P-3, and P-4.
- In both patterns, P-1 and P-4 decrease. P-2 almost disappears, while P-3 sharpens; this agreement **confirms atomic helium storage** within the **bulk lattice of Fe_2SiO_4.**

GIXRD: PLS (5A-XRS) | DFT: VASP (GGA-PBE, PAW & plane-wave basis func., ISIF=2, λ = 0.692649 Å)

S.Y. Kim et al. "Demonstration of Helide Formation for Fusion Structural Materials as Natural Sinks for Helium," *Acta Materialia* **266** (2024).

Helium Bubbles Accumulation

5,000 appm (practical requirements: 1,000-2,000 appm)

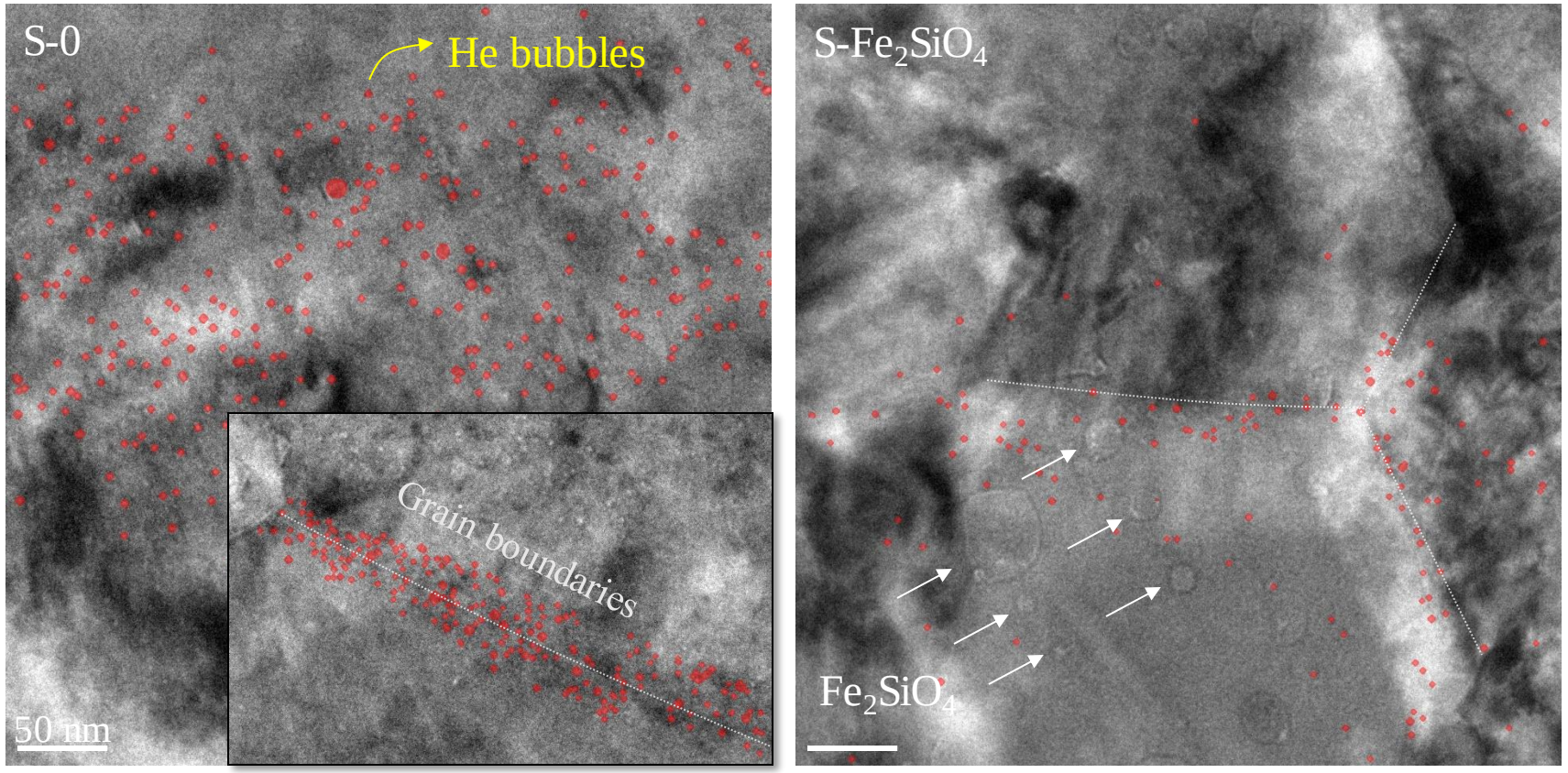

$d = 4.7 \pm 0.8$ nm; $n = 1.67 \times 10^{22}/m^3$

$d = 3.6 \pm 0.7$ nm; $n = 8.01 \times 10^{21}/m^3$

Incorporation of helide formers by ~1 vol% can reduce the diameter (d) and the number density (n) of helium bubbles by > 20% and > 50%, respectively.

S.Y. Kim et al. "Demonstration of Helide Formation for Fusion Structural Materials as Natural Sinks for Helium," *Acta Materialia* **266** (2024).

Estimation of the Required Volume Fraction

J. Knaster et al., *Nature Physics* **12** (2016) 424

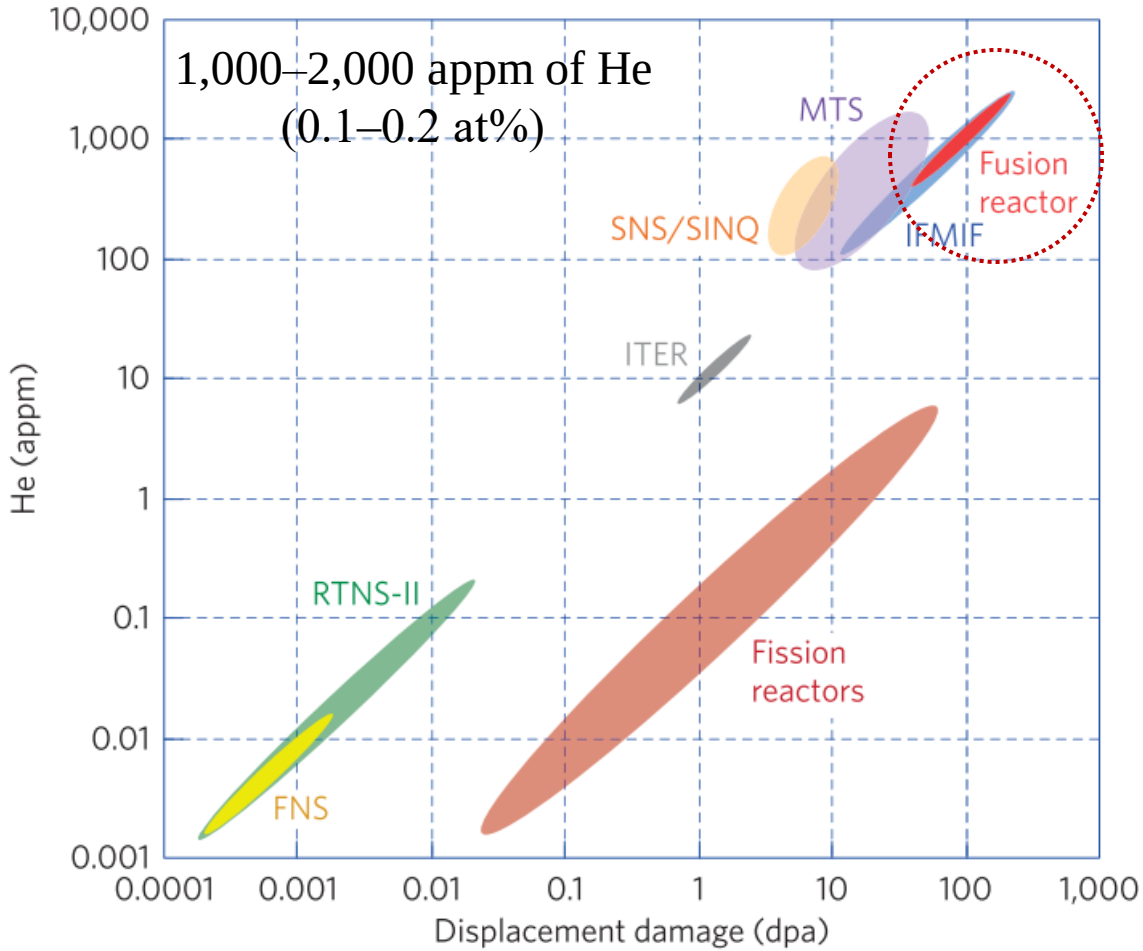

Poster E-26
(Today @5:30 PM,
Hyatt-Regency R)

So Yeon Kim
@ Li Group

One helium atom per molecule (e.g., $Fe_2SiO_4 \cdot He$)
➔ 0.1–0.2 mol% of 2nd phase could be enough (roughly ≤ 2 vol%)

S.Y. Kim et al. "Demonstration of Helide Formation for Fusion Structural Materials as Natural Sinks for Helium," *Acta Materialia* **266** (2024).

Neutron irradiation of boron-doping materials

- Excess helium production by $^{10}B(n, \alpha)^{7}Li$ reaction
  - $^{10}_{5}B + n_{th} \rightarrow {}^{4}_{2}He^{2+} + {}^{7}_{3}Li^{3+}$ ($KE_{He} = 1.470$ MeV, $KELi = 0.840$ MeV)

reaction cross-section **3980 barn**

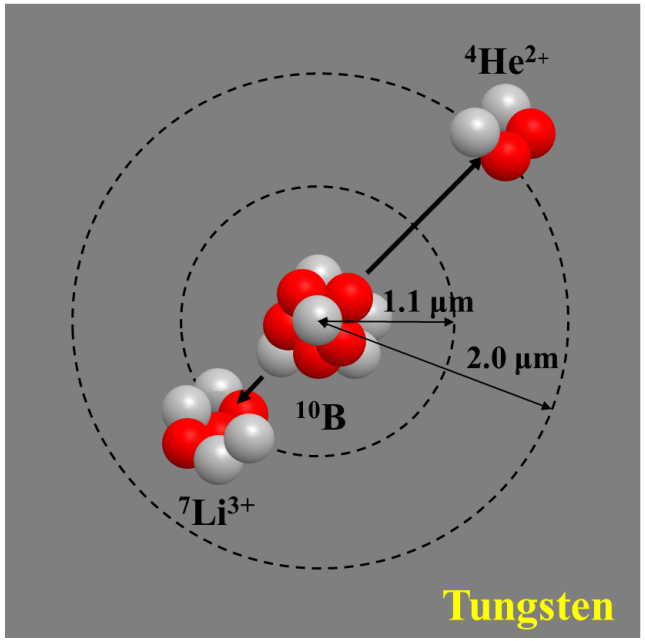

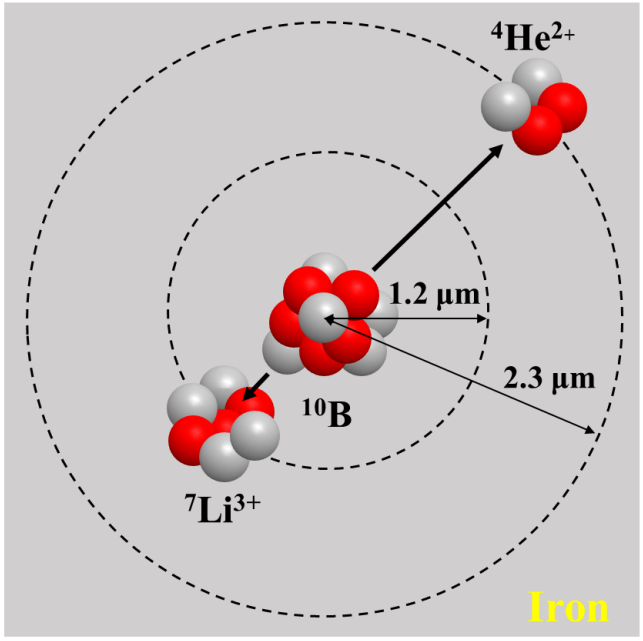

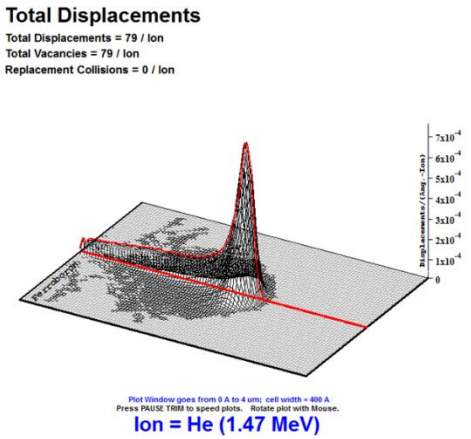

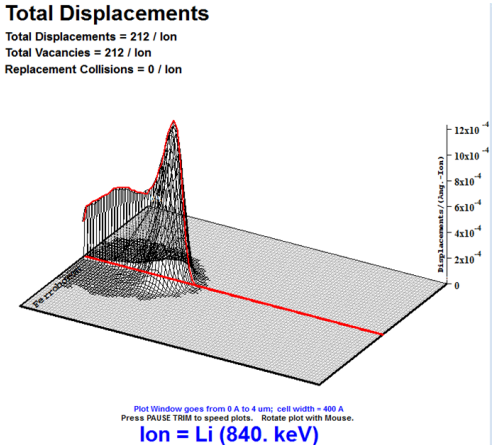

MITR 3GV port: thermal neutron flux as high as 10^{13} $n_{th}/cm^2/s$

Unlike Boron-10 with a gigantic thermal neutron capture cross-section of **3980 barn**, Boron-11 has a thermal neutron capture cross-section of only **0.005 barn**

Yunsong Jung and Ju Li, "Boron-10 stimulated helium production and accelerated radiation displacements for rapid development of fusion structural materials," *Journal of Materiomics* **10** (2024) 377-385

Helium generation and radiation damage of ^{10}B-doped Fe and W irradiated at HFIR for 25 days.

Material	Dopant concentration (appm)		He generation (appm)	Radiation damage (dpa)			He appm/dpa
	^{10}B	^{235}U		Neutron (>0.1 MeV)	^{10}B(n, α)^{7}Li	Fission reaction	
Fe	1,000	0	1,000	1.9	0.300	0	455.0
	1,000	1,000				10.0	82.0
	1,000	9,600				98.0	10.0
W	13	0	13	0.8	0.001	0	16.0
	13	13				0.1	14.0
	13	4,000				25.0	0.5

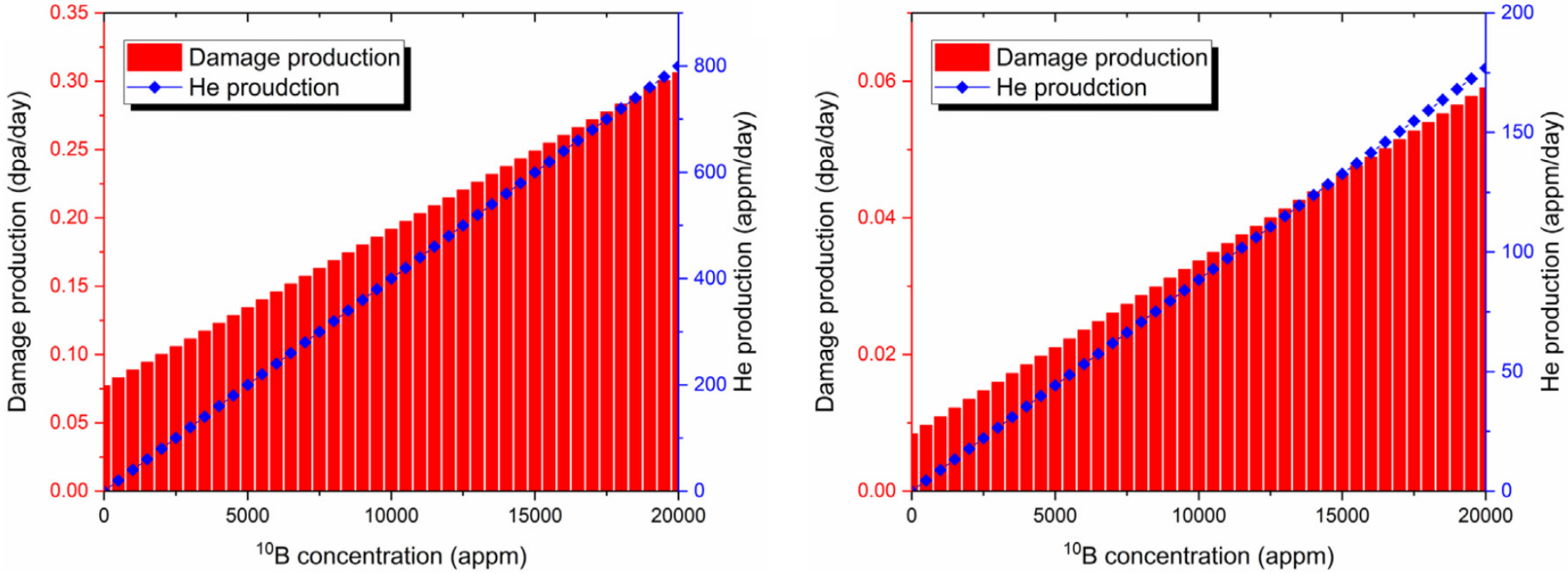

Fig. 7. Radiation damage production and helium production of iron doped with various ^{10}B (a) neutron irradiation at HFIR (the half-life of burnt ^{10}B was ~0.9 days) (b) neutron irradiation at MITR (the half-life of burnt ^{10}B was ~61.4 days).

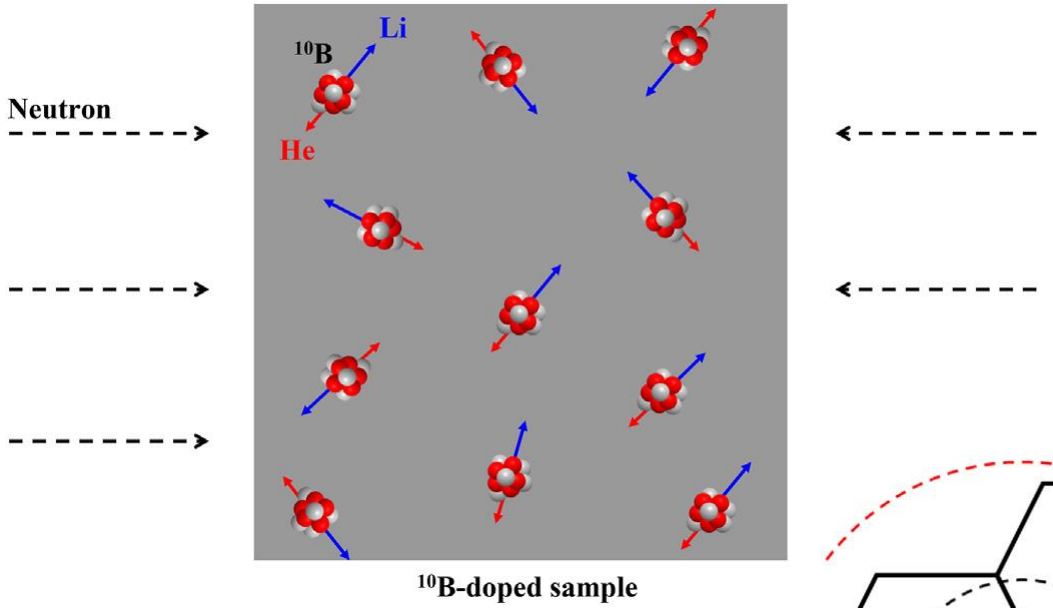

Yunsong Jung and Ju Li,
"**Boron-10 stimulated helium production and accelerated radiation displacements for rapid development of fusion structural materials**,"
J. Materiomics **10** (2024) 377

Even a **boride particle** is likely to fragment into "bomblets", due to the extreme energetic nature of the $^{10}B(n, a)^{7}Li$ product nuclei and the **Coulomb explosion** of the electron cloud left behind. Thus later on, the distribution of the dpa and appm (He) could become much more homogenized due to the "**nano-bomblets**" effect.